Alma Mater Studiorum
Università di Bologna

Dottorato di ricerca in Geofisica - XX Ciclo

Tesi di Dottorato
Settore scientifico-disciplinare FIS/06

High frequency seismic and underwater acoustic wave propagation and imaging techniques

---

Dottorando:
Dr. Tony Alfredo Stabile

Tutor:
Prof. Aldo Zollo

Coordinatore:
Prof. Michele Dragoni

Esame finale anno 2008

To my wife and my son,
my everlasting love.

Contents

List of Figures

List of Tables

Introduction

The direct measurement of elastic properties of the Earth interior encounters many problems due both to the vast dimension of our planet and to the technological difficulty to perform measurements in depth of its physical properties. In fact, for the solid Earth the only means of in situ measurements is by drilling, which however can perforate few kilometres of the crust and provides only a few point measurements. For this reason drillings are insufficient to describe the global structure of the Earth and elastic waves constitute the solution of the problem.

The elastic waves are generated by natural or human made sources. Earthquake generated waves may travel through the Earth depending to the source energy and carry on the surface the information (seismograms) about its physical properties which can be interpreted by seismologists. This approach is based on the use of indirect methods to reconstruct the internal structure and physical properties of the Earth (e.g. tomography, seismic reflection, and seismic refraction) or to study the processes that have generated the observed wavefield.

The most part of the Earth surface is covered by water, so there is the necessity to install seismic instruments also on the seafloor. Geophysical observation at sea present different difficulties with respect to on-land where seismic observation are routinely made. The main problems are the transmission of data on the surface, the installation and the maintenance of underwater stations, the usage of instruments in the seawater and the remote control of the submerged instrumentation, so the observations at sea become very expensive.

The problem related to the transmission of data in seawater can be solved by the use of acoustic wavefield, since both light and radio waves propagates hardly in the water respect to acoustic waves as a consequence of a higher attenuation. Recently there has been a rapid extension of the use of digital underwater acoustic communication due to the development of underwater acoustic wireless communication systems.

All what said above outline the importance of studying both the elastic wavefield propagation in complex 3-D media and the acoustic wavefield propagation in seawater. In particular the forward modelling, which is the calculation of theoretical wavefield starting from a given model, is an important tool for both seismological and underwater acoustic problems. For seismological problems the forward modelling can be of great support for the interpretation of data and to construct or to refine models of both the propagation medium and of the source. The calculation of the theoretical wavefield propagation in the

seawater is, instead, widely used for studying the effects on the data transmission produced by the variability in space and time of both the underwater environment and its boundaries (sea-surface and seafloor).

Many methods have been developed during the years in order to calculate the complete wavefield (i.e. solve the elastodynamic equations) both in simple structures, such as a layered medium, and in complex 3-D structures. In Chapter 1, section 1.2, a summary of these methods will be reported.

In this work we are interested to the high frequency elastic and acoustic wavefield propagation, which can be computed by approximate high-frequency asymptotic methods (such as ray methods). The high-frequency methods are preferable to direct numerical methods for many applications, both for the shorter computing times (direct numerical methods require large quantities of memory, computing time, and processor capacity) and for the full interpretability of the seismograms, since all the phases on a seismogram are relative to *a priori* known body waves. High frequency methods are preferable whenever a fast synthetic seismogram computation is needed, as in inversion procedures where an iterative forward modelling is required. In seawater ultrasonic frequencies are typically used to transmit data, so ray-theory method are widely used to study the propagation of these high-frequency signals.

Although methods based on ray theory give only an approximate solution of the elastodynamic equation, and they can be applied only if some general conditions are satisfied (see section 1.3.2), the computing time is order of magnitude less than that required by complete wavefield methods. Moreover the differences between the ray theory solution and the direct numerical solution of the elastodynamic equation become less and less as the frequency f tends to infinity ($f \to \infty$). The ray theory will be described in Chapter 1; a complete treatment of the theory can be found in Červený (2001).

Since the ray theory solution of the elastodynamic equation is composed of elementary body waves that travel through the medium from the source to the receiver, the wavefield will be computed only for the chosen body waves. The problem starts when we want to produce synthetic data as complete as possible by considering a large number of body waves. In this case the computation of the wavefield propagation using ray theory becomes tedious if an automatic body waves (raypaths and phases) generation will not be used.

In order to resolve the problem of generating a comprehensive set of raypaths and phases to be computed, we have developed and quantitatively tested a method that uses a hierarchical order of rays and seismic phases generation, taking into account some existence constraints for a ray-path and some physical constraints. The method has been implemented in the COMRAD code (from the Italian: "COdice Multifase per il RAy-tracing Dinamico"), written in Fortran77 language. The program's core is the dynamic ray-tracing method developed by Farra and Madariaga (1987). In Chapter 2 the description of the method with a discussion of its limits and its advantages will be presented. A quantitative test will be also reported. Further information of the COMRAD code (the user guide, the source code, and where they should be downloaded) can be found in Appendix A.

In Chapter 3 some applications of the COMRAD code in seismology will be presented. In particular applications to seismic reflection data, obtained from the SERAPIS (Zollo

et al., 2003) active survey, and the computation of synthetic seismograms generated by faulting sources will be discussed.

In Chapter 4 we will present a study on the physical properties of the seawater in the Gulf of Naples, considering both their spatial and temporal variability. We will show the effects they produce on the underwater acoustic digital communication at 100 kHz frequency and the limit of the transmission reliability in space and time. The underwater acoustic wave propagation in the geoacoustic model developed for the Gulf of Naples was computed using the COMRAD code. The study presented is a work carried out during this thesis by Stabile *et al.* (2007) for the Pon-MIUR SisMa project.

As we said before, the interpretation of the information that the wavefield propagation brings at the receiver is used to study the interior of the medium. So petroleum and mineral resource prospects, subsurface water, environmental pollution, archaeology objects, etc. can be found in the Earth and/or in the seawater, and imaging techniques can be used to reconstruct their shape.

In the seawater, the main advantage of acoustic imaging systems over the optical ones is that they properly work beyond the optical visibility range. Moreover they provides images of submerged object also in turbid waters. Thus, the development of an acoustic camera system, which gives a 3-D image of the insonified object, has becomes recently an active research field.

In Chapter 5 we will study the detection and imaging of objects submerged in the seawater, using acoustic signals around a frequency of 500 kHz, for the development of an acoustic imaging sysmet. Since we want to reconstruct a high resolution 3-D image of submerged not smoothed objects (such as blocks with corners or rough surfaces), the ray-theory is not valid yet. In this case scattering occurs and we use the Rayleigh approximation for the amplitude computation of the scattered wave. Using scattering theory we compute synthetic data as echoes to a receiver produced by a target modelled as a sum of little (i.e. much smaller than the characteristic wavelength of the wavefield) scattering point having the same physical properties of the target. The synthetic data are hence considered as real data to reconstruct the image of the target using beamforming techniques. This is an on-going work funded on Pon-MIUR STSS-500 project, which will be described in section 5.1.

Chapter 1

Wave propagation theory

Elastic waves are generated whenever a transient stress imbalance is produced within or on the surface of an elastic medium. Almost any sudden deformation or movement of a portion of the medium results in such a source, that can be external to the solid Earth or internal and can be natural of artificial. Except in the immediate vicinity of the source, the ground returns to its initial position after the transient motion has subsided. Vibration of this type involves small elastic deformations, or strains, in response to internal forces in the rock, or stresses. The properties of elastic waves are governed by the physics of elastic solids, which is fully described by the theory of elastodynamics.

In this chapter we briefly derive the elastodynamic equations and the wave equations. It is well known that analytical solutions to the elastodynamic equation can be found only for simple cases, but there are several techniques that can solve numerically the elastodynamic equations for more complex media. We will show an overview of these methods in the section 1.2. In particular we present in the section 1.3 the *ray theory*, which provides the solution to the elastodynamic equation in the high-frequency approximation.

Finally, when we want to take into account the presence in the medium of small[1] discrete inclusions, the scattering theory must be considered. In the last section of this chapter we present the scattering theory and, in particular, the Rayleigh scattering approximation that occurs when the size of heterogeneities is much smaller than the wavelength of the incident wave field.

1.1 Elastodynamic equations

The basic concepts and equations of linear elastodynamics have been explained in many textbooks, such as Atkin and Fox (1980), Ben-Menahem and Singh (1981), Lay and Wallace (1995), and Aki and Richards (2002).

Here we shall use the Lagrangian description of motion in an elastic continuum, in which the motion of a particular particle is followed as a function of time and space. This

[1] With small we intend that the size of the inclusion is of the order (or less) of the wavelength of the incident wave field.

is a natural system for seismology, because seismograms are essentially records of particle motions at near-surface sensors as seismic waves pass by. A continuum is a continuous distribution of particles; thus a vector field, $\mathbf{u}(\mathbf{x}, t)$, is required to describe the motions of every point in the medium, where we are free to choose a convenient reference system. Because we wish to make the treatment as simple as possible, we shall use Cartesian coordinates x_i, $i = 1, 2, 3$, and Cartesian tensors only.

Assume that the particle is located at the position described by Cartesian coordinates x_i at the reference time. The vector distance of a particle at time t from position $\mathbf{x}$ at the reference time is called the displacement vector $\mathbf{u} = \mathbf{u}(\mathbf{x}, t)$.

We denote the Cartesian components of the stress tensor by $\tau_{ij}(\mathbf{x}, t)$ and the Cartesian components of the strain tensor by $e_{ij}(\mathbf{x}, t)$. Both tensors are considered to be symmetric

$$\tau_{ij} = \tau_{ji}, \qquad e_{ij} = e_{ji}. \tag{1.1}$$

The strain tensor can be expressed in terms of the displacement vector as follows:

$$e_{ij} = \frac{1}{2}\left(u_{i,j} + u_{j,i}\right), \tag{1.2}$$

where the comma between subscripts is used for spatial derivatives (e.g. $u_{i,j} = \partial u_i / \partial x_j$). The stress tensor $\tau_{ij}(\mathbf{x}, t)$ fully describes the stress conditions at any point $\mathbf{x}$. It can be used to compute traction $\mathbf{T}$ acting across a surface element of arbitrary orientation at $\mathbf{x}$:

$$T_i = \tau_{ij} n_j, \tag{1.3}$$

where $\mathbf{n}$ is the unit normal to the surface element under consideration.

The elastodynamic equation relates the spatial variations of the stress tensor with the time variations of the displacement vector and its expression is:

$$\tau_{ij,j} + f_i = \rho \ddot{u}_i, \qquad i = 1, 2, 3. \tag{1.4}$$

Here f_i denote the Cartesian components of body forces (force per volume), and ρ is the density. The term with f_i in elastodynamic equation (1.4) will also be referred to as the source term. Quantities $\ddot{u}_i = \partial^2 u_i / \partial t^2$, $i = 1, 2, 3$, represent the second partial derivatives of u_i with respect to time (that is, the Cartesian component of particle acceleration $\ddot{\mathbf{u}}$). In a similar way, we shall also denote the Cartesian components of particle velocity $\partial u_i / \partial t$ by v_i or $\dot{u}_i$. The introduced quantities are measured in the following units:

- stress τ_{ij} and traction T_i in pascals (Pa),
- components of body forces f_i in newtons per cubic metre ($\mathrm{N/m^3}$),
- density ρ in kilograms per cubic metre ($\mathrm{kg/m^3}$),
- displacement components u_i in metres (m),
- strain components e_{ij} dimensionless.

In a linear, anisotropic, perfectly elastic solid, the constitutive stress-strain relation is given by the generalized Hooke's law (Aki and Richards, 2002; Červený, 2001):

$$\tau_{ij} = c_{ijkl} e_{kl}, \tag{1.5}$$

where c_{ijkl} are components of the elastic tensor, which has in general 81 components. These components[2], however, satisfy the following symmetry relations:

$$c_{ijkl} = c_{jikl} = c_{ijlk} = c_{klij}, \tag{1.6}$$

which reduce the number of independent components of the elastic tensor from 81 to 21. The components of the elastic tensor are measured in pascals (Pa), the same units as the stress components.

If we express e_{kl} in terms of the displacement vector components, see equation (1.2), and take into account symmetry relations (1.6), we can also express equation (1.5) in the following form:

$$\tau_{ij} = c_{ijkl} u_{k,l}. \tag{1.7}$$

Now, inserting relation (1.7) into elastodynamic equation (1.4), we obtain the elastodynamic equation for an unbounded anisotropic, inhomogeneous, perfectly elastic medium:

$$(c_{ijkl} u_{k,l})_{,j} + f_i = \rho \ddot{u}_i, \qquad i = 1, 2, 3. \tag{1.8}$$

The elastodynamic equation (1.8) represents a system of three coupled partial differential equations of the second order for three Cartesian components $u_i(x_j, t)$ of the displacement vector $\mathbf{u}$.

Alternatively, the elastodynamic equation may be expressed in terms of 12 partial differential equations of the first order in three Cartesian components $v_i(x_j, t)$ of the particle velocity vector $\mathbf{v} = \dot{\mathbf{u}}$, and 9 components τ_{ij} of the stress tensor (see Červený, 2001).

The elastodynamic equation (1.8) can be expressed also in the frequency domain by applying the Fourier transform operator $\mathcal{F}$ to $\mathbf{u}(\mathbf{x}, t)$ and $\mathbf{f}(\mathbf{x}, t)$, and taking into account the generalized derivative property of the Fourier transform[3]. Hence, in the frequency domain the equation (1.8) becomes:

$$(c_{ijkl} U_{k,l})_{,j} + F_i = -\rho \omega^2 U_i, \qquad i = 1, 2, 3. \tag{1.9}$$

where $\mathbf{U}(\mathbf{x}, \omega)$ and $\mathbf{F}(\mathbf{x}, \omega)$ are the Fourier transform of $\mathbf{u}(\mathbf{x}, t)$ and $\mathbf{f}(\mathbf{x}, t)$, respectively.

[2]The components c_{ijkl} of the elastic tensor are also called elastic constants, elastic moduli, elastic parameters, or stiffnesses.

[3]Considering $g(t)$ an integrable function of time t, $G(\omega)$ its Fourier transform, and $\mathcal{F}$ the Fourier transform operator, the Fourier transform of the n^{th} derivative of $g(t)$ satisfies the following property:

$$\mathcal{F}\left[\frac{d^n(g(t))}{dt_n}\right] = (i\omega)^n G(\omega),$$

with ω the angular frequency.

In the case of an isotropic medium the number of the independent components c_{ijkl} of the elastic tensor is reduced from 21 to only 2, infact:

$$c_{ijkl} = \lambda\delta_{ij}\delta_{kl} + \mu(\delta_{ik}\delta_{jl} + \delta_{il}\delta_{jk}) \tag{1.10}$$

where λ and μ are the Lame's elastic parameters used to describe an isotropic medium, and δ_{ij} is the Kronecker's symbol. In particular μ is the rigidity or shear modulus and it is equal to zero in fluids.

Taking into account the equation (1.10), the elastodynamic equation (1.8) in an isotropic medium becomes:

$$(\lambda u_{j,j})_{,i} + [\mu(u_{i,j} + u_{j,i})]_{,j} + f_i = \rho\ddot{u}_i, \qquad i = 1, 2, 3. \tag{1.11}$$

The solution of the elastodynamic equations (1.8) and (1.11) for anisotropic and isotropic unbounded media, respectively, results in a term that behaves like r^{-2} and in terms that behave like r^{-1}. The terms that behave like r^{-1} becoming dominant (over r^{-2}) as $r \to \infty$, and therefore they are called far-field terms. On the other hand, since the r^{-2} term dominates over r^{-1} terms as $r \to 0$, it is called the near-field term. All these terms are body (or volume) waves that travel through the interior of the unbounded medium. If there are discontinuities in the medium and/or boundaries, additional waves will be generated, such as reflected/transmitted/converted body waves, surface waves (which travel on the surface of the medium), headwaves, inhomogeneous waves, etc. Details can be found in Lay and Wallace (1995) and Aki and Richards (2002) books.

1.2 Synthetic Seismogram Methods

The seismogram (Figure 1.1) is the recording, during the time t, of the ground motion by instruments called seismometers installed in a certain point x of the propagation medium. In particular, in Figure 1.1 the principal seismic phases are indicated. On the vertical component (top) we indicate the P-wave (also called longitudinal or compressional wave) which in general corresponds to the first arrival[4] on the seismograms. The P-wave is linearly polarized longitudinally to the direction of the wavefield (or equivalently, perpendicularly to its wavefronts). The P-wave can be used for several problems, such as tomography, source localization, focal mechanisms of the seismic source, earthquake magnitude estimation.

For the same problems it is possible to use S-waves (the first S-wave arrival is indicated on the E-W component of the seismogram plotted in Figure 1.1) instead or in addition to P-waves. The S-wave (also called shear wave) is polarized in the plane tangent to the wavefronts, its velocity is always smaller than the P-wave velocity, and its polarization is in general elliptical. Brune (1970) demonstrated that the spectra of seismic shear waves (not

[4]For large offsets (horizontal distance between the source and the receiver) the first arrival can be a headwave and not the direct P-wave. In particular cases (layers with slow velocities above layer with very high velocities) and for large offsets also some reflected waves to the deepest interfaces should arrive before the direct P-wave.

only the first S-wave arrival) can be used to calculate the seismic moment M_0. Generally, P and S wavefields are not separated in inhomogeneous structures.

Between P and S waves, and after S waves, there are several reflected/refracted and(or) converted waves which carry important information on the medium crossed by the wavefield. This phases are used is seismic reflection to find in the medium gas-bearing formations, reservoirs, discontinuities and interfaces.

Finally, also the coda of the seismic signal (evidenced on the E-W component of the seismogram in Figure 1.1), and other type of phases (i.e. the surface waves or the headwaves) are used to study the medium properties and/or the source.

In summary the entire seismogram waveform can be studied to reconstruct both the characteristics of the source that has generated the wavefield and the properties of the medium the wavefield has propagated throughout. For this reason it is important to treat mathematically the process of excitation, propagation, and recording of seismic waves in order to correlate the shape and the amplitude of the recorded seismic waves to their physical meaning.

Because of the nature of the Earth, which is considered as a linear stationary filter for elastic waves, it is possible to treat mathematically the process of excitation, propagation, and recording of seismic waves as a sequence of linear filters that combine to produce

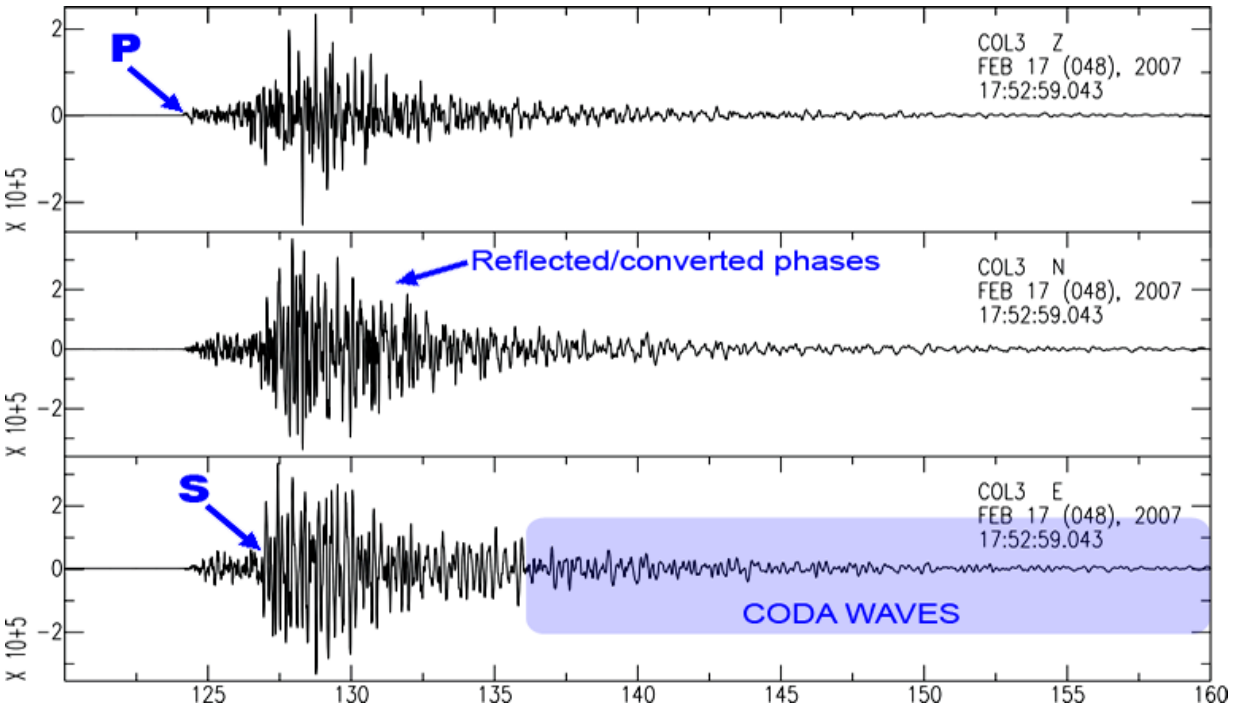

Figure 1.1: *An example of seismogram for an earthquake of magnitude M=4.0 recorded by a three component station of the ISNet network (Weber* et al.*, 2007) installed in the Irpina region (Southern Italy). The principal seismic phases are indicated. From top to bottom the vertical component, the N-S component, and the E-W component are shown, respectively.*

observed seismograms. In other words, an observed ground displacement history, u(t), can be expressed as the result of a source function, s(t), operating on a propagation function, g(t), combined with an instrument recording function, i(t), by the convolution operation:

$$u(t) = s(t) * g(t) * i(t) \tag{1.12}$$

It is also possible to model each of these effects mathematically, and develop a procedure to predict the character of a seismogram in a realistic model of the Earth. Such a mathematical construction is known as a synthetic seismogram. The formalism of comparing synthetic and observed seismograms is known as waveform modelling. Waveform modelling has become one of the most powerful tools available to seismologists for refining Earth structure models and understanding fault rupture processes. For this reason a method for rapid high frequency seismogram calculation is developed during this thesis work and it will be described in Chapter 2.

Here we summarize the most important methods used to compute synthetic seismograms with their advantages and disadvantages:

- **The Normal Mode summation method** utilize the dispersion relations and amplitude functions (eigenvalues) for Rayleigh or Love motion to determine the amplitude and phase spectrum for a layered (1-D) half space at a given distance. Fourier transformation then yields the synthetic surface wave seismograms. A large number of modes can be included. Body wave arrivals can be calculated if sufficiently high mode number is used. This implies that the method must sum a large number of modes to approximate broadband data and body waves. Numerical effects due to high mode number and long period require large number of layers in model which can increase computational effort significantly.

- **The Discrete wavenumber method** is based on a discrete horizontal wave-number representation of seismic source wave fields with the seismic source embedded in a layered (1-D) medium. The principle of the method is founded of the fact that the steady-state radiation from a line source in an infinite homogeneous medium can be represented as a cylindrical wave or, equivalently, as a continuous superposition of homogeneous and inhomogeneous plane waves (Bouchon and Aki, 1977). Therefore, denoting by x and z the horizontal and vertical axes in the plane normal to the source axis, any observable such as displacement or stress can be written in the form of an integration with respect to the horizontal wave number. The integral is then transformed into a summation of functions of discrete wavenumbers. The computation time increases with increasing frequency since more wavenumbers have to be considered in the summation. A program based on this method will be used in the Chapter 2 as reference for testing the COMRAD code developed during this thesis work.

- **The finite-difference method** belongs to the so-called grid-point methods. In the grid-point methods a computational domain is covered by a space-time grid and each

function is represented by its values at grid points. The space-time distribution of the grid points may be, in principle, arbitrary, but it significantly affects the accuracy of the approximation. Usually, no assumption is made about the values in-between the grid points. A derivative of a function is approximated by the finite-difference formula which uses values of the function at a specified set of the grid points. Grid spacing (10 points per wavelength) and time step (small step to insure stability) requirements result in very large computation time and storage use. This method is applicable in 3-D models with arbitrary complex local structures and the solution obtained should contain all the possible waves propagating in the given medium within the given time window.

- **The finite-element method**, as the finite-difference method, provides the direct numerical solution of partial differential equations (i.e. the wave equation) by finite-element matrix methods. The solution approach is based either on eliminating the differential equation completely (steady state problems), or rendering the partial differential equations into an approximating system of ordinary differential equations. The finite-element method is a good choice for solving partial differential equations over complex domains, when the domain changes, or when the desired precision varies over the entire domain. The method needs the discretization of the space in elements (in general triangles in 2-D or tetrahedrons in 3-D) and piecewise polynomial (in general linear) basis functions in order to replace the infinite dimensional problem with a finite dimensional version. Finite element matrices are typically banded (elements are locally connected) and the storage requirements for the system matrices typically grow quite linearly with the problem size, so for models with high complexity large banded matrices must be inverted. Methods that use higher degree piecewise polynomial basis functions are often called **spectral element methods**, especially if the degree of the polynomials increases as the triangulation size goes to zero.

- **The boundary element method** is another numerical computational method of solving partial differential equations which have been formulated as integral equations (i.e. in boundary integral form) that are mathematically equivalent to the original partial differential equations. The essential re-formulation of the partial differential equation consists of an integral equation that is defined on the boundary of the domain and an integral that relates the boundary solution to the solution at points in the domain. The boundary element method is often more efficient than other methods for problems where there is a small surface/volume ratio but, on the other hand, the method formulations typically give rise to fully populated matrices. This means that the storage requirements and computational time will tend to grow according to the square of the problem size.

- **The asymptotic ray method** is an approximate high frequency method based on an asymptotic solution of the elastodynamic equation. The solution is sought in the form of the ray-series and considering zero-order terms which dominates over the high order terms as the frequency tends to infinity. For this reason the solution

of the elastodynamic equation is only approximate, but the errors become small if the frequency is high (asymptotic solution). The method is very general since in can be applicable both to anisotropic and isotropic media containing curved interfaces, separating layers or block in the space, to arbitrary 3-D variations of elastic parameters and density, to very general types of body waves, and to an arbitrary source-receiver configuration. On the other hand some kind of waves (such as surface waves, inhomogeneous waves, near-field terms, head-waves) cannot be considered by the method. Although the method is in principle incomplete, it can be applicable to a large variety of problems and it is the most effective method in term of computing time. In fact the computing time does not depend from frequency and the results accuracy increases with increasing frequency.

1.3 Ray-Theory

This section presents a simple treatment of the ray method, applicable to high-frequency body waves propagating in complex 3-D laterally varying media. Here we follow and use the notations of Červený (2001), and we discuss the mathematical derivation of the zero-order ray solution (we remind to Brokešová (2006) for a complete treatment of zero-order ray solution, and Červený (2001) for a consistent treatment of the ray methods).

1.3.1 Mathematical derivation

The high frequency asymptotic methods are based on an asymptotic solution of the elastodynamic equation. They can be applied to compute not only rays and travel times (kinematic part) but also the vectorial complex-valued amplitudes of the displacement vector (dynamic part).

The final ray solution of the elastodynamic equation is composed of elementary waves (direct, reflected, refracted, multiply reflected, converted, and the like) corresponding to various rays connecting the source to the receiver. In most cases, the numerical modelling of seismic wavefields has been based on the zeroth-order leading term of the ray series.

In practice ray theory is based on the assumption that the displacement vector $\mathbf{u}$ is assumed in the form of the so-called ray series. Hence, the ansatz solution for the displacement vector $\mathbf{u}$ of the elastodynamic equations (1.8) or (1.11) at point $\mathbf{x}$ and time t will read

$$\mathbf{u}(\mathbf{x},t) = \sum_{k=0}^{\infty} \mathbf{U}_k(\mathbf{x}) F_k(t - \tau(\mathbf{x})) \tag{1.13}$$

where $\mathbf{U}_k$ is the k^{th} vectorial amplitude coefficient (a complex-valued function), τ is the eikonal (a real-valued function), and F_k $(k = 1, \ldots, \infty)$ represent high-frequency analytical[5] signals. The analytical signals in wave propagation problems are just the way to allow for suitable compact notation and to make mathematics simpler; moreover at the

[5]The analytical signal in any complex-valued function whose real and imaginary parts form a Hilbert

end of an analytical signal computation one must take only the real part of the analytical signal to obtain the physically meaningful quantity for which the problem is solved (i.e. the displacement). Finally, the advantage of the analytical signal is that it has a one-sided spectrum since its Fourier transform vanishes for negative frequencies.

Using the ray series the $\mathbf{U}_k$ ($k = 1, \ldots, \infty$) and the eikonal τ become the functions to be determined under the condition (1.8) in anisotropic media, or the condition (1.11) in isotropic media. These quantities are assumed to change only slowly in space. Since we are interested to the wavefield solution in a certain point $\mathbf{x}$ far from the source, we shall not consider the source term ($f_i = 0$, $i = 1, \ldots, 3$) in the elastodynamic equations (1.8) and (1.11).

The zero-order ray solution is obtained considering only the first term ($k = 0$) of the ray series (1.13), which is equivalent to the asymptotic high frequency solution of the elastodynamic equation:

$$\mathcal{F}\left[\mathbf{u}_{k=0}(\mathbf{x},t) = \mathbf{U}_0 F_0(t-\tau(\mathbf{x})\right] = \mathbf{U}_0(\mathbf{x}) e^{-i\omega\tau(\mathbf{x})} \equiv \lim_{\omega\to\infty} e^{-i\omega\tau(\mathbf{x})} \sum_{k=0}^{\infty} \frac{\mathbf{U}_k(\mathbf{x})}{(-i\omega)^k} \tag{1.14}$$

where the last quantity is the Fourier transform of the ray series (1.13).

Omitting the index "0" in F_0 and $\mathbf{U}_0$, the zero-order trial ray solution can be written af follows:

$$\mathbf{u}(\mathbf{x},t) = \mathbf{U} F(t-\tau(\mathbf{x})) \tag{1.15}$$

where the eikonal function τ is interpreted as travel-time of the elementary wave for which the solution is constructed. Moreover, surfaces $\tau(\mathbf{x}) = const$ represent wavefronts while the gradient of the eikonal $\mathbf{p} = \nabla\tau$ is the slowness vector and it is perpendicular to the wavefront:

$$p_i(\mathbf{x}) = \tau_{,i}(\mathbf{x}) = \frac{n_i^\tau(\mathbf{x})}{c(\mathbf{x})}, \quad i = 1, \ldots, 3 \tag{1.16}$$

with $\mathbf{n}^\tau$ the unit vector perpendicular to the wavefront and c the phase velocity.

Substituting now the zero-order ray ansatz (1.15) in the equation (1.8) or (1.11) without the source term and gathering the terms with the same derivative of F, we have the following equation for both the anisotropic and isotropic cases:

$$\ddot{F} N_i(\mathbf{U}, \nabla\tau) - \dot{F} M_i(\mathbf{U}, \nabla\tau) + F L_i(\mathbf{U}) = 0, \quad i = 1, \ldots, 3 \tag{1.17}$$

where the vectorial coefficients N, M, and L have different expressions for anisotropic and isotropic cases. In particular for anisotropic structures the three coefficients are given by

---

pair:

$$F(t) = f(t) + i\mathcal{H}[f(t)]$$

where $f(t)$ is a real-valued function and $\mathcal{H}$ is the Hilbert's transform operator. As an example the exponential function $\exp(\omega t) = \cos(\omega t) + i\sin(\omega t)$ is the special case of the analytical function (with $\sin(\omega t) = \mathcal{H}[\cos(\omega t)]$).

the relations

$$\begin{cases} N_i(\mathbf{U}, \nabla\tau) = c_{ijkl}\tau_{,l}\tau_{,j}U_k - \rho U_i \\ M_i(\mathbf{U}, \nabla\tau) = c_{ijkl}\tau_{,j}U_{k,l} + (c_{ijkl}\tau_{,l}U_k)_{,j} \\ L_i(\mathbf{U}, \nabla\tau) = (c_{ijkl}U_{k,l})_{,j} \end{cases} \tag{1.18}$$

while for isotropic media they are given by the relations

$$\begin{cases} N_i(\mathbf{U}, \nabla\tau) = (\lambda+\mu)U_j\tau_{,i}\tau_{,j} + \mu)U_i\tau_{,j}\tau_{,j} - \rho U_i \\ M_i(\mathbf{U}, \nabla\tau) = (\lambda+\mu)(U_{j,i}\tau_{,j} + U_{j,j}\tau_{,i} + U_j\tau_{,ij}) + \mu(2U_{i,j}\tau_{,j} + U_i\tau_{,jj}) + \\ \qquad +\lambda_i U_j\tau_{,j} + \mu_{,j}U_i\tau_{,j} + \mu_{,j}U_j\tau_{,i} \\ L_i(\mathbf{U}, \nabla\tau) = (\lambda+\mu)U_{j,ij} + \mu U_{i,jj} + \lambda_{,i}U_{j,j} + \mu_{,j}(U_{i,j} + U_{j,i}) \end{cases} \tag{1.19}$$

The equation (1.17) must be satisfied at any time t and any point x and, because of different orders of derivatives of F, it will be done only setting to zero both **N**, **M**, and **L** coefficients. In general the second (**M**) and third (**L**) term of equation (1.17) do not vanish, but in high frequency approximation the error is presumably small although the equation of motion can not be satisfied completely.

In the frequency domain the equation (1.17) can be written, away from the source term and considering the derivative property of the Fourier transform, as

$$-\omega^2 N_i(\mathbf{U}, \nabla\tau) - i\omega M_i(\mathbf{U}, \nabla\tau) + L_i(\mathbf{U}) = 0 \tag{1.20}$$

hence the first two terms dominate over the third if the frequency is high, so only the first two terms are used to determine the eikonal and the ray amplitude.

Taking into account this consideration, we have to solve the following system:

$$\begin{cases} \mathbf{N}(\mathbf{U}, \nabla\tau) = \mathbf{0} \\ \mathbf{M}(\mathbf{U}, \nabla\tau) = \mathbf{0} \end{cases} \tag{1.21}$$

The first condition, $\mathbf{N} = \mathbf{0}$, results in the eikonal equation, a nonlinear partial differential equation for $\tau(\mathbf{x})$ that constrains also the polarization of **U**. The magnitude of **U** (one scalar quantity) can be determined from the transport equation, which is derived by projecting the vector **M** into the direction (polarization) of **U**.

Eikonal equation

We now solve the eikonal equation $\mathbf{N} = \mathbf{0}$ introducing the Christoffel matrix $\widehat{\mathbf{\Gamma}}$ with elements Γ_{ik} as

$$\Gamma_{ik} = \frac{c_{ijkl}}{\rho}\tau_{,j}\tau_{,l} \tag{1.22}$$

for anisotropic media (note that $\tau_{,i}$, $i = 1, 2, 3$, is the i^{th} component of the slowness vector **p**) while for isotropic media they can be written as

$$\Gamma_{ij} = \frac{\lambda+\mu}{\rho}\tau_{,i}\tau_{,j} + \frac{\mu}{\rho}\delta_{ij}\tau_{,k}\tau_{,k} \tag{1.23}$$

The Christoffel matrix $\widehat{\mathbf{\Gamma}}$ has many useful properties (see Červený (2001)) and simplifies both the eikonal equations for isotropic and anisotropic media into the simple compact form

$$(\Gamma_{ij} - \delta_{i,j})U_j = 0, \qquad i = 1, 2, 3 \tag{1.24}$$

Representing the ray amplitude $\mathbf{U}$ by the use of the scalar amplitude factor A and the corresponding unit polarization vector $\mathbf{g}$, so $U_i = Ag_i$, the equation (1.24) yields

$$(\Gamma_{ij} - \delta_{i,j})g_j = 0 \tag{1.25}$$

that can be viewed as a typical eigenvalue problem for the Christoffel matrix

$$(\Gamma_{ij} - G\delta_{i,j})g_j = 0 \tag{1.26}$$

with G being a general eigenvalue. The eikonal equation (1.25) is equivalent to the equation (1.26) under the condition $G = 1$, thus determining the eigenvalues of the matrix $\widehat{\mathbf{\Gamma}}$ and equating them to unity, we obtain the eikonal equation. The Christoffel matrix has, in general, three eigenvalues $G_1(x_i, p_i)$, $G_2(x_i, p_i)$, and $G_3(x_i, p_i)$, and three eigenvectors $\mathbf{g}^{(1)}(x_i, p_i)$, $\mathbf{g}^{(2)}(x_i, p_i)$, and $\mathbf{g}^{(3)}(x_i, p_i)$.

Once the eigenvalues and eigenvectors are evaluated, we can see that for a given anisotropic medium three independent linearly polarized body waves may propagate in it. These are the quasi-P (qP) and quasi-S (qS_1 and qS_2) waves. Their amplitudes are given as

$$\mathbf{U}^{(m)}(\mathbf{x}) = A^{(m)}(\mathbf{x})\mathbf{g}^{(m)}(\mathbf{x}) \tag{1.27}$$

and their travel times $\tau^{(m)}$ must satisfy the eikonal equation

$$G_m(x_i, p_i) = 1 \tag{1.28}$$

In the case of an isotropic medium, the Christoffel matrix has again three eigenvalues but two of them coincide. The expressions of these eigenvalues are

$$G_1(x_i, p_i) = G_1(x_i, p_i) = \beta^2(x_i)p_i p_i, \qquad G_3(x_i, p_i) = \alpha^2(x_i)p_i p_i \tag{1.29}$$

where $\alpha(x_i)$ and $\beta(x_i)$ are given by the relations

$$\alpha(x_i) = \sqrt{\frac{\lambda(x_i) + 2\mu(x_i)}{\rho(x_i)}}, \qquad \beta(x_i) = \sqrt{\frac{\mu(x_i)}{\rho(x_i)}} \tag{1.30}$$

The eigenvector $\mathbf{g}^{(3)}$ corresponding to the eigenvalue G_3 has the same direction as the slowness vector $\mathbf{p}$, while the eigenvectors $\mathbf{g}^{(1)}$ and $\mathbf{g}^{(2)}$ corresponding to the two coinciding eigenvalues $G_1 = G_2$ are mutually orthogonal unit vectors, also perpendicular to $\mathbf{p}$, but they cannot be determined uniquely from the equation (1.26). Once the eigenvalues and the eigenvector are evaluated, for the isotropic case we have a P wave with the amplitude

$$\mathbf{U}^{(P)}(\mathbf{x}) = A^{(3)}(\mathbf{x})\mathbf{g}^{(3)}(\mathbf{x}) \tag{1.31}$$

which is linearly polarized perpendicularly to its wavefronts, and the S wave which is elliptically polarized in the plane tangent to the wavefronts with the amplitude

$$\mathbf{U}^{(S)}(\mathbf{x}) = A^{(1)}(\mathbf{x})\mathbf{g}^{(1)}(\mathbf{x}) + A^{(2)}(\mathbf{x})\mathbf{g}^{(2)}(\mathbf{x}) \tag{1.32}$$

Transport equation

Now we solve the transport equation which can be derived from the second equation of the system (1.21) inserting into equation $\mathbf{M} = \mathbf{0}$ the expression (1.27) for anisotropic media or, in the case of isotropic media, the expression (1.31) and the expression (1.32) for the P wave and the S wave, respectively. This means that the only quantities to be determined are the scalar, complex-valued, amplitude factors $A^{(m)}$.

For anisotropic media, multiplying the obtained equation by $g_i^{(m)}$, after some algebra (see Červený (2001)) we have

$$M_i(A^{(m)}\mathbf{g}^{(m)})g_i^{(m)} = 2c_{ijkl}p_j g_i^{(m)} g_k^{(m)} A_{,l}^{(m)} + A^{(m)}(c_{ijkl}p_l g_k^{(m)} g_i^{(m)})_{,j} = 0 \tag{1.33}$$

where the index $m = 1, 2, 3$. Moreover,introducing the vector $\mathbf{v}^{(m)}$ with components

$$v_i^{(m)} = \frac{1}{\rho} c_{ijkl} p_l g_k^{(m)} g_j^{(m)} \tag{1.34}$$

the equation (1.33) becomes

$$(\rho A^{(m)} A^{*(m)} v_i^{(m)})_{,i} = 0 \tag{1.35}$$

where $A^{*(m)}$ is the complex conjugate of $A^{(m)}$ and the vector $\mathbf{v}^{(m)}$ has the meaning of a group velocity. The vector in parentheses in the equation (1.35) is the energy flux, so that the equation (1.35) represents conservation of energy along rays.

Because the anisotropic medium includes as special case the isotropic medium, the procedure for deriving the transport equation in isotropic structures is analogous and finally we have transport equations for the P wave and the S wave in the form similar to equation (1.35). In particular the transport equation for the P wave will be

$$(\rho A^{(3)} A^{*(3)} \alpha^2 p_i)_{,i} = 0 \tag{1.36}$$

with α the P-wave phase velocity, and its expression is given by the first equation in (1.30), while the system of transport equations for the S wave will be

$$\begin{cases} (\rho A^{(1)} A^{*(1)} \beta^2 p_i)_{,i} = 0 \\ (\rho A^{(2)} A^{*(2)} \beta^2 p_i)_{,i} = 0 \end{cases} \tag{1.37}$$

with β the S-wave phase velocity, and its expression is given by the second equation in (1.30).

It is possible to demonstrate[6] that the solution of the transport equation (1.35) in anisotropic media can be written in a form that relates the scalar amplitude factor $A^{(m)}(R)$ at a given point R on the ray (R stands for the receiver point) to the scalar amplitude factor $A^{(m)}(S)$ at a reference point S on the same ray (S stands for the source point):

$$A^{(m)}(R) = A^{(m)}(S)\sqrt{\frac{\rho(S)v^{(m)}(S)J(S)}{\rho(S)v^{(m)}(S)J(S)}}, \qquad m = 1, 2, 3 \tag{1.38}$$

[6]We remind the reader to Červený (2001) for the demonstration. Moreover, a step by step demonstration will be found in Brokešová (2006).

where $v^{(m)}$ is the group velocity along the ray of the considered wave, ρ is the density, and J is the ray Jacobian[7] of transformation from coordinates x_i to ray-coordinates γ_i. The above equation is the most common form of the continuation formula in anisotropic models. The equation (1.38) is valid also for isotropic media, substituting in the equation the group velocity $v^{(m)}$ with α for P waves or β for S waves.

Finally we want to drive the attention on the regularity of the ray-coordinates system, which is guaranteed whenever the Jacobian J does not vanish. In complex media the Jacobian vanishes on caustics so, from equation (1.38), the ray amplitude in a caustic point grows to infinity. This means that ray methods fail in caustics.

1.3.2 Ray theory general validity conditions

The asymptotic ray theory is based on the asymptotic ray series for high frequencies ($\omega \to \infty$), or alternatively, for small wavelengths ($\lambda \to 0$). In practical seismic applications the maximum frequency is of a finite value, so it would be very useful to know the validity conditions under which the ray method can be applied to compute seismic wavefields. The applicability of the asymptotic ray theory is limited by several qualitative conditions, usually formulated as certain inequalities for the frequency of the wavefield or alternatively, for the wavelength.

The following three general validity conditions, formulated using the wavelength λ in a qualitative way, are presented by Červený (2001) in the following way:

1. The wavelength λ of the wave under consideration must be considerably smaller than any characteristic quantity of length dimension l_i ($i = 1, \ldots, n$, with n the number of these quantities) in the problem under study:

$$\lambda \ll l_1, \ldots, l_n \tag{1.39}$$

   Among these quantities there are, for example, dimensions of the model, source-receiver distance, layer thicknesses h_k ($k = 1, \ldots, K$ with K being the number of layers in the model), radii of curvature of structural interfaces K_j ($j = 1, \ldots, K-1$), but also the scale length of inhomogeneities of the medium of type $v/|\nabla v|$ (with v being α or β, the P or S wave speed, respectively), $\rho/|\nabla\rho|$, where ρ denotes density, and so on. The condition (1.39) expresses the high-frequency character of the wavefield.

2. The ray method fails in the vicinity of surfaces S along which the ray field of the wave under study is not regular, like a caustic surface or a shadow zone boundary. Hence, the wavefield has to be computed not closer to these surfaces, but at a distance r from the surface S which satisfies the following condition:

$$\lambda \ll r \tag{1.40}$$

[7] The square root $\sqrt{J}$ of the Jacobian is called Geometrical Spreading.

3. The ray method is not applicable when the length L of the ray trajectory of the wave under consideration between the source and the receiver is too large. The estimates based on the theorem of mean value lead to the condition

$$\lambda \ll l_0^2/L \tag{1.41}$$

where l_0 has the same meaning as l_j in the first condition.

Because of the high-frequency character of the wavefield, it is impossible to remove these limitations. It is only possible to specify in a more quantitative way these three qualitative conditions. In particular for the condition (1.39), some authors like Beydoun and Keho (1987) propose the value of order of units (up to ten times) that guarantee the inequalities to be satisfied. This evaluation is still commonly used in modelling the medium for high frequency studies.

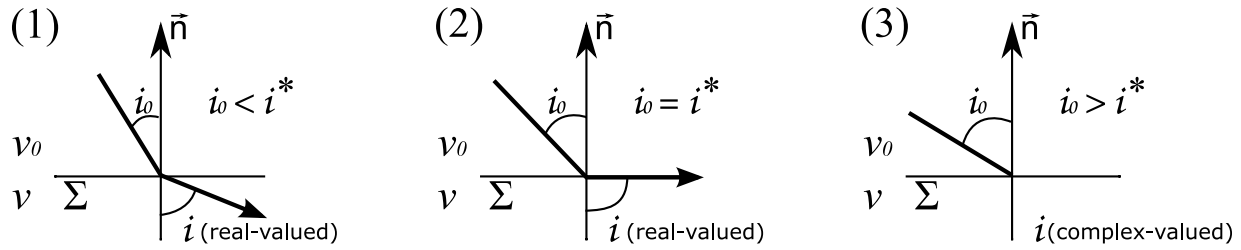

Figure 1.2: *Subcritical (1), critical (2), and postcritical (3) angles of incidence i_0. For the subcritical angle of incidence i_0, the R/T angle i and the corresponding ray are real-valued, see (1). For the critical angle of incidence $i_0 = i^*$, a headwave will be generated, see (2). For the postcritical angle of incidence i_0, the R/T angle i and the corresponding ray are complex-valued, see (3).*

A brief summary of the most common situations in which the ray theory may fail is now reported:

- **Postcritical incidence and inhomogeneous waves.** Indicating with i_0 the angle of incidence of the wavefield (which propagates with a velocity v_0) at an interface Σ and with i the angle of reflection or transmission of the wavefield (which propagates with a velocity v) at that interface, by the standard Snell's law we have $\sin i = (v/v_0)\sin i_0$. For $\sin i_0 > v_0/v$, both the angle i, the eikonal and the components of the slowness vector p_i become complex-valued. The waves relative to this case, called inhomogeneous or evanescent, exist but cannot be computed by the standard ray method and the angle of incidence i_0 is postcritical (see Figure 1.2).

- **Ray tangent to an interface locally or globally.** Using the same notation of the previous point, for $\sin i_0 = v_0/v$, the angle of incidence i_0 is critical[8], and the ray

[8]The angle of incidence i_0 such that the reflected angle $i = \pi/2$ (and so $\sin i_0 = v_0/v$) is called critical angle, and is generally written as i^*.

is globally tangent to the interface (see Figure 1.2). The generated waves propagate with velocity v along the interface Σ, and they are the so-called headwaves. For this kind of waves the rays could be formally traced but their amplitudes cannot be computed by the standard zero-order ray method as the waves belong to the class of high-order waves. In the case of a ray locally tangent to an interface Σ (when the angle of incidence $i_0 = \pi/2$) the ray can be traced, but the wavefield is singular beyond the point at which the ray touches the interface. A shadow zone is usually formed beyond the tangent point, in the region between the ray and the interface, and the ray itself becomes a boundary ray separating the shadow and illuminated region. Various waves with diffractive nature penetrate into the shadow zone, but the standard ray method is not capable to handle them.

- **Caustics.** Caustic surfaces are envelopes of rays. We have seen at the end of section 1.3.1 that the Jacobian J of the transformation into ray coordinates becomes equal to zero at a caustic point, so the ray theory predicts infinite amplitudes at this point. At any point situated close to the caustic surface on its illuminated side, there are always at least two intersecting rays, one approaching the caustics ant the other leaving it. The wavefield is anomalous in the vicinity of the caustic point but not along the whole ray, in fact at larger distances from this point the wavefield is again regular.

- **Fine layers and regions of high velocity gradient.** If in a model there are layers too thin with respect to the wavelength, the ray theory general validity conditions are not fulfilled. These conditions are not satisfied also in regions of high velocity gradient. Although in the latter case the ray can be formally traced, the wavefield computations will be low.

- **Large curvature of interfaces.** The presence of interfaces with large curvature with respect to the wavelength does not meet the ray theory general validity conditions. The rays of reflected/transmitted waves can be traced but the wavefield computations will be inaccurate.

- Objects with dimensions smaller or comparable to the wavelength. In the case of the presence in the model of small objects with dimensions equal or small than the wavelength under consideration, these objects act as scatterers. The scattered wavefield cannot be calculated by the ray methods.

Much of these problems can be treated using extensions of the ray method. As an example, the headwaves can be treated using the high order terms of the ray series (1.13).

In the next section, instead, we will discuss the case of objects in the medium which act as scatterers. In particular, the calculation of the amplitudes for the Rayleigh scattering case will be treated.

1.4 Rayleigh Scattering

Seismic waves are scattered at small-scale inhomogeneities (with respect to the wavelength) when propagating through complex media. These heterogeneities include velocity and density fluctuations of smaller scales down to microscopic pores, fractures and cracks. Such small-scale structures cannot be resolved deterministically by seismic surveys but, nevertheless, they have significant effects on seismic wave propagation because they scatter the incident seismic wave into all directions.

Indicating with a the characteristic length of a subsurface structure and with $k = 2\pi/\lambda$ the wavenumber relative to the dominant wavelength λ of the wavefield, the ray theory validity condition (1.39) gives $ka \gg 10$. The quantity ka is called the normalized frequency. For regions such that their characteristic length is of the order of the wavelength of the incident wavefield ($ka < 10$), the assumptions of the ray approximation break down and scattering occurs. Hence, as the value of ka becomes smaller and smaller, subsurface structures will tend to scatter rather then reflect the seismic wave field.

In the case the wavelength λ is of the order to the size a of the object ($ka \approx 1$), we enter the regime of resonance or Mie scattering.

If the wavelength of the incident wave field is much greater than the inclusion itself ($ka \ll 1$), the scattering can be described by the Rayleigh scattering theory (Müller, 2000). In the particular case of a weak (low parameter contrast between the object and the medium) single scattering, it is possible to treat this case also using the Born approximation (Gubernatis *et al.*,1977; Bohlen,2004).

Let us now consider small spheres in the medium with a diameter $2a$ such that $2ka \ll 1$ and with arbitrary contrasts in the material parameters. The scattered wavefields $\mathbf{u_p}$ and $\mathbf{u_s}$ for an incident P-wave, using Rayleigh approximation (Müller, 2000), are respectively:

$$\begin{cases} \mathbf{u_p} = R_p(A\cos^2\theta + B\cos\theta + C)\hat{r} \\ \mathbf{u_s} = R_s(D\sin 2\theta - B\sin\theta)\hat{\theta} \end{cases} \tag{1.42}$$

where r is the distance and θ is the scattering angle. R_p and R_s indicate the quantities

$$R_p = k_p^2 \frac{V}{4\pi}\frac{e^{-ik_p r}}{r}, \qquad R_s = k_s^2 \frac{V}{4\pi}\frac{e^{-ik_s r}}{r} \tag{1.43}$$

with $V = \frac{4}{3}(\pi a^3)$ the volume occupied by the spherical inclusion. The dynamic character-

istics are governed by the parameters A, B, C, and D, which are explicited as follows:

$$\begin{aligned} A &= -2\left(\frac{\mu'}{\mu}-1\right)\frac{\gamma^2}{\Gamma} \\ B &= \frac{\rho'}{\rho}-1 \\ C &= -\frac{1}{2}\frac{\frac{3}{2}(\lambda'-\lambda)+(\mu'-\mu)}{\frac{1}{2}\left(\frac{3}{2}\lambda'+\mu'\right)+\mu}+\frac{2}{3}\left(\frac{\mu'}{\mu}-1\right)\frac{\gamma^2}{\Gamma} \\ D &= \left(\frac{\mu'}{\mu}-1\right)\frac{\gamma}{\Gamma} \end{aligned} \tag{1.44}$$

where the prime stands for inclusion characteristics. Finally, γ and Γ are

$$\gamma = \frac{v_s}{v_p}, \qquad \Gamma = 1+\frac{2}{15}\left(\frac{\mu'}{\mu}-1\right)(3+2\gamma^2) \tag{1.45}$$

The upper limit for the Rayleigh approximation is not exactly known, but Gritto *et al.* (1995) demonstrate that inclusions with relative size of $a/\lambda \leq 17\%$ generally carry an error of less than 5%.

Chapter 2

Method for rapid high-frequency seismogram calculation: the COMRAD code

The calculation of synthetic seismograms has recently become a useful tool in seismological research, and a wide variety of techniques have been developed. Forward modelling, which means in this case the generation of synthetic seismograms, represent an important part of many seismological studies, such as seismic tomography or the kinematic inversion of source parameters (Pengcheng and Archuleta, 2004). The solution of an inverse problem requires the repeated solving of the forward problem, so that speed is the most stringent condition that the method must supply.

For horizontally stratified Earth models the complete wave field computation can be performed by using the theory of normal mode (Aki and Richards, 2002; Rosenbaum, 1960) or the discrete wave number method (Bouchon and Aki, 1977). Methods based on direct numerical solution of the elastodynamic equation by finite difference (Madariaga, 1976; Virieux, 1986), finite elements (Marfurt, 1984), spectral elements (Festa and Vilotte, 2005; Komatitsch and Vilotte, 1998), or discontinuous Galerkin method (Kaser and Dumbser, 2006) can be applied to study the seismic wave field in complex laterally varying structure.

As an alternative it is possible to obtain the solution to the wave equation by using approximate high-frequency methods (Červený, 2001). The solution of the elastodynamic equation is composed of elementary body waves that correspond to the various rays connecting the source to the receiver.

2.1 Aim of a multiphase dynamic ray-tracing code

Although the computation of ray synthetic seismograms is only approximate and the ray method can fail in certain situations, the high-frequency methods are preferable to direct numerical methods for many applications, both for the shorter computing times and for the full interpretability of the seismograms. The problems arise when we want to use

a synthetic seismogram as similar to the real one as possible in the high-frequency approximation, such that the seismogram should be relatively complete, although it is not necessary that it contains every feature of the full elastic wave field. It is becoming necessary to select from all of the rays connecting the source to the receiver only those that produce appreciable amplitude on the seismogram. The problem of generating a comprehensive set of rays was approached for the first time by Hron (1971, 1972; Hron *et al.*, 1986) for layered media, by grouping individual rays into families of kinematic equivalents. Afterwards, Clarke (1993aa, 1993bb) developed a technique for computing synthetic seismograms based on a ray-generation algorithm that involved the symbolic manipulation of complete wavefield expressions from reflectivity theory, which were truncated to produce a finite ray series.

Here we propose a new technique for the rapid definition of an exhaustive set of rays that is based on the hierarchic generation of strings that describe the ray paths and the phase types. The string generation is subjected to physical constraints that are related to the propagation medium and the source-receiver geometry. The ray sets will represent the input of a kinematic or dynamic ray-tracing algorithm (i.e. Červený and Hron, 1980; Farra and Madariaga, 1987; Snieder and Spencer, 1993; Virieux, 1991). In particular, the technique developed has been implemented in the multiphase dynamic ray-tracing COMRAD code (from the Italian: "COdice Multifase per il RAy-tracing Dinamico") that uses as its core the dynamic ray-tracing code provided by Farra and Madariaga (1987).

2.2 Method description

Our goal is to carry out an algorithm that rapidly generates an exhaustive number of seismic-phases to calculate a high frequency seismogram as complete as possible. In particular, the computing time is a critical parameter when the computation of synthetic seismograms has to be repeated many times in the inversion processes. The amplitudes, the raypaths and the travel times of the seismic-phases are computed by the dynamic ray-tracing code provided by Farra and Madariaga (1987). In this section we describe our method and the discretization of the propagation model.

2.2.1 General concepts

It is possible to use an arbitrary medium as long as it is discretized by M ordered elements between a free surface and a halfspace. The sequential elements are separated by a surface. Each element can have an arbitrary shape and is characterized by the following properties:

- Vp_i: compressive wave velocity (P wave);
- Vs_i: shear wave velocity (S wave);
- ρ_i: density;
- Qp_i: P-wave quality factor (optional);

- Qs_i: S-wave quality factor (optional);
- T_i: top surface of the element;
- B_i: bottom surface of the element ($= T_{i+1}$: top surface of the next element);
- $i = 1, \ldots, M$: index of the element.

where the elastic wave velocities, densities and quality factors are functions of spatial coordinates.

Both the source and the receivers take the index i of the element in which they are included. Each ray goes from the source to the receiver and is divided into L curves if it passes through L elements. Each ray is described by a numerical string composed of L numbers, and each one is the index of the element crossed by the ray. For a ray there are also 2^L phase numerical strings, because in each element crossed by the ray the wave can have two different polarizations (P wave or S wave). A numerical string for a phase is composed of L numbers and each one can be 1 (to indicate a P wave) or 2 (to indicate an S wave).

As example, for a medium where the elements are three horizontal, parallel layers, the source is inside the third layer, and the receiver is inside the first layer, the ray string relative to the direct wave is 3-2-1 at which correspond 2^3 phase strings.

Although the algorithm can generate only body waves, it is possible to calculate headwaves travel times using an artifact. We can consider a tiny element between two elements, with the same properties of the second one, and generate a ray string relative to a wave that propagates inside the tiny element. The travel time obtained for that wave is about equal to that for a headwave, but the amplitude is not correct.

2.2.2 Selection Criteria

Once the length L of the numerical ray string is fixed, there are M^L ray strings of the same length if the medium is discretized by M elements. However, not all of the ray strings describe a real ray, because there are some existence constraints for a ray path:

(a) The ray starts at the source;
(b) The ray arrives at the receiver;
(c) The ray path is bordered by the free surface and the half space;
(d) If a ray points towards the top surface of the ith element, it can remain in the same element (with opposite direction) or go to the $(i-1)^{th}$ element (with the same direction);
(e) If a ray points towards the bottom surface of the ith element, it can remain in the same element (with opposite direction) or go to the $(i+1)^{th}$ element (with the same direction);
(f) If the receiver is on the free surface, the ray must come from below;
(g) If the source is on the free surface, the starting direction of each ray cannot be up.

To generate only the ray strings that describe real ray paths, we use a hierarchic order of ray generation, where the root (first generation) is the index of the element that contains the source, and the number of the generations is the length of the numerical strings of the rays. The hierarchic order of ray generation satisfies itself for the (a), (b), and (c) constraints. Indicating with S the source index and with R the receiver index, the generation that produce the ray string of minimum length, that is the direct ray, is given by the number $Lmin = |S - R| + 1$. An example of hierarchic ray generation taken to the fourth generation for a source in the third element ($S = 3$) and a receiver in the first element ($R = 1$), where the medium is discretized by $M = 5$ elements, is shown in Figure 2.1. In this Figure, the last component of the strings that satisfy for each generation the (b) constraint is evidenced with a grey circle. The selected string will be composed by all the numbers in the tree structure from the root to the evidenced number. In this case we have, on the whole, four ray strings (3-2-1, 3-2-1-1, 3-3-2-1, and 3-2-2-1) up to the fourth generation that satisfy the (a), (b), and (c) constraints.

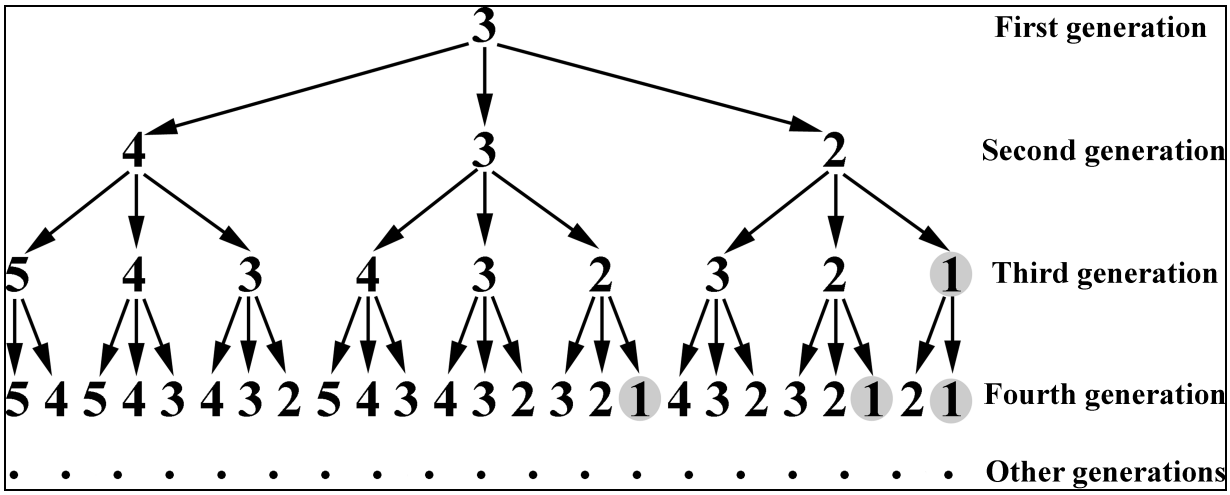

Figure 2.1: *Tree structure of ray strings stopped to the fourth generation. The root, that is the source position, is the number three. The grey circles identify, for each generation, the last component of the strings that satisfy the (b) selection criterion. We have four ray strings up to the fourth generation.*

Using the additional (d), (e), (f), and (g) constraints, we discard some branches inside the numerical string tree. In particular, putting the receiver on the free surface the ray strings selected are shown in Figure 2.2. Now we have only two ray strings (3-2-1 and 3-3-2-1) up to the fourth generation. If we put the receiver inside the first element instead of on the free surface, we will have the additional ray string 3-2-1-1 because there is no (f) constraint yet, and consequently the ray can arrive at the receiver also from above.

Since the number of phase strings becomes greater and greater if the number of generations increases, and consequently the computing time rises, it is possible to introduce some constraints on the propagation in order to reduce the number of phases. For this

reason, we created the following additional constraints on ray-paths and on phases:

(I) Maximum number of generations that means the truncation of ray-series;
(II) Maximum number of reflections in each element;
(III) Phase selection based on their expected amplitude values.

In agreement with ray-theory there are infinite rays that propagate form the source

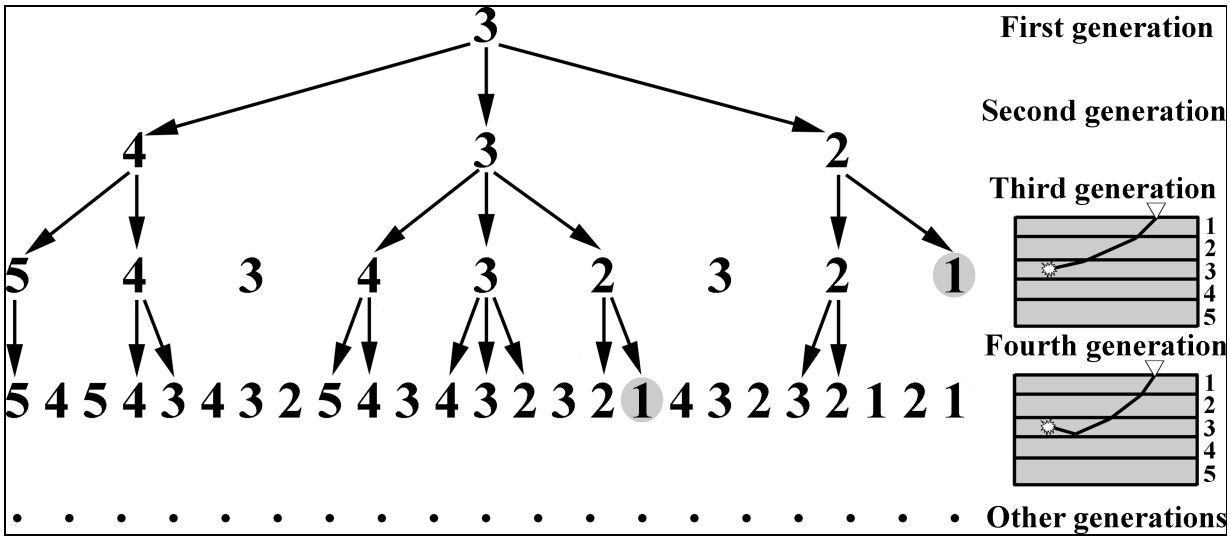

Figure 2.2: *Tree structure of ray strings stopped to the fourth generation as in Figure 2.1, but using all of the (a) to (g) constraints. There are only two ray strings up to the fourth generation because the receiver is on the free surface. If the receiver is inside the first element, there will also be the string 3-2-1-1. The ray-paths relative to the two selected ray strings in the layered velocity model are shown on the right. The white star is for the source and the white triangle is for the receiver.*

to the receiver, but there is also a loss of the initial ray energy whenever it has a reflection/transmission on a discontinuity, besides the energy lost for geometric and anelastic attenuation. After a certain number of generations, the ray strings represent those rays that have encountered so many discontinuities as to have a negligible energy. For this reason it is possible to truncate the ray series at a certain generation without significant loss in energy; this is the principle on which is founded the (I) constraint. In particular the default maximum number of generation is fixed by the number

$$Lmax = Lmin + 2 \cdot M \tag{2.1}$$

which guarantees a complete investigation of the propagation medium.

The (II) constraint assumes that a ray trapped inside an element has a loss in energy bigger than the energy lost by untrapped rays, especially for deeper elements. Using the

(II) constraint, a ray string will be accepted only if is satisfies the condition:

$$(n-1)\cdot i \leq RIFM \tag{2.2}$$

with n the number of consecutive multiple reflection of the ray inside the i^{th} element, i the element index, and $RIFM$ a number that controls the multiple reflections (the default value is $RIFM = 8$). Using the $RIFM$ default value we can have maximum 9 consecutive reflections in the first element (the shallowest), 5 consecutive reflections in the second, 3 in the third and the fourth, 2 from the 5^{th} to the 8^{th}, and only one for the others. The (III) constraint is developed following this scheme:

- For each k^{th} component of the phase string a weight w_k, from 0 to 1, is assigned;
- Once the weight is assigned, the phase string will be accepted only if it satisfies the condition:

$$\prod_{k=1}^{L} w_k \geq PHS \tag{2.3}$$

  where L is the length of the phase string and PHS is a number that represents a percentage of the weights product assigned to the direct P-wave (the default percentage is $1 \cdot 10^{-4}$ %).

Here we describe how the weights w_k have been calculated. For each incident phase (P or S) on the boundary between two elements, we have to calculate each time the scattering coefficient relative to one of the 8 phases that can be generated for reflection/transmission/conversion (PrP, PrS, PtP, PtS, SrP, SrS, StP, StS; where "r" indicates the reflection and "t" the transmission). These coefficients are functions of the incidence angle and the physical parameters (P-wave velocity, S-wave velocity, and density) of the elements crossed by the wave. Their calculation requires both computing time and the values of the incidence angles, but the latter are known only after ray-tracing. To overcome the problem, the weights w_k are defined for each type of interface and for each type of phase independently on the incidence angle. Indeed, to define the weights, we have calculated, for each one of the 8 scattering coefficients, the integral on the whole interval of the incidence angle, dividing the result for the same interval. The values obtained for the four phases that an incident wave can generate (PrP, PrS, PtP, PtS for a P-wave; SrP, SrS, StP, StS for a S-wave) are normalized such that their sum is equal to one. This computation is carried out varying the interface parameters, that is the values of the P-wave velocities, S-wave velocities, and densities of the elements separated by the discontinuity (Table 2.1).

Precisely, S-wave velocities have been determined from P-wave velocities using different values of the Vp/Vs ratio, while densities have been calculated using the following empirical formula of Ludwig *et al.* (1970):

$$\rho = 0.7 + 2.23v - 0.598v^2 + 0.0704v^3 - 0.00283v^4 \tag{2.4}$$

with ρ the density in g/cm^3 and v the P-wave velocity in km/s. The results show that for an incident P-wave the value of the integral, defined previously, depends essentially on

the Vp_1/Vp_2 ratio[1]. Likewise for an incident S-wave the integral depends on the Vs_1/Vs_2 ratio. In fact, as showed in Figure 2.3 and 2.4, the curves relative to the different cases reported in Table 2.1 have a similar shape for each type of phase (i.e. PtP, PrP, etc...).

Velocity model	**Vp_1 (km/s)**	**Vp_1/Vs_1**	**Vp_2 (km/s)**	**Vp_2/Vs_2**
A	2.50	1.73	1.8-7.0	1.73
B	7.00	1.73	1.8-7.0	1.73
C	3.40	1.73	1.8-7.0	3.50
D	4.00	3.50	1.8-7.0	1.73
E	4.00	2.00	1-8-7.0	2.00

Table 2.1: *Different velocity models to study the effect of the boundary between a half-space that contains the incident wave (labelled by the number 1) and a half-space that contains the transmitted wave (labelled by the number 2).*

To avoid the construction of an indexed table for each phase and for each value of Vp_1/Vp_2 and Vs_1/Vs_2 we have selected only 5 intervals of these ratios. The weight assigned to each phase will correspond to the maximum of the corresponding integral curve inside each region. This allows the realization of a smaller indexed table (Table 2.2) which contains the weights to assign to the components of the phase strings. Moreover, the weight assigned to a component of the phase string is equal to zero if in the i^{th} element the component indicates an S wave and $Vs_i < 0.1$ m/s. From equation (2.3) this implies that the whole phase string is rejected.

Type of phase	**Region I $z < 0.5$**	**Region II $0.5 < z < 0.8$**	**Region III $0.8 < z < 0.95$**	**Region IV $0.95 < z < 1.2$**	**Region V $1.2 < z$**
ptp	0.17	0.45	0.73	1.00	0.71
prp	0.70	0.69	0.37	0.24	0.35
pts	0.21	0.24	0.21	0.25	0.27
prs	0.51	0.35	0.19	0.12	0.21
sts	0.50	0.92	0.98	1.00	0.96
srs	0.90	0.66	0.19	0.10	0.16
stp	0.01	0.02	0.02	0.02	0.17
srp	0.17	0.07	0.03	0.03	0.05

Table 2.2: *Weights assigned for each region, defined by z parameter, and for each type of phase. The z parameter is equal to the Vp_1/Vp_2 ratio for an incident P-wave or equal to the Vs_1/Vs_2 ratio for an incident S-wave.*

[1]The indexes 1 and 2 in the velocities ratio indicate the medium that contains the incident wave and the medium that contains the transmitted wave, respectively.

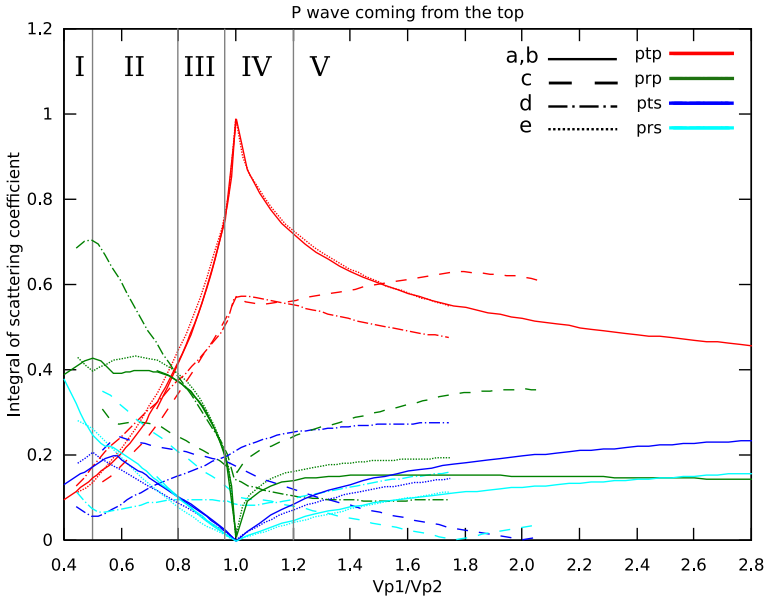

Figure 2.3: *Integral of scattering coefficients for an incident P-wave, as a function of the Vp_1/Vp_2 ratio between the P-wave velocity in the medium 1 (that contains the incident wave) and P-wave velocity in the medium 2 (that contains the transmitted wave). The colour of curves refers to different type of phases, while the style is relative to different velocity models reported in Table 2.1. The five regions I, II, III, IV, V, separated by vertical lines, are defined in Table 2.2.*

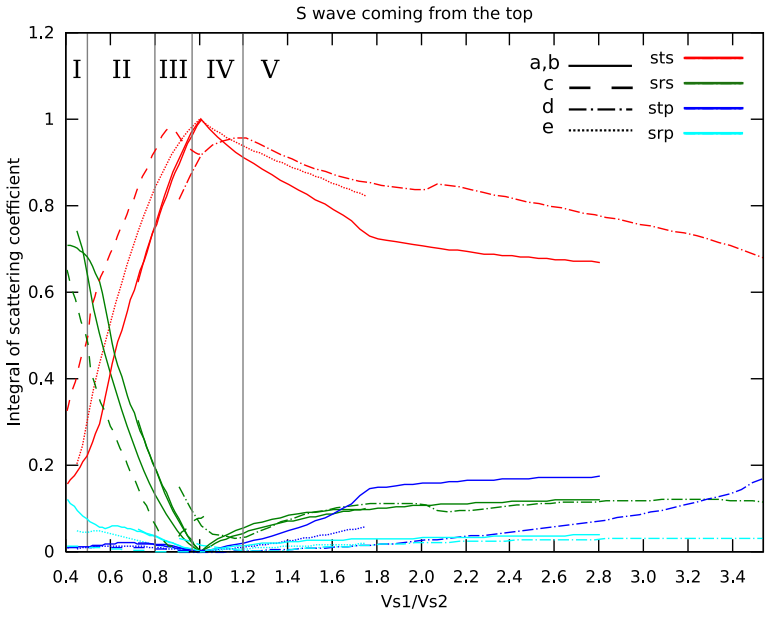

Figure 2.4: *As for Figure 2.3 but referring to an incident S-wave as a function of the Vs_1/Vs_2 ratio between the S-wave velocity in the medium 1 and S-wave velocity in the medium 2.*

2.2.3 Structure of the COMRAD code

The `Comrad.f` code is the Fortran77 version of multiphase code that, based on selection criteria, generates an exhaustive set of ray and phase strings allowing the computation of a seismogram as complete as possible. In order to compute synthetic seismograms, that is travel times, amplitudes, and ray paths relative to the selected phases, it uses as its core the dynamic ray-tracing code developed by Farra (Farra and Madariaga, 1987) which needs a medium discretized by flat tilted layers. However, the COMRAD code can be easily implemented with other dynamic ray-tracing programmes which can work on 3-D models with irregular discontinuities. The code is accompanied by the bash script multiphase.sh, which optimizes the whole calculation process and runs both the COMRAD and core programmes.

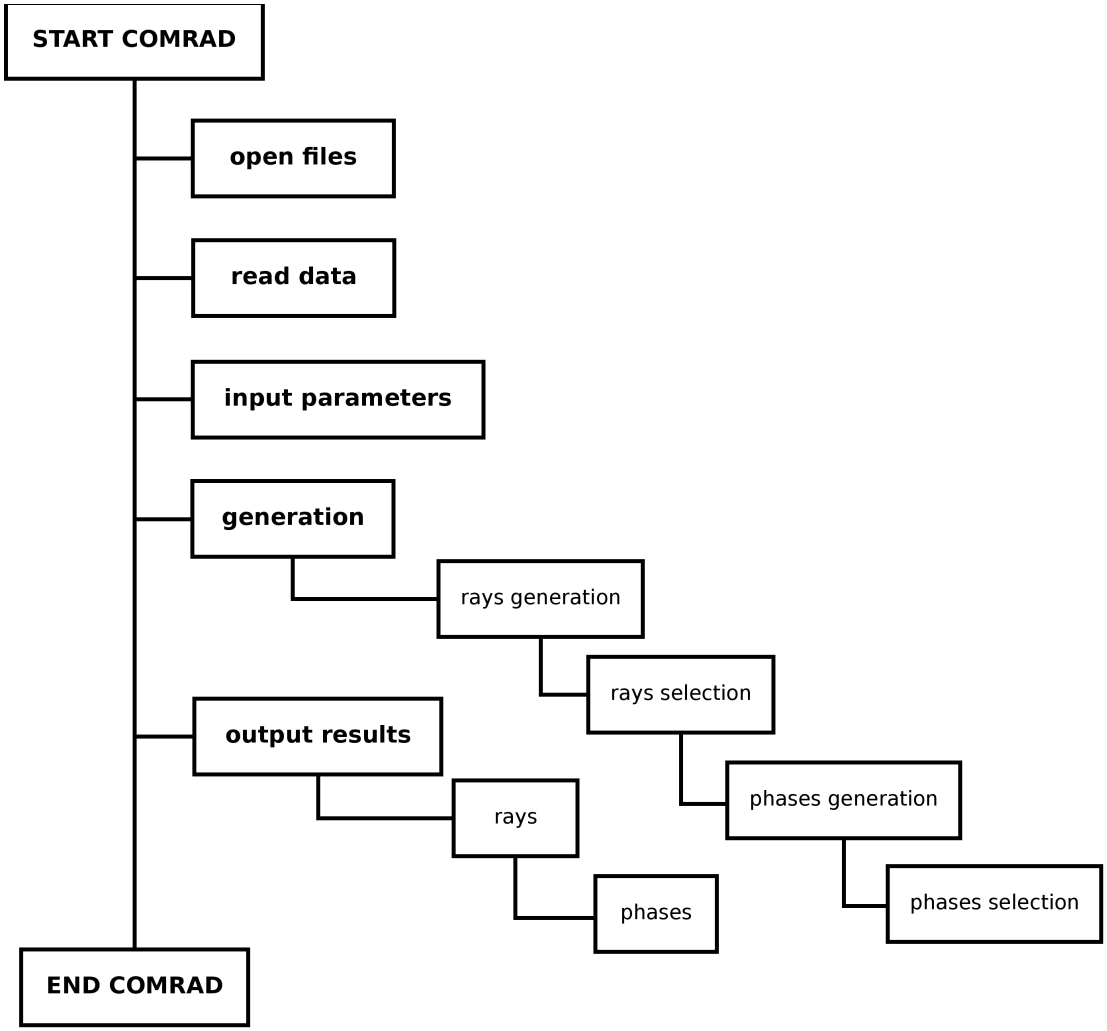

Figure 2.5: *Block scheme of the Comrad.f computer code.*

The structure of the code is shown in Figure 2.5, where we outline its most important features. The code requires the following input data:

- the `creation.inp` file which contains the medium information;
- the `xxxx.dis` file (where `xxxx` represents a four characters word) which contains the source-receiver geometry;
- the maximum number of generations ($Lmax$), which truncates the ray series. The user can choose to use the default value ($Lmax = Lmin + 2 \cdot m$);
- the multiple reflections parameter ($RIFM$), which allows the ray to have a finite number of reflections in each element. The user can choose to use the default value ($RIFM = 8$);
- the phase selection parameter (PHS), which discards phases with negligible amplitudes. The user can choose to use the default value (calculated on the approximated amplitude value of the direct P wave and fixed at $1 \cdot 10^{-4}$ % of this value);
- the initial polarization of the phases (P or S).

Using the hierarchical generation method with the constraints described previously, the code generates the ray and phase strings and creates the following output data:

- the `kernel.inp` file which contains the input parameters for the core;
- the two `xxx1.dis` and `xxx2.dis` files (where xxx represents a three character word) inside which the `Comrad.f` code will write all of the ray and phase strings to be used by the core programme for the computation of the synthetics. The first file describes rays where their starting direction is up, and the second, where it is down. These two files are very important also to search the type of phase identified on the output seismograms, since they contains the list of the ray and phase strings.

The existence of the two `xxx1.dis` and `xxx2.dis` files assures the calculations of both the P/P\ (where S/ or P/ indicates an upcoming S or P wave and S\ or P\ a downgoing S or P wave, respectively) and P\P/ phases (and similar), although they are described by the same ray and phase strings if the source and the receiver are both in the same element (i.e. the ray string is 1-1 both for P/P\ and P\P/ phases if the source and the receiver are in the first element of the medium). Moreover, if the source is on the free surface, the `xxx1.dis` does not exist because of the (g) constraint.

In order to select the appropriate weight for each type of phase we have transformed the Table 2.3 in a 3D-matrix of indexes Z, RT, and POL. The RT index indicates if there is a reflection or a transmission; it is equal to 1 for a transmission and 2 for a reflection. The POL index indicates the polarization of the phase before and after a reflection/transmission; it is equal to 1 for PP, 2 for PS, 3 for SP and 4 for SS. Z indicates the number of the region (see Figures 2.3 and 2.4) containing the Vp_1/Vp_2 ratio

(for an incident P-wave) or Vs_1/Vs_2 ratio (for an incident S-wave) values. To avoid the introduction in the `comrad.f` program a great number of control instructions to verify the index values, we have searched two relations (equation (2.5) and (2.6)) that directly determine the values of the RT and POL indexes. The value of the RT index is obtained from the equation (2.5):

$$RT = \mid ud1 - ud2 \mid +1 \tag{2.5}$$

where $ud1$ and $ud2$ are the directions (1 for up and 2 for down) of the i^{th} component and the $(i+1)^{th}$ component of the ray string, respectively. The value of the POL index is obtained instead from the equation (2.6):

$$POL = 2a + b - 2 \tag{2.6}$$

where a and b are the polarizations (1 for a P-wave and 2 for a S-wave) of the i^{th} component and the $(i+1)^{th}$ component of the phase string, respectively.

After the COMRAD and core programmes have finished, the output consists of files containing the Green function[2] and a list of raypaths, travel times and amplitudes for all the phases. If more than one receiver is considered it is possible to produce a synthetic section for each component (X, Y, and Z).

2.3 Validation of the method

The higher the number of generations we consider, the higher the number of phases the core must calculate. To make the best choice on the number of generations, we have to compare the calculation time with the complexity we need for the synthetics.

Several tests have been carried out both to set the default parameters and to understand the limits beyond which the method should fail. We have computed synthetics for different velocity models and compared qualitatively and quantitatively the results with those obtained using complete wavefield programs. In particular, here we will describe in details one of these validation tests.

We compute synthetic seismograms for two receivers (R_1 and R_2) respectively at 1 km and 30 km distance from the epicentre of an explosive source. The source function is a triangle with duration of 0.1 s, but it is possible to choose other source functions (i.e. Sinusoidal, Gaussian, Ricker, ...) and change the duration and the frequency. We use a crustal velocity model Bernard and Zollo (1989), where the elements are considered in this case as horizontal parallel layers. The model is described in Table 2.3, while the results of the simulations are given in Table 2.4. Only the geometrical spreading is considered in the computation of synthetics and no headwaves are considered since we can compute only their travel times and not the amplitudes.

The source depth is 4 km, and both of the receivers are at 1 m in depth. For this source-receiver geometry, the source is in the second layer, the receivers are in the first layer and

[2]The Green function is the displacement due to a unidirectional unit impulse, which is localized precisely in both space and time.

Interfaces	**Depth (km)**	**Vp (km/s)**	**Vs (km/s)**	ρ **(g/cm^3)**
1	0	2.30	1.33	2.2
2	3	5.30	3.06	2.3
3	7	6.00	3.46	2.4
4	10	6.28	3.63	2.6
5	20	6.54	3.78	2.8

Table 2.3: *The crustal velocity model used for the simulations.*

the first real phases start at the second generation. In Table 2.4, for each generation, the time needed by both the COMRAD and core programmes for the calculations can be seen, along with the total number of phases and the RMS calculated for both of the receivers and for both of the X and Z components of the seismogram. The RMS is a measure of the similarity between two signals and in the Table 2.4 it is calculated between the synthetic seismogram obtained at each generation ($S(t)$) and that obtained for the previous generation ($SREF(t)$). The RMS is defined as follows:

$$RMS = \sqrt{\frac{\sum_t \mid S(t) - S_{REF}(t) \mid^2}{\sum_t \mid S_{REF}(t) \mid^2}} \tag{2.7}$$

where t is the time. The amplitudes of the seismograms are normalized with respect to their maximum amplitudes. The calculations are carried out using a PC with an AMD-3GHz processor and 2Mb SD-RAM memory.

N. of GEN.	COMRAD TIME	CORE TIME	N. of PHASES	RMS R_1-CompX	RMS R_1-CompZ	RMS R_2-CompX	RMS R_2-CompZ
2	0m 00.05s	0m 00.06s	2	-	-	-	-
3	0m 00.05s	0m 00.15s	10	1.037	0.992	4.628	4.789
4	0m 00.05s	0m 00.29s	34	0.108	0.104	0.980	0.932
5	0m 00.05s	0m 01.13s	114	0.107	0.103	0.262	0.340
6	0m 00.05s	0m 04.42s	370	0.027	0.144	0.440	0.494
7	0m 00.05s	0m 16.84s	1266	0.026	0.028	0.398	0.399
8	0m 00.05s	1m 07.45s	4210	0.008	0.010	0.186	0.252
9	0m 00.11s	4m 18.82s	14706	0.008	0.010	0.131	0.220
10	0m 00.27s	16m 18.15s	49522	0.002	0.004	0.087	0.109
11	0m 01.18s	1h 00m 23.47s	174450	0.002	0.004	0.077	0.092
12	0m 03.39s	3h 40m 56.38s	590194	0.001	0.002	0.037	0.058

Table 2.4: *Computing time of COMRAD and core codes, number of phases, and RMS computed at each generation for both of the receivers R_1 and R_2, at 1 km and 30 km distance from the source, respectively. The horizontal (CompX) and vertical (CompZ) components of the seismograms are considered.*

We show the results up to the 12^{th} generation since the RMS becomes negligible at the expense of an excessive computing time. From Table 2.4, it is clear that the RMS is lower

and lower as a function of the number of generations. Moreover, starting from the RMS calculated between the 9^{th} and 10^{th} generations, the RMS decrease rate at 30 km distance becomes stable for both the X and Z components. This means that if we truncate the ray series at the 10^{th} generation we obtain little values both for the RMS and the computing time.

If we take into account also the propagation constraints it is possible to reduce further the number of phases created at each generation. The selection on the phase strings is controlled by the $RIFM$ and the PHS parameters discussed in the previous paragraph. In order to evaluate the changes on the seismogram due to the application of these constraints, we calculate the RMS, the computing time, and the number of phases for different values of $RIFM$ and PHS parameters. In particular we used $RIFM = \infty$, when the constraint is not used, and the default value $RIFM = 8$. The test is performed on the seismogram obtained at the 10^{th} generation for both receivers R_1 and R_2 of the previous model. The RMS is computed using as reference signal both the same seismogram but complete with all phases and the seismogram computed at the 12^{th} generation complete with all phases. As we can see in the Table 2.5 the use of the $RIFM$ parameter can reduce the number of phases (and then the computing time) from 2% to 20%, but this reduction depends on the choice of the PHS value (it is bigger for lower PHS values). On the other hand PHS is a crucial parameter able to reduce considerably the number of phases without losing the phases with bigger amplitude. If we choose for PHS a value equal to 1.4% of the relative direct P-wave value, the computing time is drastically reduced (from 16m 18.15s to 1.77s) whereas the RMS becomes significant for the receiver more distant (R_2). The best values for $RIFM$ and PHS parameter can be chosen on the basis of the required precision.

PHS (%)	RIFM	COMRAD TIME	N. of PHASES	RMS-10^{th} R_1-CompZ	RMS-10^{th} R_2-CompZ	RMS-12^{th} R_1-CompZ	RMS-12^{th} R_2-CompZ
0	∞	16m18.42s	49522	0.000	0.000	0.005	0.109
$1.4{\cdot}10^{-4}$	∞	8m 52.96s	29300	0.000	0.035	0.005	0.116
$1.4{\cdot}10^{-4}$	8	8m 18.91s	24218	0.000	0.035	0.005	0.116
$1.4{\cdot}10^{-2}$	∞	1m 25.20s	4648	0.000	0.298	0.005	0.319
$1.4{\cdot}10^{-2}$	8	1m 18.31s	4195	0.000	0.298	0.005	0.319
1.4	∞	0m 01.99s	137	0.015	0.694	0.017	0.703
1.4	8	0m 01.77s	134	0.015	0.694	0.017	0.703

Table 2.5: *Computing time of COMRAD(+core) code, number of phases, and RMS computed at each generation for both of the receivers R_1 and R_2, at 1 km and 30 km distance from the source, respectively. The vertical component (CompZ) of the seismogram is considered. RMS-10^{th} is the RMS relative to the seismogram computed at the 10^{th} generation without constraints. RMS-12^{th} is the RMS relative to the seismogram computed at the 12^{th} generation without constraints.*

To better understand if our choice is appropriate, we can calculate the complete wavefield for the case under study by the AXITRA programme, which uses the discrete wavenumber method developed by Bouchon (Bouchon, 1981; Coutant, 1989). Afterwards, we can compare the AXITRA results with those obtained using the COMRAD programme

stopped at the 10^{th} generation, where the amplitudes of the synthetics are expressed in velocity and are normalized with respect to their maximum amplitude. The AXITRA computation time (up to the frequency of 25 Hz) is 53 minutes and 41.6 seconds, 3-4-fold longer than the COMRAD+core computation time obtained at the 10^{th} generation (see Table 2.5). For a quantitative comparison between the synthetics, we use the misfit criteria in time and frequency that was developed by Kristeková *et al.* (2006). In fact the standard RMS matches the single-valued envelope misfit only in the case of a pure amplitude modification of the signal while in all other cases RMS considerably overestimates the misfits and does not recognize what causes the difference (Kristeková *et al.*, 2006). The time frequency envelope misfit ($TFEM$) is calculated according to the following equation:

$$TFEM(t,f) = \frac{\Delta E(t,f)}{\max_{t,f}(\mid W_{REF}(t,f) \mid)} \tag{2.8}$$

while the time frequency phase misfit is calculated according to equation (2.9):

$$TFPM(t,f) = \frac{\Delta P(t,f)}{\max_{t,f}(\mid W_{REF}(t,f) \mid)} \tag{2.9}$$

where t is the time, f is the frequency, $\Delta E(t,f)$ is the local time-frequency envelope difference, $\Delta P(t,f)$ is the local time-frequency phase difference, and $WREF(t,f)$ is the time-frequency representation of the reference signal $SREF(t)$ based on the continuous wavelet transform. In this case the difference is computed between the COMRAD and AXITRA seismograms.

In Figures 2.6 and 2.7, the $TFEM$ and the $TFPM$ misfits for the vertical component of the seismograms computed at the receivers at 1 km and 30 km distance from the source are shown. Red colour in the $TFEM$ and the $TFPM$ images indicates greater amplitude and a positive phase shift in the COMRAD seismogram respect to AXITRA seismogram. Blue colour represents the opposite case. For the receiver at 1 km distance the $TFEM$ and the $TFPM$ values suggest a good agreement between the synthetics computed using the two methods. In fact the maximum $TFEM$ value, observed at 1.5 s, is about 4% while the maximum $TFPM$ value is about 0.6%.This agreement slowly decreases with the source-receiver distance as shown in Figure 2.7 for the receiver at 30 km distance from the source. In Figure 2.7 we can see that there is a maximum envelope misfit, of about 20%, in correspondence of 7.5 s and 11 s. These misfits are due to differences in amplitude between the two seismograms, as evidenced in the plots of the synthetics in Figure 2.7. Over 16 s COMRAD seismogram amplitudes are generally underestimated probably for the absence of the surface waves calculated by AXITRA and not by COMRAD code. Moreover, from the $TFPM$ plot in Figure 2.7, the phase misfit is less than 7%. In general, the differences in amplitude and phase between the synthetic seismograms computed by the two codes decrease at higher frequencies as expected by theory. The misfits are shown only for frequencies greater than 3 Hz because the COMRAD code is valid only in the high frequency approximation.

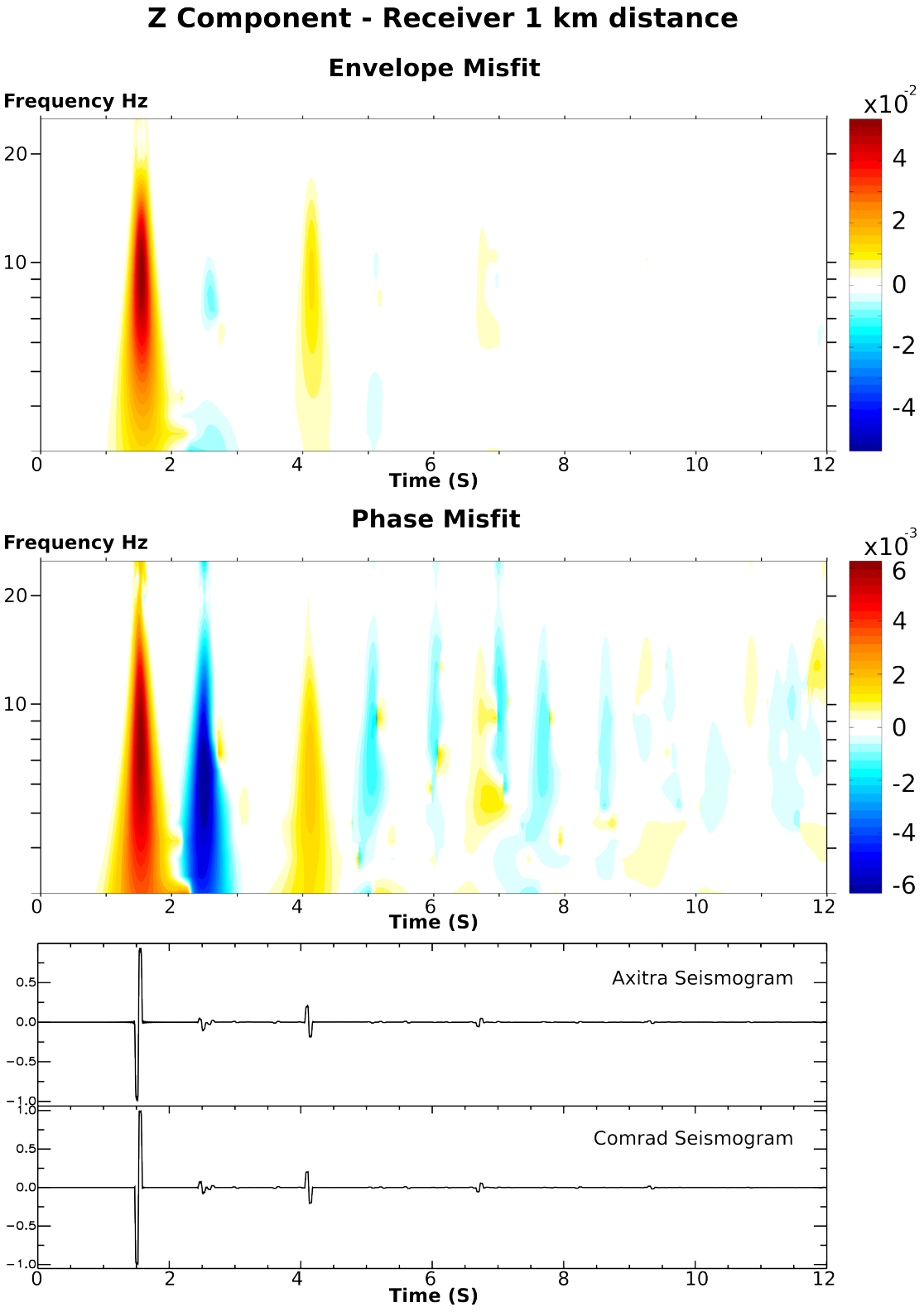

Figure 2.6: *(Top) Time frequency envelope misfit $TFEM(t, f)$ and (Middle) time frequency phase misfit $TFPM(t, f)$ plots for the vertical components of the seismogram computed for a receiver at 1 km distance from the source. (Bottom) The two synthetic seismograms computed by AXITRA and COMRAD codes. The amplitudes are normalized with respect to the maximum amplitude of each seismogram.*

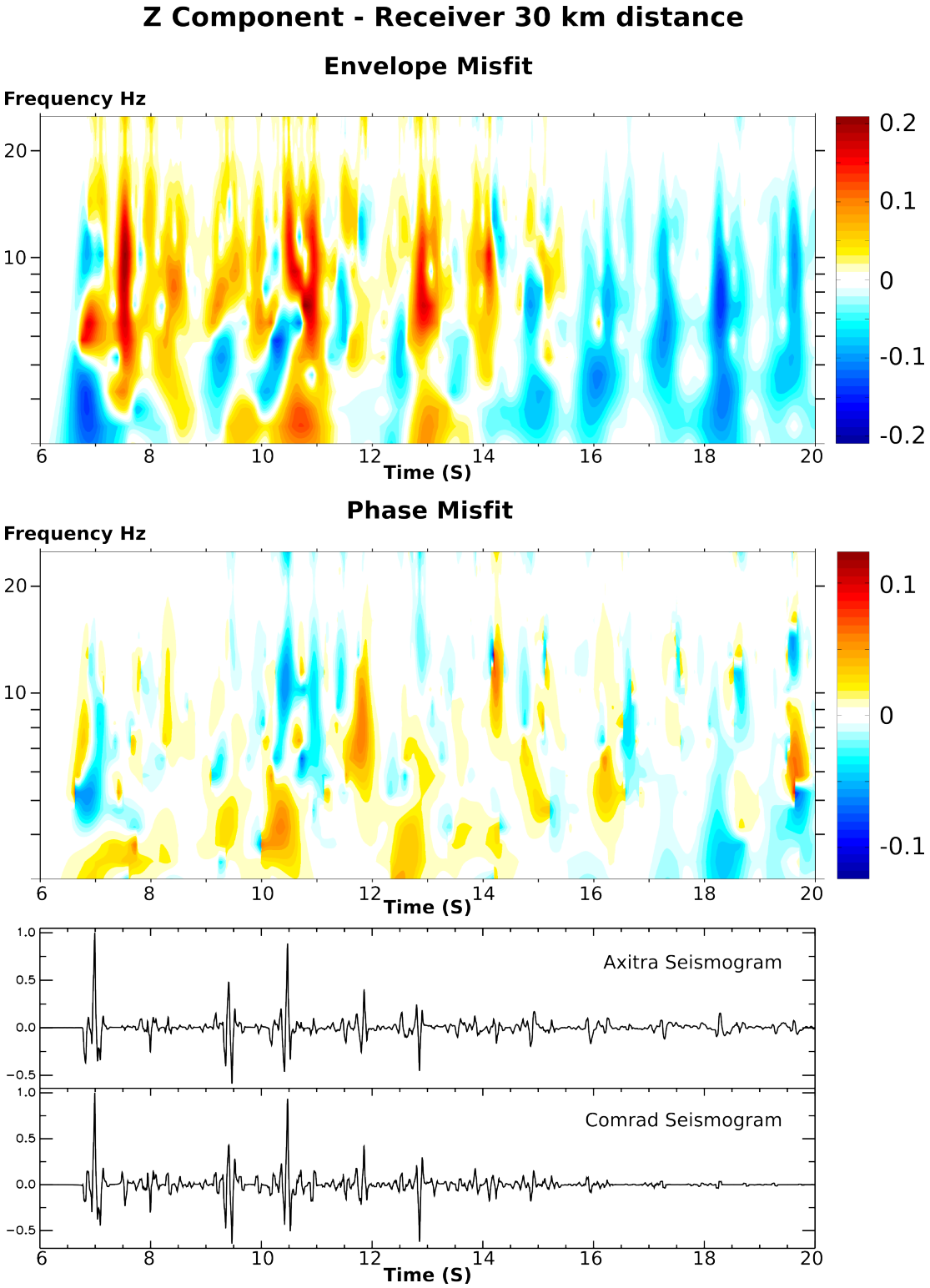

Figure 2.7: *As in Figure 2.6 but referring to the receiver at 30 km distance from the source.*

2.4 Results and discussions

We have developed a method for rapid high frequency seismogram computation based on a hierarchical order of ray and phase strings generation subjected to physical constraints. The method is used in a code (`Comrad.f`) to compute an exhaustive set of phases able to produce a complete body waves seismogram. It uses as core the dynamic ray-tracing code developed by Farra and Madariaga (1987).

We have numerically tested the method in two steps using a PC with an AMD-3GHz processor and 2Mb SD-RAM memory. First we evaluated, generation by generation, both the computing time and the RMS between the COMRAD synthetics obtained in each generation and those obtained in the previous generation. This allowed us to choose the number of generation at which we can truncate the ray series that is the 10th generation.

After fixing the number of generations, we compared the COMRAD-derived synthetic seismograms with AXITRA-derived synthetic seismograms, the latter being a programme that calculates the complete wavefield. The numerical tests were carried out by the quantitative misfit criteria developed by Kristeková *et al.* (2006).

The seismograms computed by the COMRAD and AXITRA programmes are in good agreement at least up to 30 km source-receiver distance. For a receiver 30 km distant from the source, where we have greater misfits, the maximum time frequency envelope misfit is about 20% only in correspondence of 7.5 s and 11 s on seismograms, due to the differences in amplitudes.

Finally, we have compared the computation times for both of the programmes, and we can be sure that COMRAD code (with 10 generations without constraints) is 3-4-fold faster than AXITRA code (up to a frequency of 25 Hz). If we want to compute the synthetics at higher frequencies, the AXITRA code needs more time, while the computation time of the COMRAD code remains the same or decreases if we take into account the additional constraints on the phases. These constraints are based on the maximum number of reflections in each element of the model and on the expected amplitude value for each phase. We have evaluated the effects of these constraints on the seismogram computed at the 10^{th} generation in terms of number of phases, computing time, and accuracy of the signal. The results confirm that the constraints are effective, reducing the number of phases to be computed without losing the phases with appreciable amplitude on the seismogram.

The source code and a user guide of the COMRAD program are reported in Appendix A.

Chapter 3

Applications of the COMRAD code in seismology

In this chapter we will show some applications of the COMRAD code in seismology. In particular in the first section some applications to seismic reflection data recorded during SERAPIS active seismic survey will be described. In the second section synthetic seismograms for an earthquake faulting source will be computed, considering the focal mechanism of the source. In particular, an example of a vertical strike-slip mechanism will be considered. Finally, the extended source case will be planned.

Each section has a conclusive paragraph, where the limits and the potentialities of this code for such problems will be discussed.

3.1 Forward modelling of active seismic data: the case study of Campi Flegrei caldera

Seismic data are used for the seismic exploration of the medium in order to deduce information about the rocks from the observed arrival times and from variations in amplitudes, frequency, phase and wave shape in the recorded seismogram. In particular structural information is derived from headwaves paths (refraction seismic) and reflected paths (reflection seismic). In seismic exploration both passive and active seismic data (Telford *et al.*, 1990) can be used.

When an earthquake occurs, the rocks rupture generates seismic waves that travel outward from the fracture surface. These waves, as they spread throughout the propagation medium, are recorded by seismic instruments, called seismometers, and seismologists use the data to deduce information about the nature of the rocks or the properties of the seismic source. In this case we use the term of passive seismic, where both the position and characteristics of the source are unknown.

Active seismic involves basically the same type of measurements as passive seismic, but the sources are human-made, controlled and movable. Moreover, the distances between the source and the receivers are relatively small.

A useful tool for the seismic exploration is the calculation of synthetic seismograms for a given structure to be compared with the active seismic data recorded for that structure. The comparison can help the operator to understand the goodness of the model produced for the structure under investigation and to the identification of second arrivals of phases in the observed seismograms. The model can be further optimized using step by step procedures based on the comparison between synthetic and real seismograms and the minimization of their differences.

Here we show an application of the COMRAD code to reflection seismic studies on the Campi Flegrei caldera (Figure 3.1). Since the code is based on the ray theory (see Chapter 2), it is very useful whenever headwaves and surface waves are not required to study the medium, as in the case of seismic reflection when the reflected body waves are the most important waves to be considered.

Figure 3.1: *An image of the Campi Flegrei caldera (Campania region, southern Italy). This image was produced using Google Maps tools.*

Campi Flegrei (Figure 3.1) is an active volcano located at the eastern margin of the Tyrrhenian Sea, wherein a large part of the city of Naples is located. Campi Flegrei is a partly submerged caldera and its shape is believed to be a consequence of two huge areal collapses generated by large explosive eruptions occurred in the past. The structure of

the caldera has been investigated previously via several methods and in 2001 an extended active survey was performed in order to study its internal structure. On the following section a brief description of this experiment is shown.

3.1.1 A brief description of Serapis active seismic survey

SERAPIS (SEismic Reflection/Refraction Acquisition Project for Imaging complex volcanic Structures) is the acronym of an extended active survey performed during September 2001, in the gulfs of Naples and Pozzuoli (Zollo *et al.*, 2003) with the aim to provide new insights on the Campi Flegrei caldera, Southern Italy, and to investigate its feeding system. During the SERAPIS experiment, seismic signals produced by a battery of 12, 16-liters air-guns mounted on the oceanographic vessel NADIR (IFREMER) were recorded at a dense array of three-component, sea bottom and on land seismographs installed in the bays of Naples and Pozzuoli.

Seventy-two, three-component stations were installed on-land in the areas of Campi Flegrei, Mt.Vesuvius and on the islands of Ischia and Procida. Sixty, sea bottom seismographs (OBS) were installed in the gulfs of Naples and Pozzuoli. A total number of 5000 shots were fired during the experiment, with an average spacing of 125 m.

Based on the acquisition layout of the experiment, a specific trace gathering scheme, that took advantage of the potential of the 3D source-receiver geometry, was developed and applied to improve the detection and resolution of reflected/converted phases.

The recorded seismic waveforms were arranged in 3D Common Midpoint (CMP) gathers following the procedure described below. The Pozzuoli Bay area was subdivided into square cells and the midpoint position between the corresponding source and receiver was calculated for each trace considered, taking as maximum offset a distance of 9000 m. All of the records with the midpoint falling in a given cell have therefore been grouped into the same CMP, independent of the source-receiver azimuth. This is equivalent to assuming a near vertical variation in the velocity distribution in a cone, pointing down in the Earth at the cell centre, and having a diameter of 9000 m at the surface (Zollo *et al.*, 2003). After several trials, a cell size of 500 x 500 m was chosen based on the criteria of having a sufficiently high number of traces in each CMP gather (> 30) and a dense coverage of the explored area, while maximum offset was chosen based on the duplex criteria that the lateral variations of the velocity had to be negligible with respect to those vertical, and along the sections the morphology of the interface had to be more or less planar and horizontal.

3.1.2 Comparisons between synthetic sections and real sections

Starting from a 3-D tomographic model of Campi Flegrei (Zollo *et al.*, 2003) obtained from data recorded during the SERAPIS experiment, a 1-D average model is derived using also information on physical properties of rocks measured on samples from Agip wells (Rosi and Sbrana, 1987; Giberti *et al.*, 2006).

The 1-D average model has been used to calculate synthetic sections in order to find multiple reflections in the real sections. In Figure 3.2 the 1-D average model and the comparison between a real section with a synthetic section is reported.

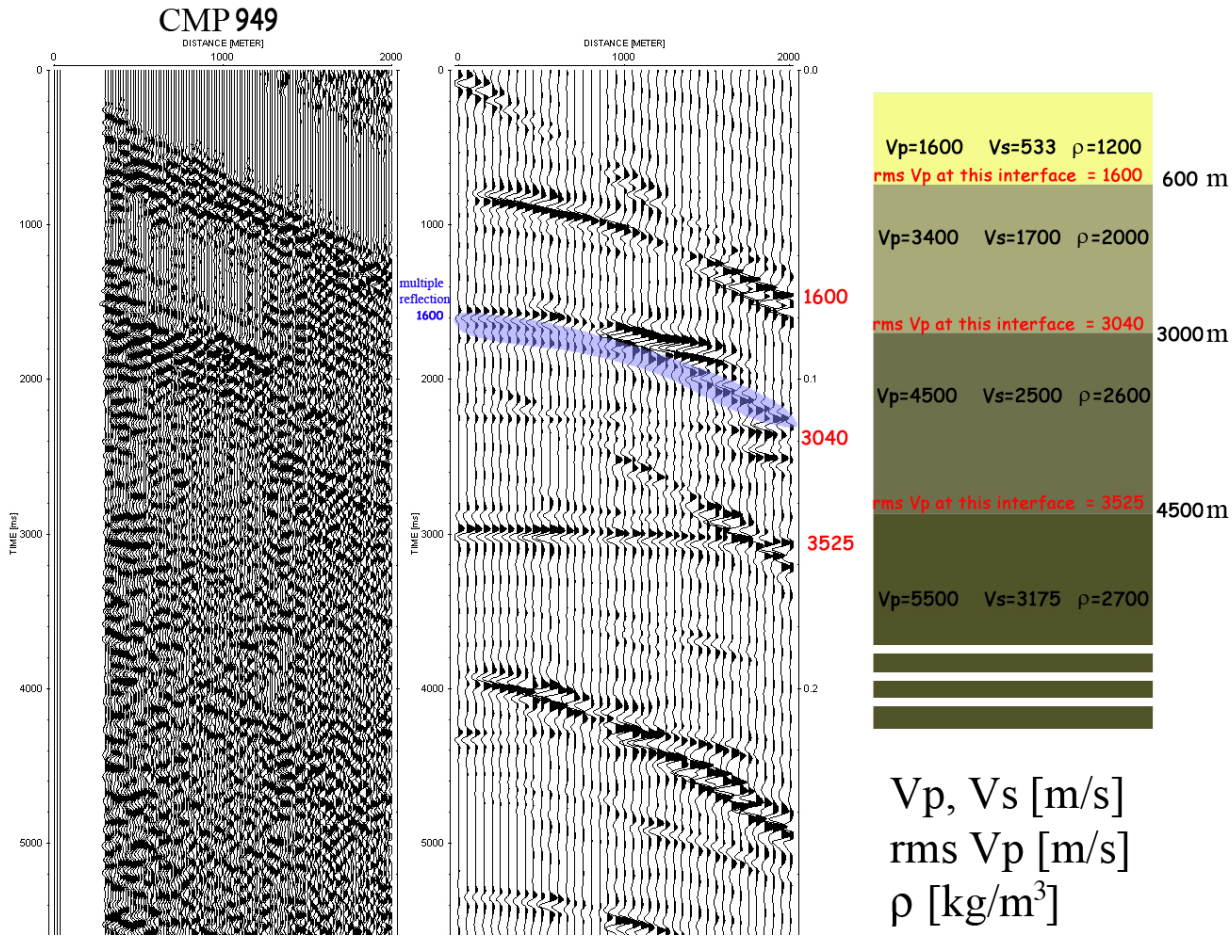

Figure 3.2: *(Right) 1-D average model for Campi Flegrei. (Left) Comparison between a real section of SERAPIS experiment and the relative synthetic section (only vertical component) computed with COMRAD code for the 1-D model reported in the figure. Reflections to the interfaces of the model are indicated, and the multiple reflection to the first interface is evidenced in blue.*

A blue colour evidences in Figure 3.2 the multiple reflection to the first interface at a depth of 600 metres. Moreover, also the P-to-P reflections to the three interfaces of the model with the relative rms velocity[1] are indicated in Figure 3.2.

[1]Considering a medium composed by a number of horizontal layers of different velocities (the velocity is constant within each layer), the travel time t of the reflected wave to the n^{th} interface can be calculated using the root-mean-square (rms) value V_{rms} of its velocity, so that:

$$t^2 = t_0^2 + x^2/V_{rms}^2$$

The COMRAD code up to the 6^{th} generation has been used to compute the vertical component of the synthetic seismogram of Figures 3.2 and 3.3, with the source-receiver geometry equal to the source-receiver geometry of the SERAPIS experiment. In practice, we have considered an explosive source (with a peak frequency of about 10 Hz) at a depth of 10 m and the receivers depth equal to 90 m, while the maximum offset has been fixed at a distance of 2000 meters. The processing has been performed using an automatic gain control with a 0.5 s window, and amplitude normalization for both the real and the synthetic sections. Moreover, an 8-15 Hz band-pass filtering was applied on real sections in order to remove low frequency waves, which are not taken into account by the COMRAD code.

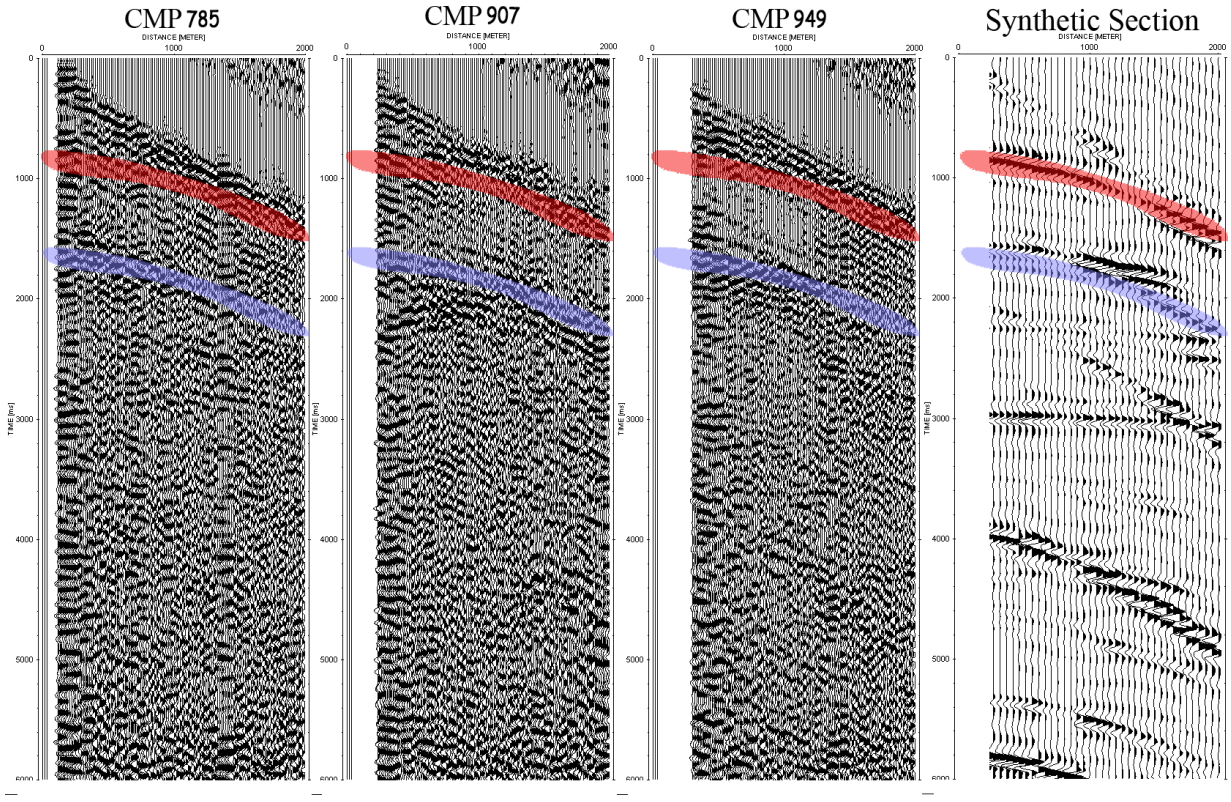

Figure 3.3: *Three different real sections (CMP 785, CMP 907, CMP 949) in which the multiple reflection of Figure 3.2 is clear. The multiple reflection to the interface at 600 m is evidenced with blue colour both on real and synthetic sections (vertical components), while the single reflection to the same interface is evidenced with red colour only on the synthetic section.*

where x is the distance between the source and the receiver (offset), t_0 is the travel time for $x = 0$, and V_{rms} is given by

$$V_{rms} = \sqrt{\frac{\sum_{i=1}^{n} V_i^2 t_i}{\sum_{i=1}^{n} t_i}}$$

V_i and t_i are, respectively, the average velocity in and the traveltime through, the i^{th} layer.

The multiple reflection shown in Figure 3.2 is clear also on other real sections, as reported in Figure 3.3. This confirms that the phase is really a multiple reflection to the first interface of the model and not a reflection to a deeper interface (that can be found at about 1500 meters in depth, according to the travel-time of the phase under investigation).

The COMRAD code has been used also to compute a synthetic seismic section to simulate one of the CMP gathers of SERAPIS survey in order to make quantitative analyses on reflected waves to the interfaces of a 1-D model for Campi Flegrei. For this case we used the average 1-D model for the Campi Flegrei caldera, based on ray kinematic modelling of PP and PS travel times and on PS-to-PP amplitude ratios vs. offset, as obtained by Maercklin and Zollo (2008) from the analysis of real data. The model is shown in Table 3.1.

Interfaces	**Depth (km)**	Vp **(km/s)**	Vp/Vs	ρ **(g/cm^3)**
1	0.0	1.6	3.40	2.2
2	0.6	3.5	1.70	2.6
3	2.7	from 4.7 to 6.0	1.58	2.6
4	4.0	6.0	1.65	2.6
5	7.5	2.8	2.35	2.6
Halfspace	8.7	6.5	$\sqrt{3}$	2.6

Table 3.1: *Average 1-D model for Campi Flegrei (Southern Italy) as derived by Maercklin and Zollo (2008). In the third layer there is a positive gradient velocity with depth, while the* 5^{th} *layer is an area (probably the magma chamber) with low P-velocity and high* Vp/Vs *ratio.*

For these simulations we have reproduced, like the previous case, the acquisition geometry used during the SERAPIS experiment, where the source depth is 10 m and the depth of the receivers is 90 m. We have considered a Gaussian source function with a peak frequency of 11 Hz. Radial and vertical synthetic seismograms have been computed stopping now the hierarchic ray generation to the 11^{th} generation and considering a maximum offset of 4000 m.

The synthetic sections have been compared with the real ones relative to the same CMP. In Figure 3.4 the vertical and radial components for both the synthetic and real seismic sections are shown. Red and green lines indicate the travel time of PP and PS reflection to the 2^{nd} interface of the model, respectively. The gather is formed by 190 recordings. The processing has been performed using 8-15 Hz band-pass filtering, an automatic gain control with a 1 s window (only on synthetic sections), and an amplitude normalization. Although a processing has been performed, it is difficult to see the PP reflection to the 2^{nd} interface on the radial components of the sections. This is normal, since the P-wave is polarized along the direction of the raypath which is near vertical at each receiver due to a high contrast of elastic parameters at the 1^{st} interface of the model (see Table 3.1).

In summary, the qualitative comparison shows that the synthetic sections well reproduce the main seismic phases. This confirms the goodness of the 1-D velocity model used to calculate synthetics.

Once the synthetic sections are calculated for the model of Table 3.1, we can use these sections as real sections to make some analyses in order to estimate the elastic parameter of the model. As an example amplitude variation with offset (AVO) analyses are often used to estimate elastic parameter contrasts at a given reflector.

Maercklin and Zollo (2008) propose a variant of these techniques that evaluates amplitude ratios between PS and PP reflected at the same interface. Here we use the PS-to-PP amplitude ratio variation with offset to check the amplitudes of the COMRAD synthetics.

In Figure 3.5 we show a comparison between the amplitude ratios measured from the synthetic seismograms (green dots) and the theoretical curve (grey line) for the corresponding interface at 2.7 km depth (see Table 3.1). Blue and red lines are theoretical curves for alternative models with higher and lower P-velocity in the layer below the reflector, respectively (2% interval).

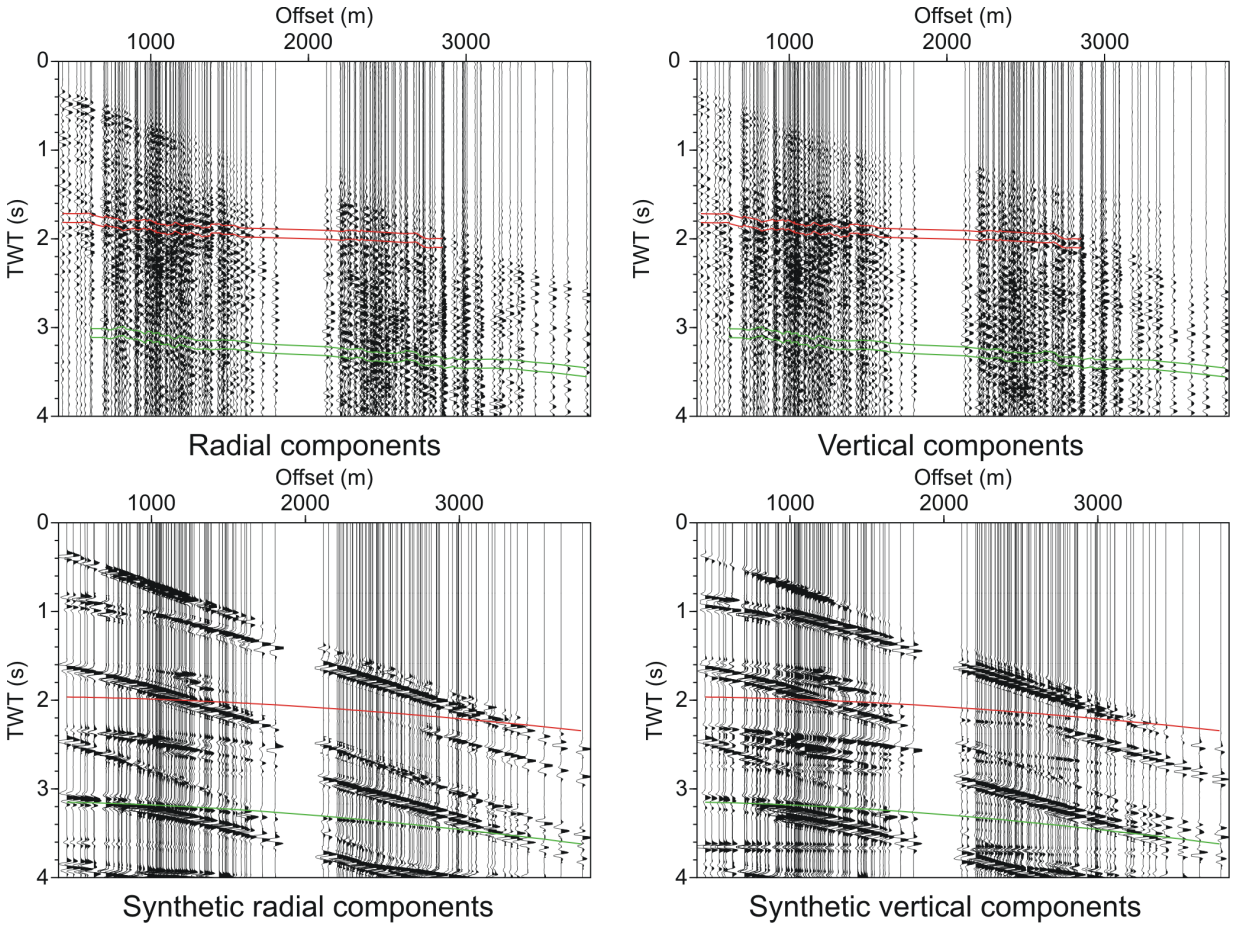

Figure 3.4: *Comparison between the observed (top) and synthetic (bottom) sections for the average 1-D model of Table 3.1. Both radial component (left) and vertical component (right) are reported. Red and green lines indicate the travel time of PP and PS reflection to the 2nd interface of the model, respectively.*

Generally, the measured amplitude ratios are consistent with the theoretical curves up to an offset of about 3 km. The scatter around the expected curve can be explained by the contamination with other phases, mainly multiples from the strong reflector above the target reflector. Around the second minimum of the theoretical curves (offsets greater than 3 km), the measured ratios are better fit using a model with a higher P-velocity contrast at the reflector (blue lines), and the rapid amplitude increase toward 4 km offset has not been reproduced. Since the second minimum of the PS-to-PP curve indicates the distance of critical reflection, the observed amplitude discrepancy may be related to inaccurate post-critical amplitudes in the synthetic seismograms.

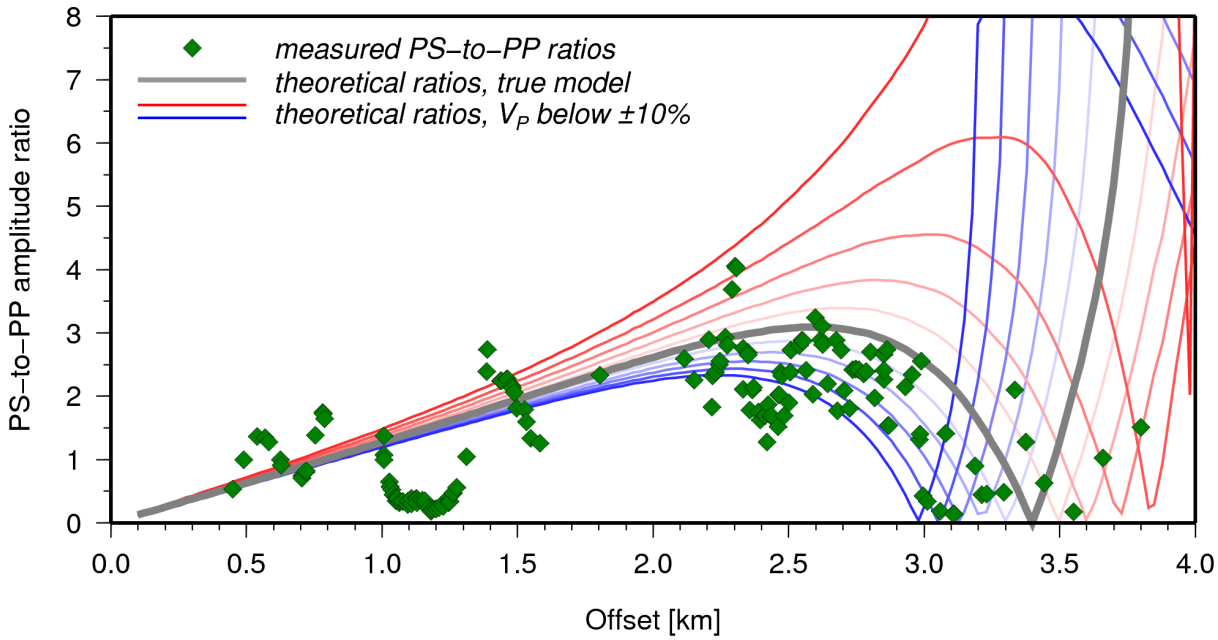

Figure 3.5: *AVO analysis (PS-to-PP ratio) to the second interface of the velocity model. Blue and red lines are theoretical curves for alternative models with higher and lower P-velocity in the layer below the reflector, respectively.*

3.1.3 Conclusions and discussions

In this section, applications of the COMRAD code to seismic reflection data illustrate how such a method can be a useful tool for the waveform analysis. We compute a synthetic section reproducing the acquisition geometry of SERAPIS survey and considering first the 1-D model of Campi Flegrei plotted in Figure 3.2 and after the 1-D obtained by Maercklin and Zollo (2008), reported in Table 3.1.

In the first case qualitative comparisons between synthetic and real seismic section are used to search multiple reflections. In the second case the computation of the complete high frequency synthetic section and the comparison with the real data allowed us to verify

how the 1-D velocity model of Table 3.1 well reproduces the complexity of the observed waveforms both in qualitative (Figure 3.4) and quantitative (Figure 3.5) way. Both these approaches could be used to refine a preliminary velocity model for complex structures.

Moreover, we have found that the evaluation of PS-to-PP amplitude ratios as a function of offset generally verified pre-critical amplitudes of the COMRAD synthetic seismograms, but also pointed to some problems in the post-critical offset range.

3.2 Forward modelling of seismic sources

In this section the COMRAD code is used to compute synthetic seismograms for an earthquake faulting source (a single-particle fault), considering the radiation pattern of the source. For these simulations the core (Farra and Madariaga, 1987) of the COMRAD code has been modified in order to take into account of the radiation pattern of the seismic source. In particular we have to consider in the model the strike, dip, and slip (or rake) angles, which give the fault orientation and the direction of the sliding motions on the fault.

However, we have to bear in mind that only far-field body waveform modelling can be carried out by ray-theory methods, such as the COMRAD code. Indicating with R and λ the source-receiver distance and the wavelength, respectively, this means that $R \gg \lambda$.

3.2.1 Faulting sources

Unlike an underground explosion, most seismic sources do not have spherical symmetry since the outgoing waves are influenced by the strain distribution near the source. The geometric description of the initial motion and amplitude near the source of P and S wavefields is called radiation pattern. The low-order symmetry for such a source provides relations between the fault-plane orientation and the radiation pattern.

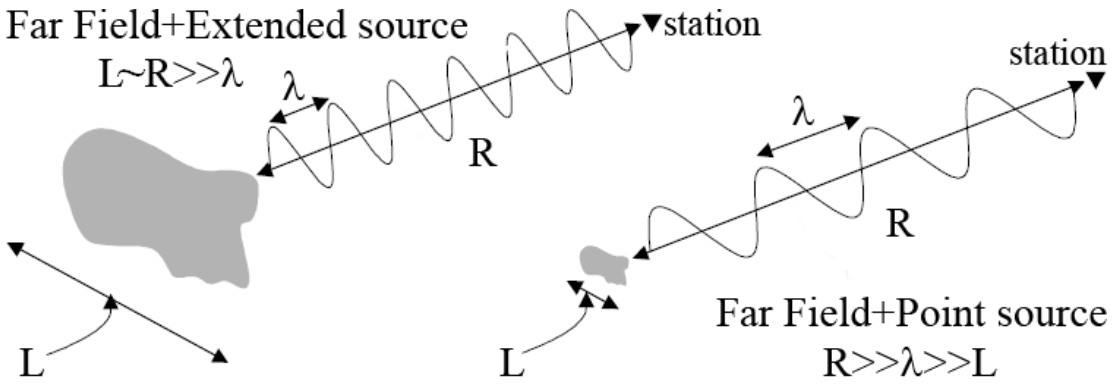

Figure 3.6: *Extended source (left) and point source (right) conditions in far-field approximation ($R \gg \lambda$). In the figure the source dimension is indicated by D, the source-receiver distance by R, and the wavelength by λ.*

When an earthquake occurs, the sliding motion start at a certain point called the earthquake hypocenter (or focus). A slip front expands outward over the fault with a rupture velocity v_r. Considering L the length of the fault, and λ the characteristic wavelength of the wavefield, the rupture area and the source volume can be approximated as a point source if $L \ll \lambda$, else the source must be considered as extended. Figure 3.6 shows both the point and the extended source cases, considering also the far-field condition.

The mathematical representation of the geometric nature of faulting is now introduced. We consider faulting as a slippage between two blocks of material[2], where the slip is constrained to lie in the plane connecting the two blocks (see Figure 3.7a). We call the strike θ of the fault the azimuth measured from north of the projection of the fault onto the surface; the dip δ of the fault is the angle measured downward from the surface to the fault plane in the vertical plane perpendicular to the strike; the slip λ is the angle measured in the plane of the fault from the strike direction to the slip vector (see Figure 3.7b). These three parameters describe the orientation of the fault plane in geographic coordinates. Finally, the magnitude of the slip vector is given by the total displacement D of the two blocks. The total displacement D is important to determine the seismic moment M_0 since:

$$M_0 = \mu A D \tag{3.1}$$

with μ the rigidity modulus, and A the fault area.

In general θ, δ, λ, and D can vary over the finite fault surface, but their average values can be used for simple model, as we have done in our simulations.

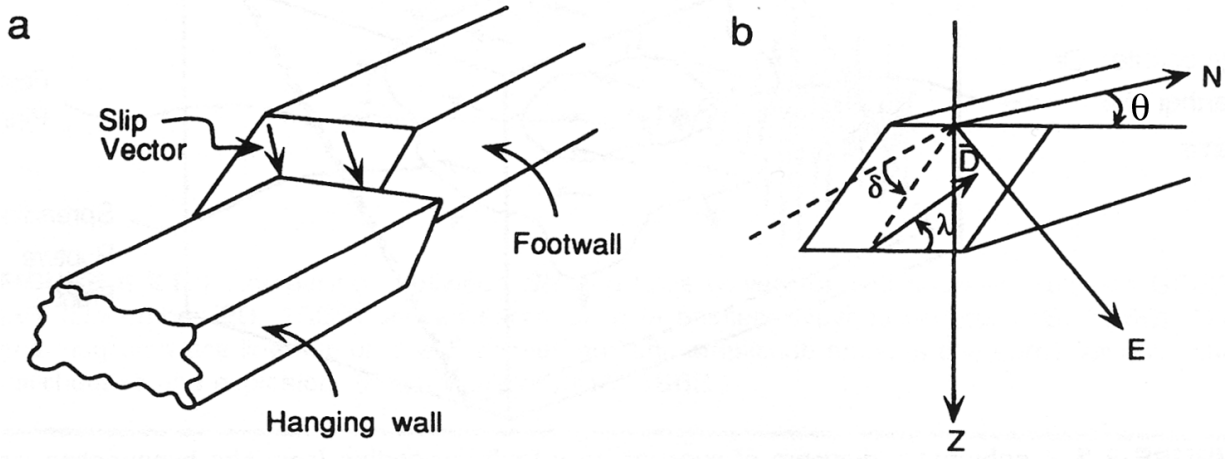

Figure 3.7: *Standard definition of fault-plane and slip vector orientation parameters. (a) The slip vector lies in the plane connecting the two blocks (the hanging wall and the footwall). (b) The strike θ, dip δ, and slip λ angles are defined. The figure was modified from Lay and Wallace (1995).*

[2]Conventionally, the block above the fault is called the hanging wall and the block below is called the footwall.

The motions on the fault can be divided in three basic categories:

1. **Strike slip fault**: When the two sides of a fault slip horizontally relative to each other, the motion is called pure strike slip, with λ equal to 0° or 180°, and if the dip $\delta = 90°$ the geometry is called vertical strike slip. In particular, for $\lambda = 0°$ the block of the other side of the fault moves to left, so the fault movement is called left-lateral slip; for the opposite case ($\lambda = 180°$) the fault movement is called right-lateral slip.

2. **Thrust fault**: When the slip vector is parallel to the dip direction, the motion is called dip-slip; if the dip $\delta = 90°$ the geometry is called vertical dip-slip. For $\lambda = 90°$, the hanging wall moves upward, causing thrust (or reverse) faulting. The thrust faults are generated by a compressive force system acting against the two blocks.

3. **Normal fault**: When a dip-slip motion occurs with $\lambda = 270°$, the hanging wall moves downward, causing normal faulting. The normal faults are generated by dilatational force system acting against the two blocks.

In general, λ will have a value different than these special cases, and the motion is then called oblique slip.

It was demonstrated (Lay and Wallace (1995); Aki and Richards (2002)) that an appropriate equivalent body-force system for an earthquake dislocation is the double-couple model. In fact the displacement field can be substituted by an equivalent field due to a distribution of equivalent double couples that are placed in a medium without any dislocation. This is one of the most important concepts in seismology, and it is used both for static and dynamic displacement modelling. Hence, in the following sections we intend the seismic source as a double-couple force system.

3.2.2 Synthetic seismograms for a vertical strike-slip point source

Here we will show and example of computing synthetic seismograms for faulting sources using the COMRAD code. This example considers a sigle-particle fault (a point-source) with a vertical strike-slip geometry ($\theta = 0°$, $\delta = 90°$, $\lambda = 0°$) and a left-slip movement, according to the convention introduced in section 3.2.1.

We have considered a simple propagation medium with two layers above a halfspace, as reported in Table 3.2. For each layer and the halfspace the elastic parameters have been set.

The source-receivers geometry is the following. We consider a source of 7 km in depth with the epicentre (its projection onto the surface) falling in the centre of an 8x8 km square. Eight receivers are positioned as follows: 4 receivers in the vertexes of the square 4 receivers inside the square; all the receivers are on the surface. If we consider the epicentre of the source as the origin of the coordinate system, the relative positions of the receivers are: R_1=(3,-3,0), R_2=(4,4,0), R_3=(-1,-2,0), R_4=(-4,4,0), R_5=(2,3,0), R_6=(-4,-4,0), R_7=(-2,3,0), R_8=(4,-4,0), where all quantities are expressed in km.

Interfaces	**Depth (km)**	Vp **(km/s)**	Vp/Vs	ρ **(g/cm^3)**
1	0	4.5	$\sqrt{3}$	2.6
2	3	6.0	$\sqrt{3}$	2.7
Halfspace	10	7.0	$\sqrt{3}$	2.7

Table 3.2: *Model used to compute synthetic seismograms for a vertical strike-slip point source. The source lies in the second layer, since it is at 7 km in depth.*

We have used the following convention for the X,Y, and Z coordinates: X is equal to the North, Y corresponds to the East, and Z is the vertical component with the positive axis downward (the same as in Figure 3.7b).

Since we were interested in the polarities of the first P-wave arrival (which are used to compute the focal mechanism of the source) and not to reproduce a seismogram as complete as possible, we have stopped the COMRAD's hierarchic ray generation to the 5^{th}, leaving the other parameters to the default value.

Figure 3.8 shows the vertical component of the synthetic seismograms (the displacement velocity) for R_2 and R_4 receivers. The polarity of the P-wave (the first arrival on the synthetic seismogram) at the R_2 receiver is down. This means that the P arrival is compressional (since Z in positive downward), then there is a motion away from the source. The opposite case is found at the R_2 receiver, where the P arrival is dilatational as a consequence of a motion toward the source. In the simulations we have considered as source-time function a Gaussian with duration of 0.1 seconds in order to include temporal and spatial fault finiteness. In general the source-time function is more clearly approximated by a trapezoid (Lay and Wallace (1995); Aki and Richards (2002)).

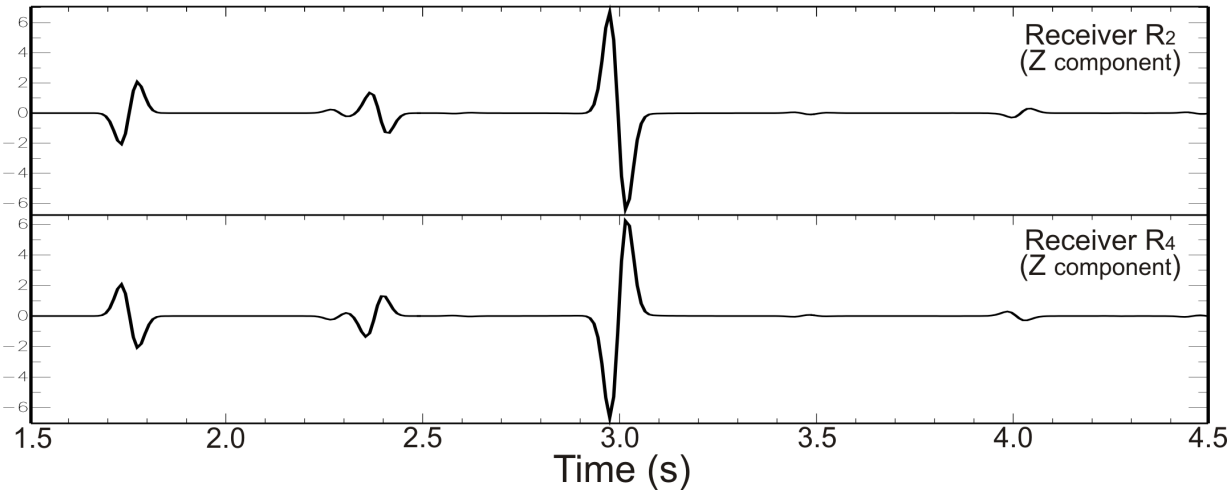

Figure 3.8: *Synthetic seismograms (Z comp.) for R_2 and R_4 receivers in the time window between 1.5 and 4.5 seconds after the origin time of the earthquake.*

As a trivial exercise, we have considered the synthetics as real data in order to perform a localization of the seismic source and the study of its focal mechanism. The localization was obtained using the HYPO71 program (Lee and Lahr, 1975), while the focal mechanism is obtained using the FPFIT program (Reasenberg and Oppenheimer, 1985).

The HYPO71 program localizes the source at the point of coordinates S=(0.03,0.00,7.11) km. The focal mechanism obtained from FPFIT program gives $\theta = 5°$, $\delta = 80°$, $\lambda = 0°$ with a left slip movement, as shown in Figure 3.9. This geometry is similar to the vertical strike-slip geometry used for the simulation. The result can become better if a large number of stations will be used.

It is possible to model also an extended source by considering N elementary point sources with the same focal mechanism of the extended source. In other words, the seismic source process can be thought of a series of N little earthquakes, each one starts according

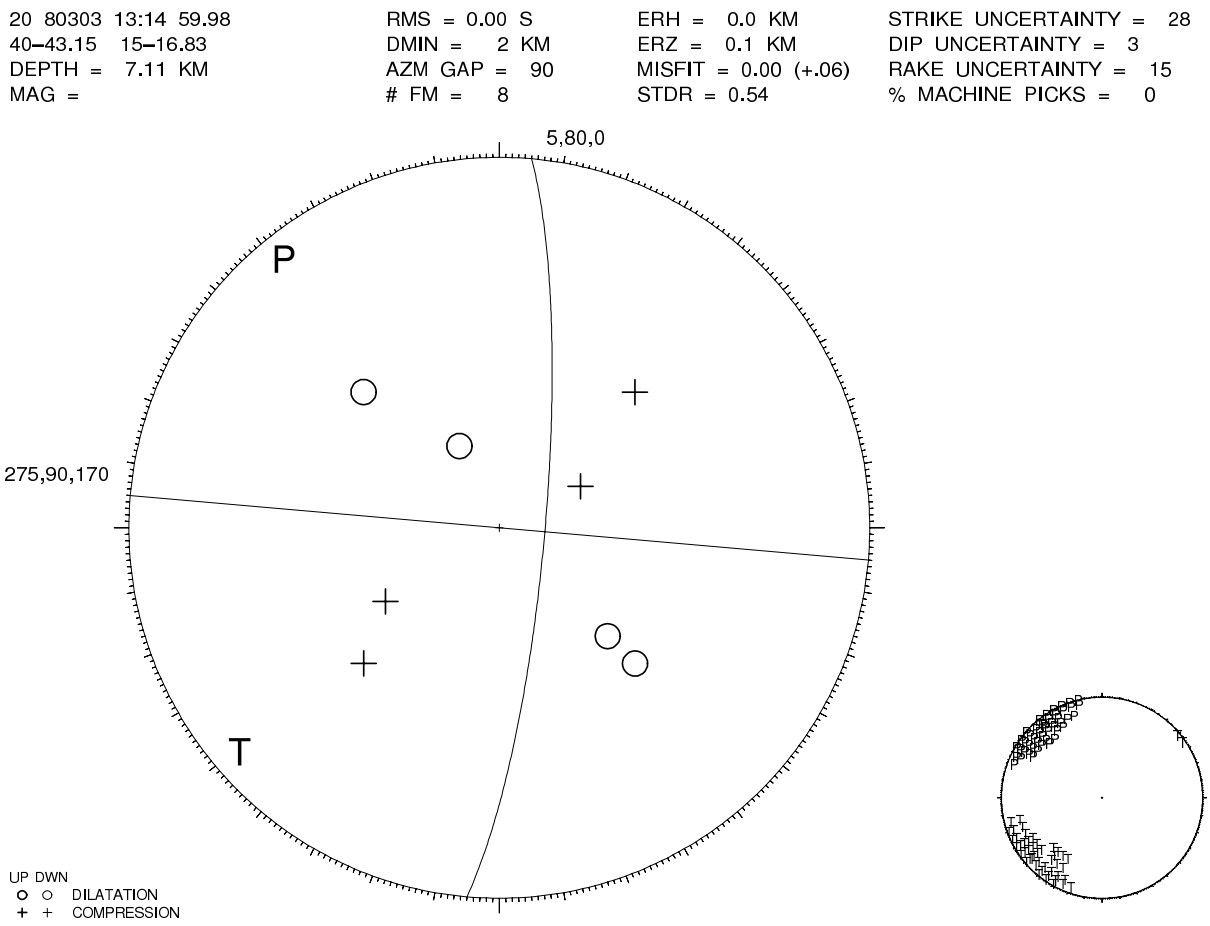

Figure 3.9: *Focal mechanism obtained from FPFIT program. The result obtained is similar to the geometry of the model used for the simulations. The + sign represents a compressional wave (motion away from the source), while the ◯ sign represents a dilatational wave (motion toward the source).*

to the time history of the extended source process. The first point-source activates at the origin time, the rupture propagates with a velocity v_r and the i^{th} source activates at the time t_i such that $t_i = \delta_i / v_r$, with δ_i the distance between the i^{th} and the $(i-1)^{th}$ source. Moreover, the total seismic moment M_0 must be given by the sum $M_0 = \sum_{i=1}^{N} M_{i0}$, with M_{i0} the seismic moment of the i^{th} source.

3.2.3 Conclusions and discussions

In this section we have shown an application of the COMRAD code earthquakes by considering the radiation pattern of the faulting source that generates the earthquake. A vertical strike-slip geometry for a single-particle fault has been considered in the example.

As a trivial exercise, we have considered the synthetics as real data in order to find the focal mechanism of the source and to localize it. The results show that the forward modelling of the seismic source using the COMRAD code is correct. Finally, the extended source case has been planned.

Although the code produces good results for the far field modelling of seismic sources, some work has to be done to assess the amplitudes for a given earthquake. In fact the synthetics do not have the exact amplitude values for a given seismic moment of the source, since this parameter is not included yet. We are plannig to provide in the future synthetic seismograms with amplitudes related to a given seismic moment.

Chapter 4

High frequency underwater acoustic propagation in the Gulf of Naples

Over the last ten years, there has been a rapid extension of the use of digital underwater acoustic communication from mainly military purposes to those commercial, to satisfy the growing needs for underwater acoustic wireless communication systems in real time and with the necessity to oversee the submerged instrumentation without the direct intervention of man.

Underwater acoustic wireless sensor networks are an emerging topic of research and are envisioned to enable applications on the surveillance and monitoring of sea areas (Adams *et al.*, 2000; Sozer *et al.*, 2000; Akyildiz *et al.*, 2005; Benson *et al.*, 2006; Jaffe and Schurgers, 2006). There is, in fact, significant interest in monitoring aquatic environments for scientific, environmental, commercial, safety, and military reasons such as detect tectonic movements, incoming tsunamis, water pollution, global warming, distributed tactical surveillance, mine reconnaissance, and many other facts that are bound to affect our lives (Badia *et al.*, 2006; Pompili *et al.*, 2006).

The main problem of underwater acoustic communication is the complexity of the marine acoustic channel: background noise from the environment and from human activities; unevenness in the water caused by the presence of solid and gaseous particles; the presence of spatial and temporal sound velocity gradients that can arise from salinity, pressure and temperature variations; multipath effects caused by multiple reflections on the sea surface and bottom; reverberations caused by the agitation of the sea and the topography of the sea bottom; and marine currents. In particular, with a digital communication system, the multipath that occurs with the propagation of signals results in intersymbol interference (ISI), which limits the capacity of the underwater acoustic communication channel. All of these phenomena are magnified in the situation of acoustic transmission in shallow water with respect to transmission in deep water, due to the depth of the sea and the closeness to the coast (Cazzolato *et al.*; Smith *et al.*, 2003), so the shallow water acoustic communication channel is characterized by strong signal degradation.

The use of high frequencies in acoustic communication improves the velocity of digital transmission of data, but also causes a greater attenuation of the signal (Thorp, 1967;

Fisher and Simmons, 1977), with the consequent decrease in the range of distance, i.e. in the ability to transmit data over distance.

To be able to complete any underwater acoustic communication system, it is necessary to know the physical properties of the transmission channel to be able to understand what the limits on signal transmission are and how its complexity can influence the quality of the information transmission.

In this Chapter we will show a work we have carried out to studying the physical properties of the water layer of the Gulf of Naples, which can be used as an acoustic communication channel for high-frequency digital transmissions (around 100 kHz). We have analyzed also the influence of the seasonal variations in its physical parameters on underwater transmission and the limits that the channel forces upon this communication. For this purpose we were interested to understand the effects produced by the underwater acoustic channel on a high frequency digital transmission to choose the best configuration of an underwater communication system that can be installed in the Gulf of Naples (Southern Italy). This kind of system shall extent offshore the geophysical monitoring of the Neapolitan volcanoes, Mt.Vesuvius and Campi Flegrei caldera.

In this study we did not take into account the effects of bubble scattering and absorption because the layer that contains bubbles is near the surface (Preisig, 2006) and, as our models use wind speeds less than 6 m/s, bubbles cannot significantly attenuate propagating signals in this layer (Dahl, 2004). We also have considered the sea as a steady propagation environment with smooth sea surface and seafloor during the transmission of data.

The simulations of the high frequency wavefield propagation in the Gulf of Naples have been carried out using the COMRAD code described in Chapter 2.

4.1 Physical properties of the Gulf of Naples

The Gulf of Naples is sited along the south-western coast of Italy, between 40°35' and 40°50' latitude North, and between 14°00' and 14°30' longitude East. The depth of the sea in the area of interest is not deeper than 300 m, except for the northern part of the Dohrn canyon (Figure 4.1), in which the sea depth reaches 400 m. Since the Gulf of Naples is not deeper than 300 m, it can be considered as a shallow water acoustic communication channel. This implies a bigger complexity on the sound propagation because in shallow water the surface, the volume, and the bottom properties are all important. Moreover the seasonal variation in sound-speed structure is significant with winter condition being nearly isospeed (Jensen *et al.*, 2000).

In the following pages we will describe the physical properties of the Gulf of Naples considered as a one-dimensional (1D) communication channel in shallow water. We will construct a velocity model for the seawater, considering that the average depth of this water layer is less than 300 m, and a geoacoustic model for the sea bottom. Moreover the potential noise sources are described, and the noise levels (NL) expected in the Gulf of Naples at the 100 kHz frequency are calculated.

4.1.1 Analysis of the weather conditions

In order to study the physical properties of the Gulf of Naples it is important to know the weather conditions because, as it will be shown in sections 4.1.2 and 4.1.3, the weather has an important influence on both the sea-water temperature and the underwater noise level.

Here we show the analysis of the air temperature, precipitations, wind speed, and wind direction in the Gulf of Naples. The weather data have been downloaded from the NOAA[1] website at the link http://www.arl.noaa.gov/ready/amet.html, taking the temperature (in °C) at 2 meters above the sea-level, the precipitations (in mm), the wind direction (in degrees respect to the North), and the wind-speed (in knots) at 10 meters above the sea-level. The database is sampled every 6 hours from the 1^{st} January 1997 to the 31^{st} December 2006, collecting a total number of 14549 data for each meteorological parameter.

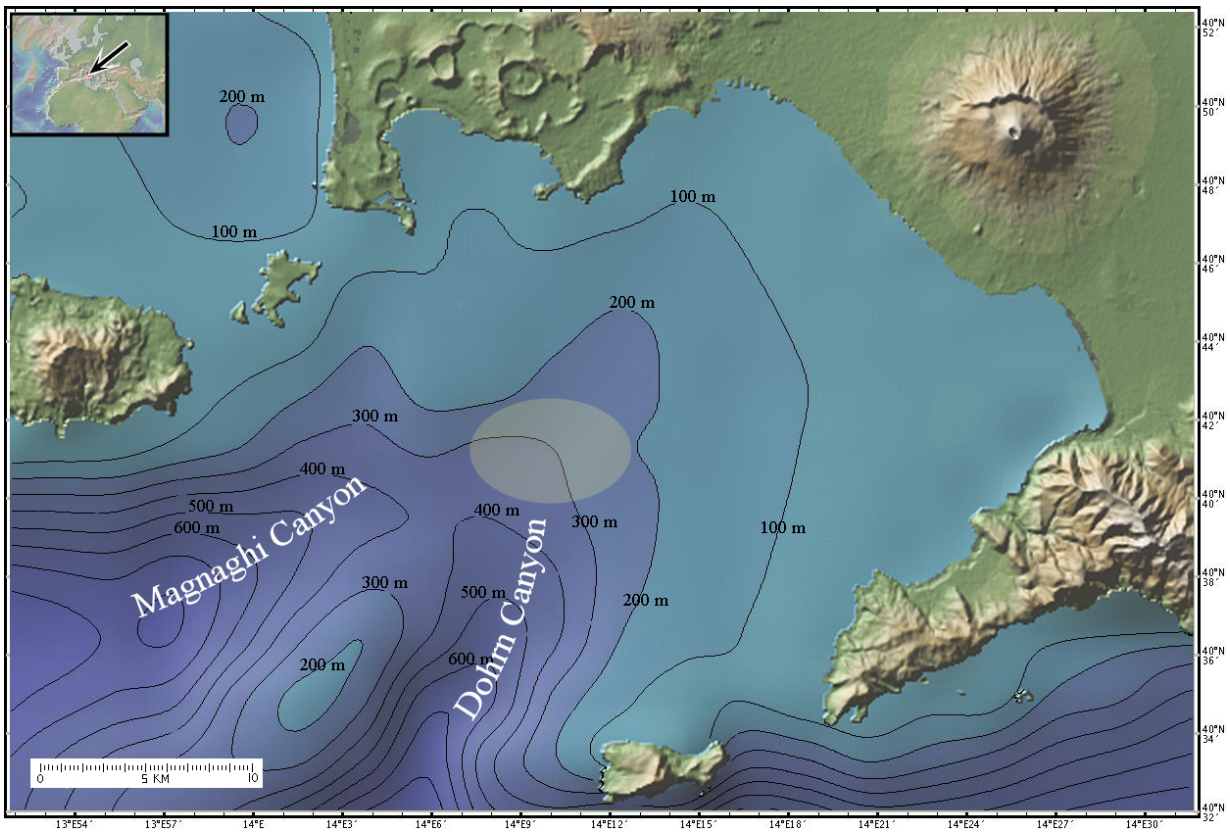

Figure 4.1: *Bathymetric and topographic image of the Gulf of Naples. A bright ellipse indicates the area of interest for our studies, where the researchers of the Anton Dohrn Zoological Station carried out measurements of the physical properties of the sea water in the period from February 2002 to February 2003.*

[1]National Oceanic and Atmospheric Administration, USA.

We have calculated from the data the mean values and their standard deviations for the air temperature and the wind speed in the Gulf of Naples during the year. In Figure 4.2 the mean air temperature at 2 meters above the sea level (on the left) and the mean wind speed at 10 meters above the sea level (on the right) in the Gulf of Naples are reported. The mean values are plotted with a red line, while the ± one deviation standard curves are plotted with blue and green lines, respectively. From the left side of Figure 4.2 it is possible to note that in general there is a thermal excursion between coldest months (January and February) and the hottest months (July and August) of about 15-20 degrees. The lowest temperature in the data is 2.4 °C and it was reached at the midnight of the 31^{st} January 1999, while the highest is 31.1 °C and it was reached at the noon of the 9^{th} August of the same year. These variations influence the water temperature in the surface layer of the sea since there is a thermal exchange between the sea and the air above. In table 4.1 the mean annual air temperature in the Gulf of Naples from 1997 to 2006 is reported. The coldest year was 2005, with a mean temperature of 16.3 °C, and the hottest year was 2003, with a mean air temperature of 17.6 °C. No linear trends of the air temperature are founded during this period in the Gulf of Naples.

Year	1997	1998	1999	2000	2001	2002	2003	2004	2005	2006
T(°C)	16.8	16.7	16.4	17.1	17.4	17.3	17.6	17.0	16.3	16.7

Table 4.1: *Mean annual temperature in the Gulf of Naples from 1997 to 2006.*

Looking to the right side of Figure 4.2 it is possible to see that the mean value of the wind speed does not change so much from winter to summer in the Gulf of Naples. In

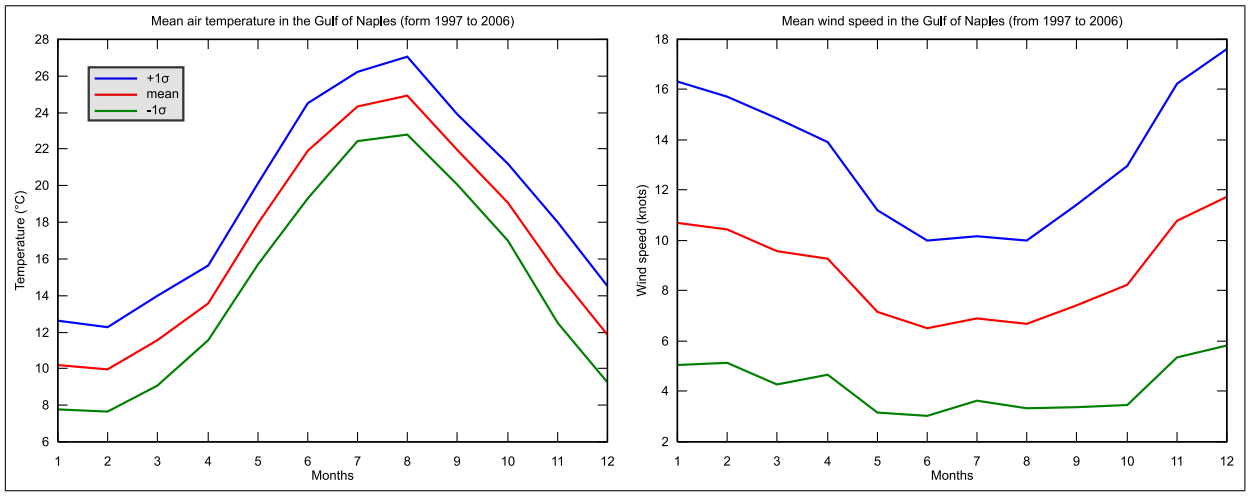

Figure 4.2: *Mean air temperature and wind speed in the Gulf of Naples during one year, calculated from 1996 to 2006. The red curves indicate the mean values of air temperature and wind speed, while the blue curves and the green curves are the $+1\sigma$ and the -1σ curves, respectively.*

fact the mean wind speed varies between about 7 knots in June and nearly 12 knots in December. According to the Beaufort Scale[2] the sea conditions change on average from gentle Breeze (force 3, equivalent to 7-10 knots) in summer to moderate Breeze (force 4, equivalent to 11-16 knots) in winter. From 1997 to 2006 the lowest wind velocity was equal to 0.1 knots (force 0 $\rightarrow$ Calm) while the highest wind velocity was equal to 40.9 knots (force 8-9 $\rightarrow$ Gale). As shown in Figure 4.2 the standard deviation of the wind speed is about 5 knots for each month, a very high value that implies a big variation of the sound speed independently of the season taken into account. The Figure 4.3 shows the frequency of the wind direction for each month. The wind direction is expressed in degrees respect to the North. From April to September the most common wind direction is 270° (West wind), with a probability of 30%. In the same period there is also a probability of $15-20\%$ that the wind direction is 315°; this is the Mistral. In particular in July and August both the Mistral and the West wind can occur with the same probability. Finally from January to March in the $50-60\%$ of cases the wind can blow with an angle of 45° (East Wind), 270° (West Wind), or 315° (Mistral). During the other periods of the year no favourite wind direction is observed.

The wind speed is partially correlated to the precipitation since the latter indicates bad weather conditions, when the wind speed reaches high values. In fact the most dry months are May, June, and July (when the wind speed reaches the lowest values) with a total precipitation less than 30 mm, while from September to December the total precipitation is greater than 70 mm, as shown in Table 4.2. In particular the rainiest month is December with a total precipitation of 100 mm. Between 1997 and 2006 there were also big differences in total precipitation from one year to each other, with a minimum of 383 mm in 2001 and a maximum of 991 mm in 2005.

Month	Jan	Feb	Mar	Apr	May	Jun	Jul	Aug	Sep	Oct	Nov	Dec
Rain (mm)	67.2	46.8	45.5	53.2	27.4	23.2	21.2	34.8	81.6	77.3	83.4	100.0

Table 4.2: *Monthly total rain fallen in the Gulf of Naples (mean value from 1997 to 2006). The most rainiest period is from September to January, while the most driest period is from May to August.*

In summary, both the wind speed and the air temperature are important weather parameter to be considered because they influence the water temperature and, as it will be discussed in section 4.1.2, the sound velocity in the seawater depends strongly on the water temperature. Moreover, the wind speed produces also noise in the seawater due to the breaking of the waves.

[2]The Beaufort scale is an empirical measure for describing wind velocity based mainly on observed sea conditions.

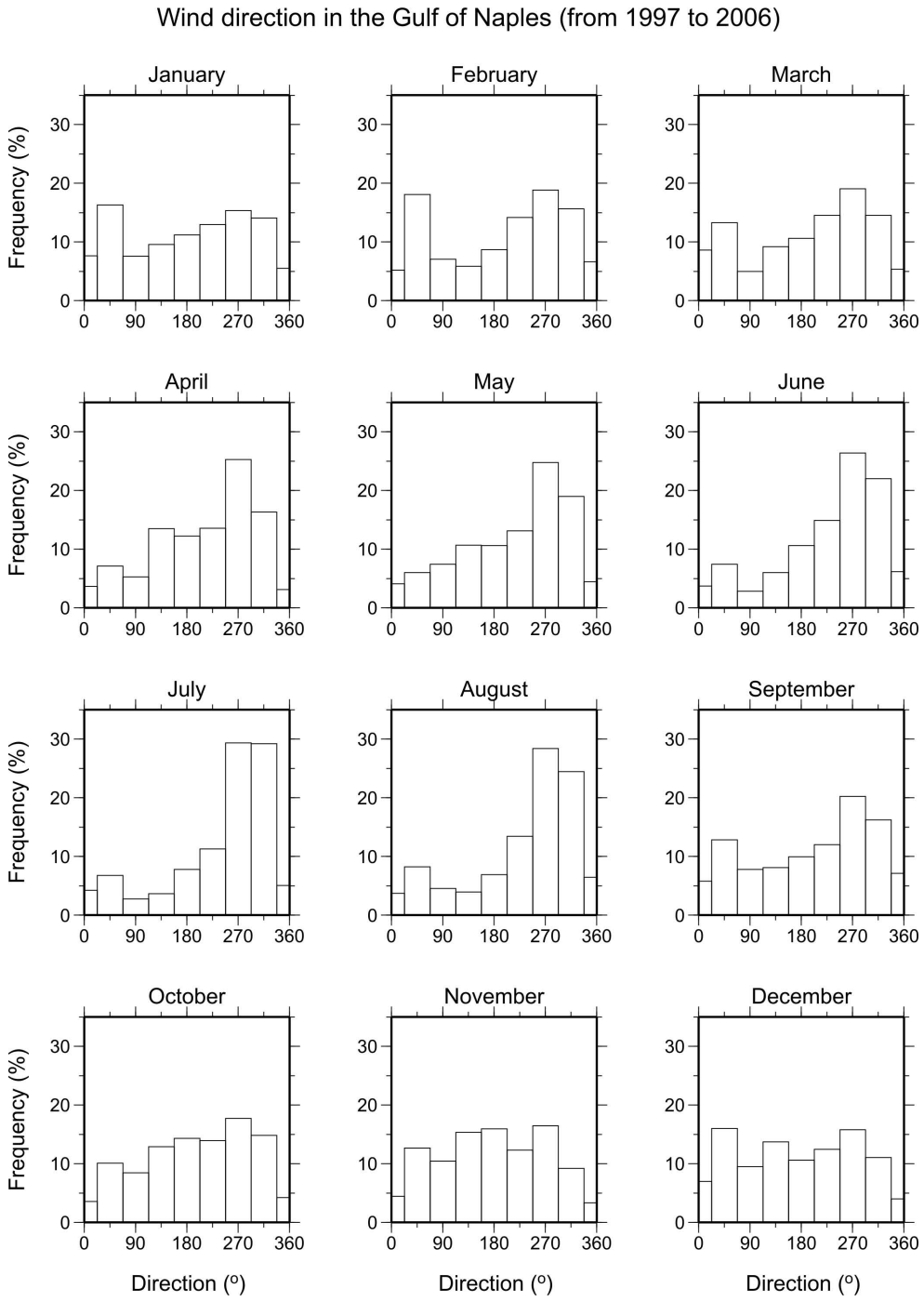

Figure 4.3: *Monthly frequency of the Wind direction respect to the North in the Gulf of Naples. The most frequent winds from January to March are the North-east Wind, the West Wind, and the Mistral, while from April to September are the West Wind and the Mistral.*

4.1.2 One-dimensional velocity and geoacoustic model of the Gulf of Naples

The essential characteristic of sea water is, in fact, the velocity at which the sound can be propagated through it. The square of the velocity of the sound depends then on the ratio between the density and the bulk modulus of the propagation medium. In particular, in the sea the density is a function of the pressure, temperature and salinity of the sea, while the bulk modulus is a function of the pressure and temperature of the sea; for this reason, the propagation velocity of acoustic energy in the sea can be described as a function of three physical parameters: pressure, temperature and salinity (Jensen *et al.*, 2000). It is not only necessary to know the mean values of these three physical parameters for the sea, but it is also important to know their spatial and temporal variabilities, as these variations significantly modify the propagation velocity of the acoustic waves in the sea. Over the years, various formulae have been suggested that link the sound velocity in the sea to the three parameters of pressure, temperature and salinity (Coppens, 1981; Mackenzie, 1981; Kinsler *et al.*, 2000), and in particular, the UNESCO algorithm (Chen and Millero, 1977; Wong and Zhu, 1995) and the equation of Del Grosso (Del Grosso, 1974) are commonly used.

If the sea is considered to be a resting fluid with a constant density ρ, the pressure is solely a function of the depth. There are also some very accurate, empirical relationships between sea depth and pressure. The sea temperature and salinity, however, depend upon the ambient conditions of the location, such as the solar irradiation, evaporation, the atmospheric conditions, the water circulation, the wind, the presence of rivers, and the geographical position.

The characterization of the Gulf of Naples starts, therefore, from the knowledge of the values and variabilities of these parameters in space and time. For this, the temperature and salinity data were analyzed from measurements carried out by the researchers of the Anton Dohrn Zoological Station (Ribera, personal communication, 2005) in the Gulf of Naples from the sea surface to a depth of 300 m, in the period from February 2002 to February 2003. The sound velocity data, calculated by the same with the equation of Del Grosso (Del Grosso, 1974) from these salinity and temperature measurements, were analyzed.

Figure 4.4 shows the salinity profiles of the sea between the surface and the bottom at 300 m in depth, with a sampling rate of 0.1 m, across 15 different periods of the year. The salinity went through small variations during the whole year, with a value of about 38 ppm. It can be seen from Figure 4.4 that there was an increase in the salinity with depth of about 0.5 ppm, from the surface to the bottom, and also rapid oscillations in the salinity values in the first 100 m in the non-winter periods due to surface marine currents, where at some depths the salinity can change of about 2 ppm from the mean value. In the winter periods, the strong agitation of the sea causes a mixing of the water down to great depth, resulting in stability of the salinity values.

Figure 4.5 shows the temperature profiles measured at the same time as the salinity at the same depths. The temperature varies with time, and on large spatial scales, in con-

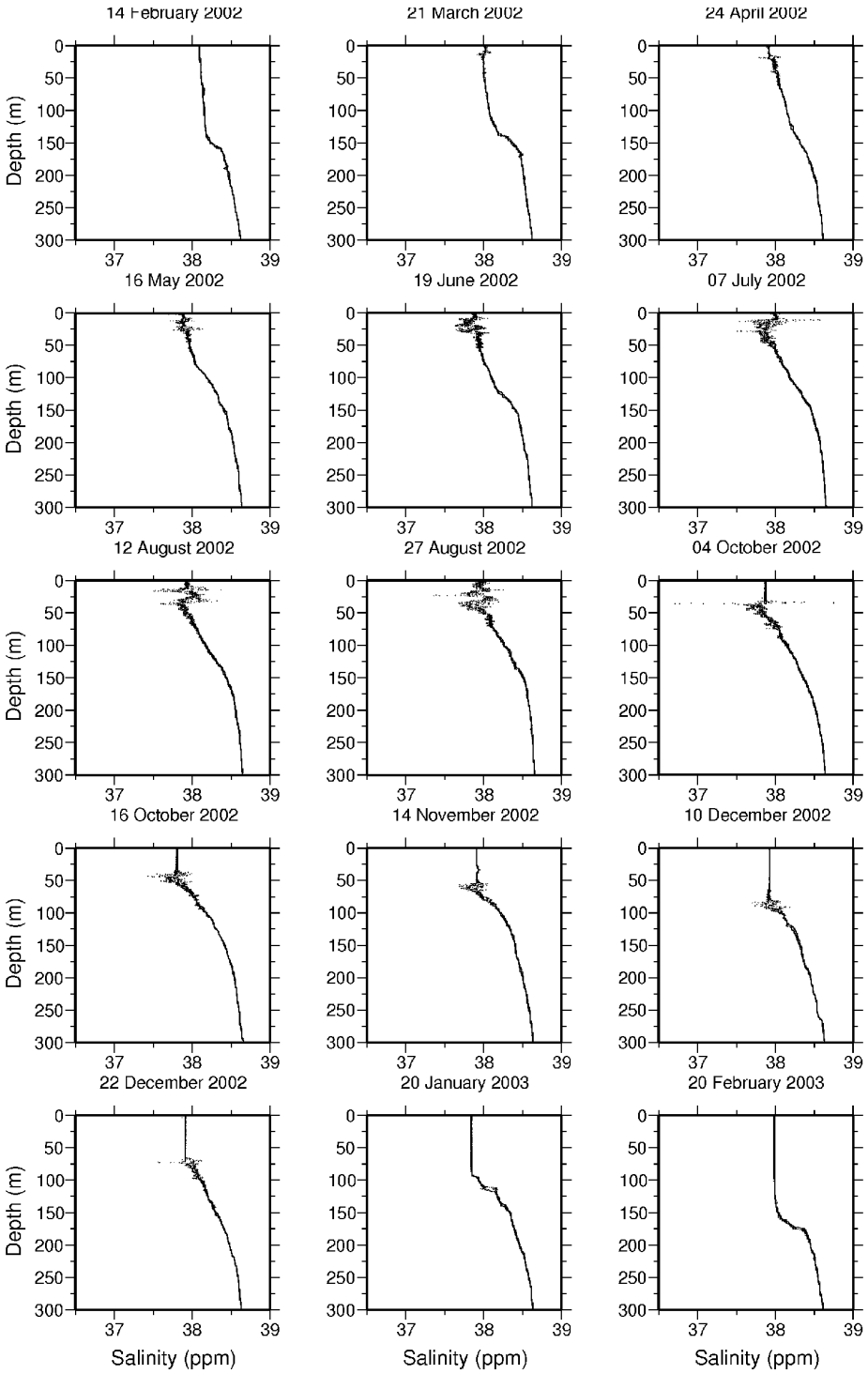

Figure 4.4: *Salinity profiles in the Gulf of Naples from the sea surface to the bottom, at 300 m in depth, measured across 15 different periods between February 2002 and February 2003.*

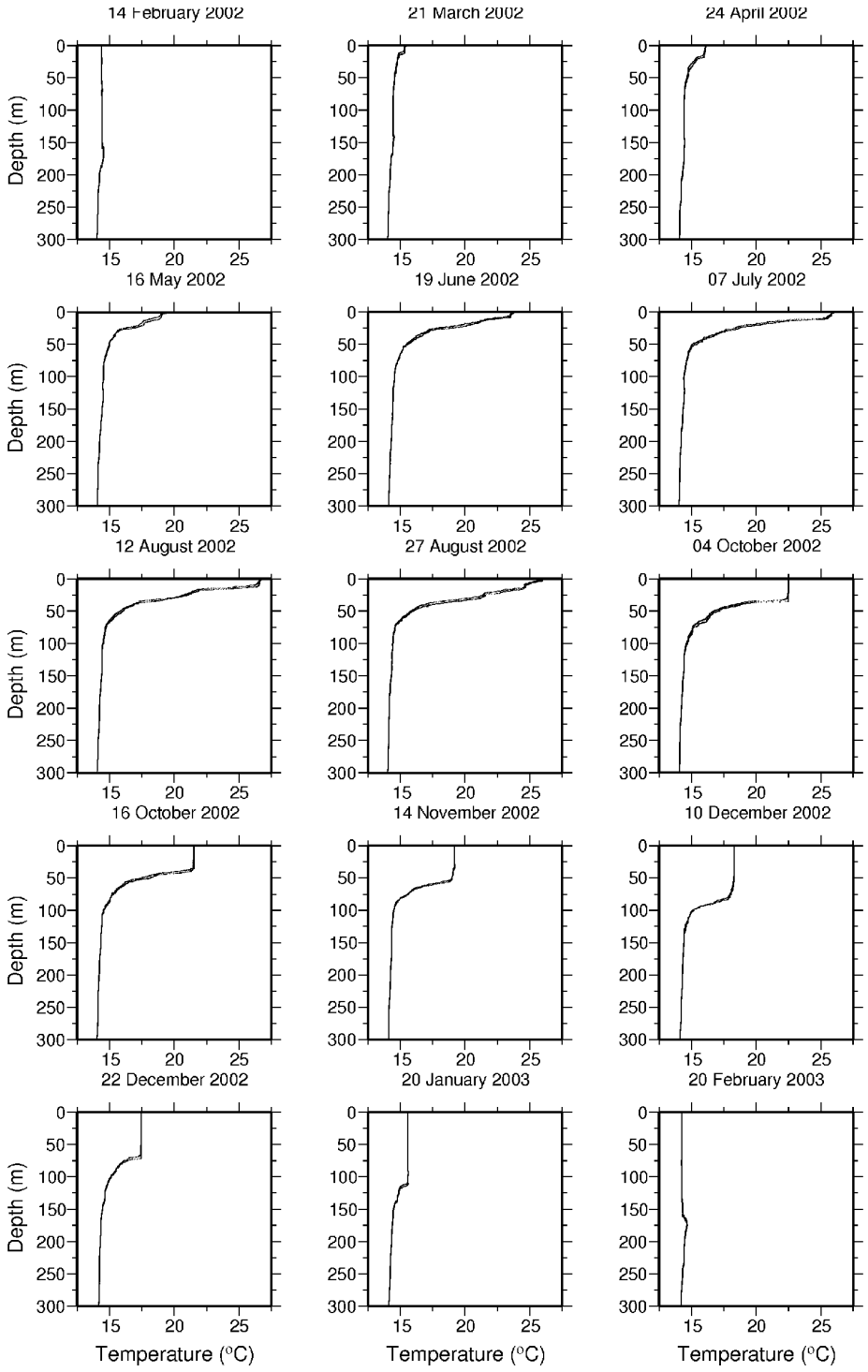

Figure 4.5: *Temperature profiles in the Gulf of Naples from the sea surface to the bottom, at 300 m in depth, measured across 15 different periods between February 2002 and February 2003. The main temperature variations are above 50 m depth. For depths greater than 160 m the seasonal temperature variation rarely reaches 0.1 °C.*

comitance with the daily and seasonal variations of solar irradiation; fine spatio-temporal variations are determined locally by turbulent movements of the seawater. The variability in the temperature of the sea depends on the variability of the thermal content of the water as a consequence of the heat transfer between the surface and the adjacent atmosphere (De Dominicis Rotondi, 1995). From Figure 4.5, it can be seen that at the surface the higher temperatures are reached in the summer months, with maximum values of 27 °C in August, while the lowest temperatures are reached in the winter months, with minimum values of 13 °C in February; in the deepest water, the mean temperature is lower and the temperature variations between the summer and winter seasons are greatly reduced. In summer, water mixings hardly and results in a large negative temperature gradient in the first 75 m of depth, where the temperature can drop from 27 °C at the surface to 14 °C at 75 m in depth. In autumn and winter, the mixing of the water is very intense, which generates isothermic surface layers that reach down to a depth of 50 m in October to 160 m in February. For depths greater than 160 m the mean temperature is 14 °C and its seasonal variation rarely reaches 0.1 °C; at this depth the temperature is no longer influenced by the outside meteorological conditions.

Figure 4.6 shows the sound velocity profiles calculated with the equation of Del Grosso (Del Grosso, 1974), starting from the salinity and temperature data. In this figure, it is possible to infer that the highest variations in the sound velocity are at the surface, and are between 1508 m/s and 1541 m/s, equivalent to a percent variation of $\pm 1\%$ of the mean velocity value. At increasing depths, the seasonal variations decrease until they become less than 5 m/s below 100 m and negligible below 160 m. A comparison between the sound velocity profiles with those of temperature reveal an overall correlation at all depths for all the periods of the year, except for a positive linear trend followed by the sound velocity profiles for increasing depths, caused by a raise in pressure with growing depth. From 160 m to 300 m in depth, where the temperature variations are negligible, the velocity only depends upon the pressure variations, increasing by around 2 m/s. The comparison between the salinity and sound velocity profiles shows that the rapid salinity oscillations in the hottest months, and for depths less than 100 m, do not correspond to appreciable variations in the sound velocity profiles, since the latter are less then 0.5 m/s (that is 0.03% of the mean sound velocity in the seawater). Consequently, the rapid variations in salinity have not been considered in the construction of a sound velocity model of the Gulf of Naples.

The knowledge of the effects of the three physical parameters of temperature, pressure and salinity on the sound velocity profiles has allowed the construction of a multiparameter function of depth z that simulates the sound velocity profiles throughout the year and for depths from 0-300 m in the Gulf of Naples, assuming that the variations seen over the sampling period are stationary. The parameters of the function were obtained through the inversion of the 15 sound velocity profiles using the non-linear Simplex global optimization algorithm (Nelder and Mead, 1965; Press *et al.*, 1992) and creating a function of time for each parameter that interpolates the values obtained from the inversion. The chosen

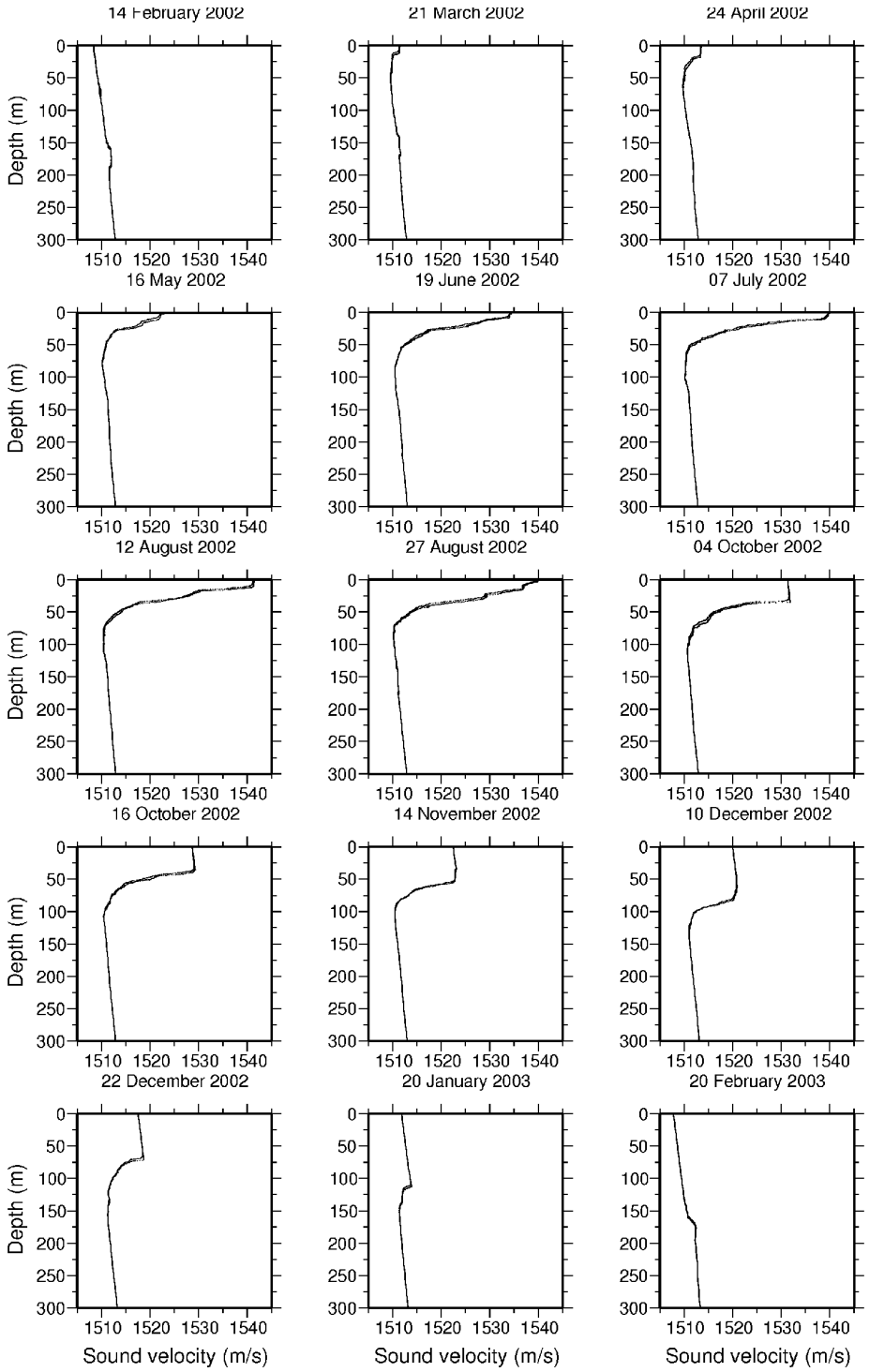

Figure 4.6: *Velocity profiles in the Gulf of Naples calculated from the salinity and temperature data obtained from the measurements carried out between February 2002 and February 2003.*

multiparameter model is described by the following function:

$$V(z) = \frac{V_0}{1 + (z/z_c)^{\gamma}} + \alpha + \beta z \tag{4.1}$$

The linear dependence with depth (βz) expresses the increase in the mechanical pressure. The parameter α represents the value of the sound velocity in sea water at a temperature of 15 °C and a pressure of 1 atm (depth of $z = 0$ m); the parameter V_0 represents the variation with respect to α in the sound velocity at the sea surface for a different temperature. The parameter z_c gives information on the thickness of the surface isothermic layer. The dimensionless parameter γ amplifies the z/z_c ratio and determines the negative slope of the function V(z) for $z \approx z_c$.

Using equation (4.1), a mean velocity profile was constructed for the summer and winter months, with the aim of studying the behaviour of the acoustic propagation according to the variations in the sound velocity in the sea; the two velocity profiles are shown in Figure 4.7. We have also calculated (Figure 4.7) the residuals for the summer and winter months as the difference between the values of the mean velocity profiles constructed using equation (4.1) and those calculated using the profiles of Figure 4.6. The residuals are less

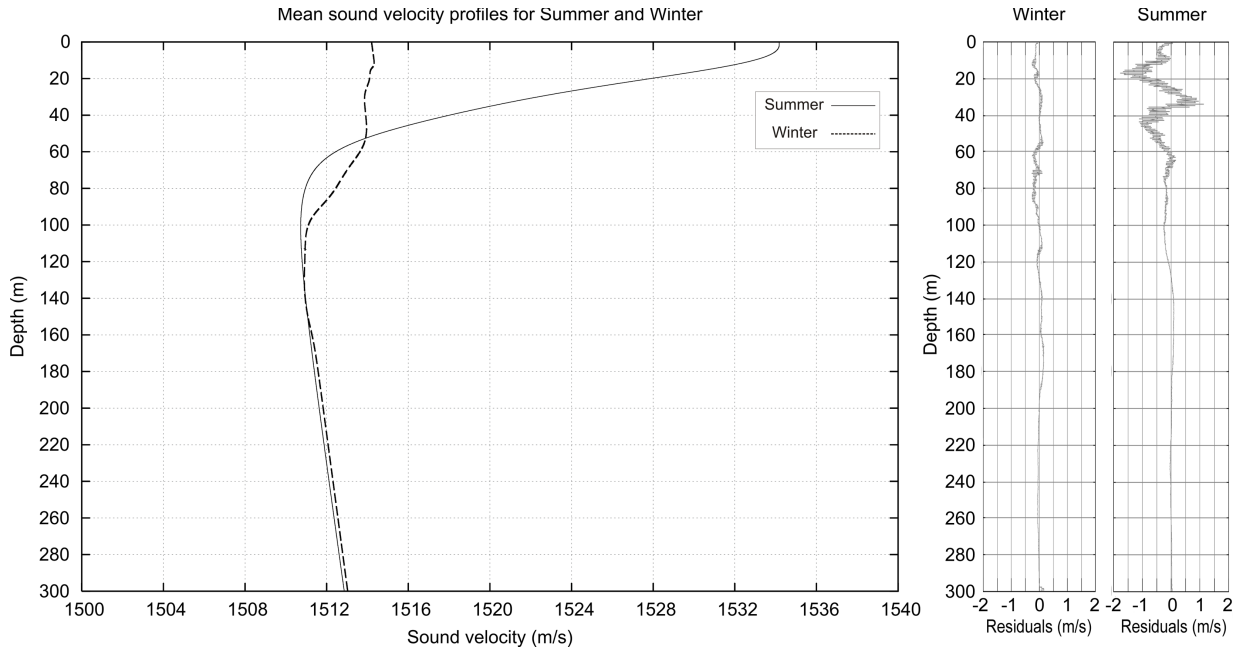

Figure 4.7: *Mean velocity profiles (left) for the summer and winter seasons calculated from equation (4.1) and residuals (right) evaluated respect to the mean velocity profiles computed using the 15 velocity profiles obtained from data. Below 50 m depth the residuals are less than 0.5 m/s for both summer and winter mean velocity profiles.*

than 0.5 m/s for both summer and winter mean velocity profiles, except for the first 50 m

depth in summer profile where the residuals can reach a maximum value of 1.8 m/s (only 0.1% of the sound velocity in the water).

Once the velocity model of the seawater is constructed, it is important to characterize also the sea bottom that means to define a geoacoustic model of the seafloor. The sediments samples taken from the first few meters of the sea bottom in the Gulf of Naples show that it is composed by clayey silt sediments in the first five meters and sand-silt-clay sediments below, because of lower percentage of silt. From Hamilton studies on physical properties of marine sediments (Hamilton, 1979a, 1979b, 1980) we can therefore define a geoacoustic model of the seafloor in the Gulf of Naples assigning, for each solid layer, the thickness, the sound velocity (P waves), the Vp/Vs ratio, and the density.

Stratum typology	***Thickness (m)***	***Sound velocity Vp (m/s)***	***Vp/Vs***	***Density (g/cm^3)***
Sea water	300	1510-1534	∞	1.03
Clayey silt	5	1550	13.0 ± 2	1.40
Sand-silt-clay	∞	1650	9.4 ± 2	1.80

Table 4.3: *Values of the physical parameters of the propagation medium for the Gulf of Naples.*

The propagation medium for the Gulf of Naples is described assuming a sea water layer and two solid layers (sea bottom sediments). The values of the physical parameters of the propagation medium are given in Table 4.3. We also consider a variation of the Vp/Vs ratio for both the solid layers since water saturation and porosity[3] may be different for the same sediment composition.

	Depth (m)										
	0	**10**	**20**	**30**	**40**	**50**	**60**	**80**	**100**	**160**	**300**
Summer model Vp (m/s)	1534	1533	1527	1523	1517	1514	1512	1511	1510	1511	1513
Winter model Vp (m/s)	1514	1514	1514	1514	1514	1514	1513	1512	1511	1511	1513

Table 4.4: *Sound velocities of the summer and winter models for increasing depths. The main differences between the two models are above 50 m depth..*

The discontinuity surfaces between the layers are flat and horizontal and no rough sea surface and seafloor are considered. Within the water layer, the sound velocity is assumed to vary continuously with depth, following the trend given in Figure 4.7. The model that describes the characteristics of the propagation medium in the summer months essentially differs from the one relative to the winter months in terms of the sound velocity values in

[3]The change of sediment porosity and water saturation influence the rigidity of the sediment structure, then the Vp and Vs velocities. The reduction in the value of Vp/Vs is due to open, dry or undersaturated cracks, but the Vp/Vs ratio increases as these cracks fill with water.

the water layer above the cut-off depth of about 50 m. Table 4.4 gives the sound velocity values for the two models at increasing depths.

4.1.3 Noise sources up to a frequency of 100 kHz

The noise signal of an underwater acoustic sensor is composed by electronic and acoustic noise, generated by the pressure fluctuations in the sea water due to the action of ambient sources (De Dominicis Rotondi, 1996).

Here, we consider only acoustic noise, and in particular we calculate the noise level around a frequency of 100 kHz in the Gulf of Naples. Analytically, the noise level (NL) will be expressed in decibels (dB) as the ratio between the noise pressure (or intensity) revealed with omnidirectional hydrophones and a reference pressure (or intensity) of a plane acoustic wave in the same frequency bandwidth. Typically, the reference pressure level used in underwater acoustics is 1 μPa.

In the sea, there are various noise sources that are both artificial and natural, which have intensities that vary in time, space and frequency. The natural sources have physical origins (molecular thermal agitation, sea tides and turbulence), meteorological (wind, rain, hail, storms, wave backwash, glaciers), terrestrial (earthquakes, volcanoes, distant storms) and biological (cetaceans, crustaceans, fish); the artificial sources are due to human activities, like seaside traffic, coastal industrial works, ports, boreholes for research into energy sources, and underwater acoustic communications besides those of interest.

This noise covers a vast frequency range that goes from frequencies lower than 1 Hz to frequencies higher than hundreds of kHz. For the various frequency ranges, the trend of the spectrum shows particular characteristics as a consequence of the peculiarities of the various sources: each source has its own dominant frequency band in which it has a predominant aspect with respect to the other noise sources; sometimes, different sources can predominate in the same frequency band.

The range going from a few kHz to 100 kHz is of interest in our study and is dominated by the noise generated by the impact on the sea surface of drops and water spray that arise from the breaking of the waves. A classical representation of the spectral distribution in the range from 100 Hz to 25 kHz comes from the historic Knudsen curves (Knudsen *et al.*, 1948), which came from a vast measurement campaign carried out during the Second World War by a group of researchers guided by V.O. Knudsen, along the coastal waters of various ocean regions. The curve, parameterized according to the condition of the sea or equivalently as a function of the wind velocity (in knots), shows a linear trend on a logarithmic frequency scale with a slope of around -20 dB/dec. A series of subsequent investigations in the Knudsen range, carried out by Wenz (Wenz, 1962) and Urick (Urick, 1986), established a correlation between wind speed and the ambient noise spectrum level. Using the empirical formulae given by Coates (Coates, 1990; Stojanovic, 2006), it is possible to calculate the noise level (NL), from 1 Hz to 1 MHz, as a function of frequency (in kHz), wind speed w (in m/s) and shipping activity factor s, whose value ranges between 0 and 1 for low and high activity, respectively. From these formulae it is possible to infer that the shipping activity factor s is negligible at frequencies of about 100 kHz.

The calculation of the noise level of the Gulf of Naples, for a frequency of 100 kHz, was carried out using Coates formulae and the mean wind velocity in the Gulf of Naples for both the summer and winter months. The wind velocities at 10 m above see surface were considered with the READY program starting from the FNL model (the model and program are available on-line on the website of the National Oceanic and Atmospheric Administration) they were sampled every six hours from February 2002 to February 2003, the period in which the measurements of the physical parameters of the sea were taken. The mean wind velocity calculated for the summer months was 3.9 m/s, while for the winter months it was 5.6 m/s. The noise levels in the Gulf of Naples at the frequency of $f = 100$ kHz are then 28 dB/μPa in summer and 30 dB/μPa in winter.

4.2 Simulations of acoustic signal propagation at 100 kHz

The knowledge of the physical parameters and the use of the function designed to simulate the sound velocity variations with depth and time in the Gulf of Naples has allowed us to carry out various simulations of high frequency acoustic propagation in the Gulf of Naples. Below, we describe the calculation method used for the simulation of the signal propagation and for the calculation of the signal-to-noise ratio.

4.2.1 Methodology used for the simulation of the signal propagation

Using the model described in the Table 4.3 of the section 4.1.2, we have calculated synthetic seismograms for different source-receiver configurations. Moreover, we have changed the Vp/Vs ratio for both the solid layers following the values reported in the model of Table 4.3 to understand if it influences the signal propagation.

The simulations were carried out using the COMRAD code with modifications in its core program[4] to allow for the anelastic attenuation in the sea, which is considered by multiplying for each phase (direct P, multiple P reflections in the water) the amplitude of the non-attenuated wave A_0 by a negative exponential:

$$A = A_0 \exp(\alpha x) \tag{4.2}$$

where α is the attenuation coefficient and has the dimensions of inverse length and x is the length of the ray-path.

From the empirical Thorp's formula (Thorp, 1967; Fisher and Simmons, 1977; Jensen *et al.*, 2000):

$$\alpha'(dB/km) = 3.3 \cdot 10^{-3} + \frac{0.11 f^2}{1 + f^2} + \frac{44 f^2}{4100 + f^2} + 3.0 \cdot 10^{-4} f^2 \tag{4.3}$$

[4]The core program is the 3D dynamic ray-tracing code developed by V. Farra (see chapter 2).

the attenuation is expressed as a loss in decibels per unit of distance as a function of the frequency f (in kHz) of the wave that propagates in the sea and it is indicated by α' (Jensen *et al.*, 2000), instead of α (see Appendix B.2 for more details on the sound attenuation in seawater). From the equation (4.3) and considering a frequency of 100 kHz we find that α' is equal to 34.3 dB/km. Taking into consideration equation (4.2), we can obtain α from α' as follow:

$$\alpha' x \equiv -20 \log\left(\frac{A}{A_0}\right) \simeq 8.686 \alpha x \Rightarrow \alpha \simeq \frac{\alpha'}{8.686} = 3.95 km^{-1} \tag{4.4}$$

To study the reliability of the acoustic communication, we simulated the propagation from the transmitter to the receivers of a signal consisting of a sinusoidal transient of 1 s duration and with a frequency of 100 kHz.

The transmitter, i.e. the source of the signal, is omnidirectional and was positioned at the three different depths of 1 m, 190 m and 299 m from the sea surface; for each transmitter position, the reception of the signal was simulated on a grid of 21x12 receivers, disposed in a vertical plane inside the area of interest shown in Figure 4.1 by a bright ellipse. The horizontal distance between the receivers is $\Delta x = 100$ m from the vertical axis through the source for up to 2 km in distance, while the vertical distance between the receivers is $\Delta z = 25$ m, from 5 m in depth to 280 m in depth.

For each receiver, the particle displacement velocity $\mathbf{v} = (v_x, v_y, v_z)$ was simulated, from which it is possible to deduce the intensity of the signal, information that is useful for the determination of transmission losses. Indeed, the instantaneous acoustic intensity I of field produced by force F that acts normally on a unitary surface A is $I = Fv/A = pv$, where p is the pressure and v is the particle displacement velocity along the normal to the surface A. Considering that the time-scale of oceanographic changes is order of magnitude greater than the time-scale of acoustic propagation, it can be assumed that the density ρ and the sound velocity c are independent of time. With this assumption, both the pressure p and the velocity potential Φ ($\mathbf{v} = \nabla\Phi$) satisfy the wave equation, and using the linearized Euler equation (Jensen *et al.*, 2000), this gives:

$$p = \rho c v \Rightarrow I = \rho c v^2 \tag{4.5}$$

where v is the particle displacement velocity along the direction of acoustic wave propagation.

Calculating therefore the particle displacement velocity $\mathbf{v}$ as a function of the time t in a certain point of the space, it is possible to obtain the intensity I of the field using the equation (4.5).

4.2.2 How to calculate the signal-to-noise ratio (SNR)

An object that radiates with a source level (SL) will be registered by a receiver with a lower signal level (S) due to the transmission loss (TL) that it undergoes in its passage

through the propagation medium. The signal-to-noise ratio (SNR) for this receiver is obtained by subtracting the noise level (NL) from the signal level (S), such that:

$$SNR(dB) = S - NL = SL - TL - NL \tag{4.6}$$

where all of the quantities under consideration are expressed in dB (see also Appendix B).

To determine the limits beyond which the transmission is no longer reliable, using equation (4.6) we can construct the SNR maps for a determined source level (SL) starting from the knowledge of the transmission loss (TL) at each receiver and the noise level (NL) for the Gulf of Naples. The noise level (NL) was discussed above in section 4.1.3, so we now consider the determination of the source level (SL) and calculate the transmission loss (TL) at the frequency of 100 kHz on the whole grid of 21x12 receivers. The source level is determined according to the relationship (De Dominicis Rotondi, 1990):

$$SL(dB) = 170.5 + 10\log(We) + 10\log(\eta) + DI \tag{4.7}$$

where We represents the electrical power supplied to the antenna, η the electroacoustic efficiency, and DI the directivity index. Considering a realistic example where the transmitter has an efficiency of 50% and the current supplied to the antenna is 185 mA with a tension of 3.24 V, thus giving it an electrical power of 0.6 W, from equation (4.7) the source level will be $SL = 165$ dB. The transmission loss undergone by the signal at any specific receiver are obtained instead from the ratio between the mean intensity I of the signal simulated at each receiver and the mean intensity I_0 of the signal simulated at one meter distance from the transmitter, giving the value in dB according to the relationship:

$$TL(dB) = -10\log\left(\frac{\langle I\rangle}{\langle I_0\rangle}\right) \tag{4.8}$$

which, taking into account equation (4.5), becomes:

$$TL(dB) = -10\log\left(\frac{\langle \mathbf{v}^2\rangle}{\langle \mathbf{v}_0^2\rangle}\right) = -10\log\left(\frac{\langle v_x^2 + v_y^2 + v_z^2\rangle}{\langle v_{0x}^2 + v_{0y}^2 + v_{0z}^2\rangle}\right) \tag{4.9}$$

Using equation (4.9), it is therefore possible to calculate for each receiver the transmission loss knowing the mean value of the particle displacement velocity $\mathbf{v} = (v_x, v_y, v_z)$. The mean value is calculated across a period of time equal to the duration of the signal sent by the transmitter.

4.3 Calculation of the SNR in the Gulf of Naples at 100 kHz

Using equation (4.6) we have constructed the maps that give the signal-to-noise ratio (SNR) for the summer and winter months, for three different transmitter positions, considering both the multiple reflections and the direct phase only. The calculation is carried

out from the knowledge of the transmission loss in the acoustic communication channel at the frequency of 100 kHz, and from the knowledge of the noise level in the Gulf of Naples, and considering a standard digital data transmission apparatus with a source level of 165 dB. The data transmission apparatus considers an omnidirectional transmitter that delivers sinusoidal acoustic signals for the transmission of a digital binary sequence, with a velocity of 2.4 kbit/s at a dominant frequency of 100 kHz, in an operative band of 10 kHz. The power delivered to the antenna was assumed to be 0.4 W with an electroacoustic efficiency of 50%.

From the Shannon's Capacity Theorem for a communication channel (Shannon, 1948) it is possible to calculate (see Appendix B.3) that the signal-to-noise ratio must be greater than 22 dB for reliable information transmission.

Figures 4.8, 4.9, and 4.10 indicate in black the regions in the section of water in which the communication is not reliable, as in those zones of the channel in which the signal-to-noise ratio is less than 22 dB. Where the transmission should be reliable ($SNR > 22$ dB) a different colour has been assigned to each SNR value calculated, in decreasing order from red to violet.

Figure 4.8 shows the signal-to-noise ratio for a transmitter positioned at 1 m in depth. A comparison between the summer and winter maps relative to the direct phase only shows that if the source is positioned at a low depth, the effect of the negative velocity gradient that is seen in summer does not favour surface communication for increasing distances. If, however, a comparison is made between the summer and winter maps that take into account multiple reflections between the surface and the bottom, we see that the multipath effect predominates over the velocity gradient effect. Figures 4.9 and 4.10 show the signal-to-noise ratio for transmitters positioned at 190 m and 299 m in depth, respectively. From a comparison of the summer and winter maps, relative to the direct phase only, it can be seen that for these source depths the negative velocity gradient of the summer months no longer influences communication.

Comparing Figures 4.8, 4.9, and 4.10 for the cases in which multiple reflections are taken into account, it can be seen that if the source is a long way from the bottom and from the surface of the sea, the communication is less disturbed for up to 1.0 to 1.2 km, because of the less influence of the surfaces that delimit the communication channel. Above this distance, the effects produced by the bottom and the free surfaces are similar, independently of the position of the source. The Vp/Vs ratio does not influence the communication. In fact changing the Vp/Vs ratio in the range illustrated in Table 4.3 we obtain the same results as reported in Figures 4.8, 4.9, and 4.10. Moreover, from these three Figures (4.8, 4.9, and 4.10), it can be seen that the transmission is slightly favoured in the summer period due to a lower noise level from agitation of the sea. It is nevertheless important to bear in mind that on average the difference in the noise levels between the summer and winter months due to the conditions of the sea is only 4 dB in the Gulf of Naples.

Considering also the information of Figure 4.7, we can see that below 50 m depth the mean sound velocity profiles for summer and winter season are similar, so also the SNR is stable during the year for transmitter-receiver connections below this depth.

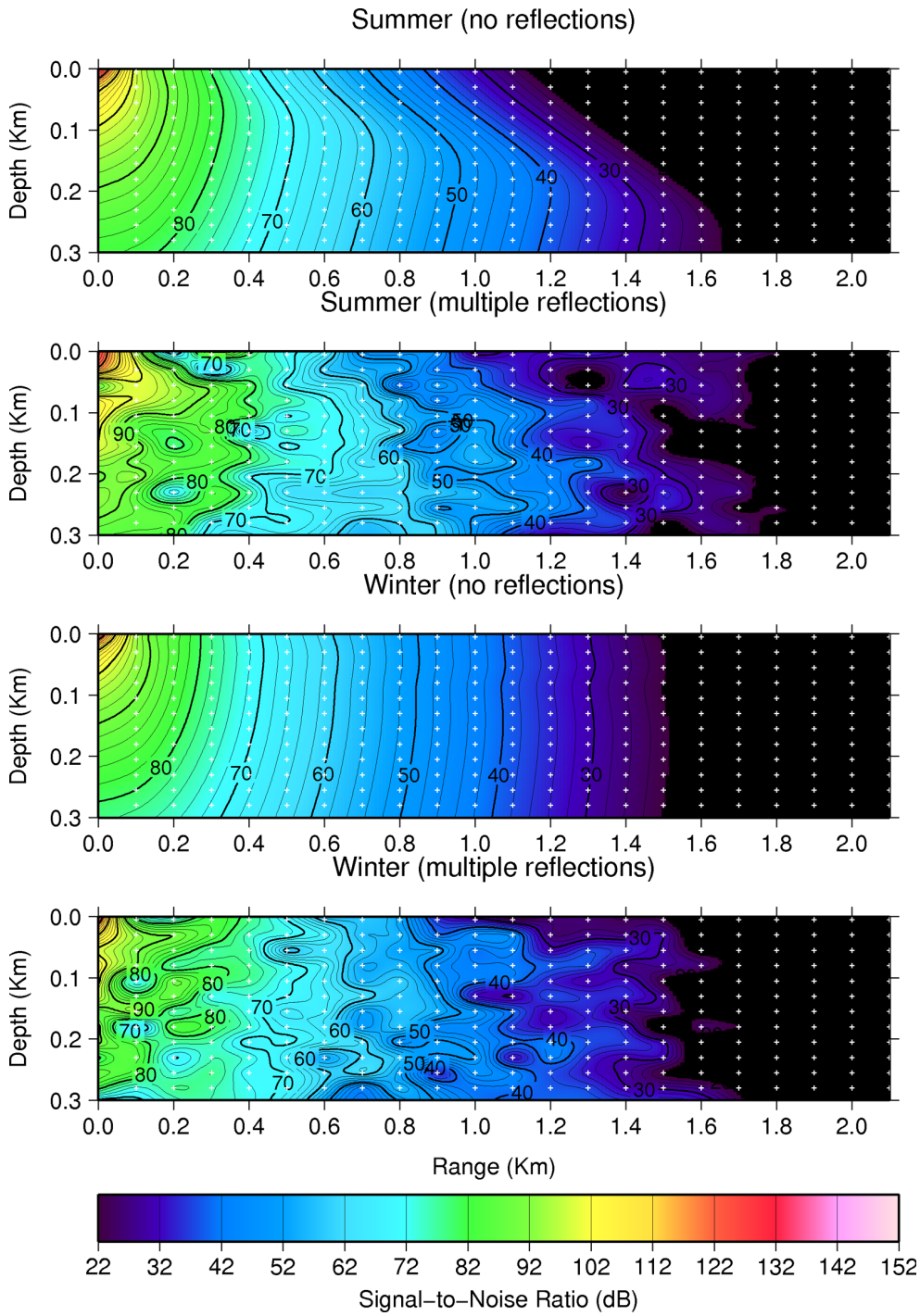

Figure 4.8: *The signal-to-noise ratio for the summer and winter months in the Gulf of Naples with the transmitter positioned at a depth of 1 m. The grid of receivers is plotted with white points. A comparison between the summer and winter maps relative to the direct phase only shows that in summer the effect of the negative velocity gradient does not favour surface communication for increasing distances. Considering also multiple reflections, the multipath effect predominates over the velocity gradient effect.*

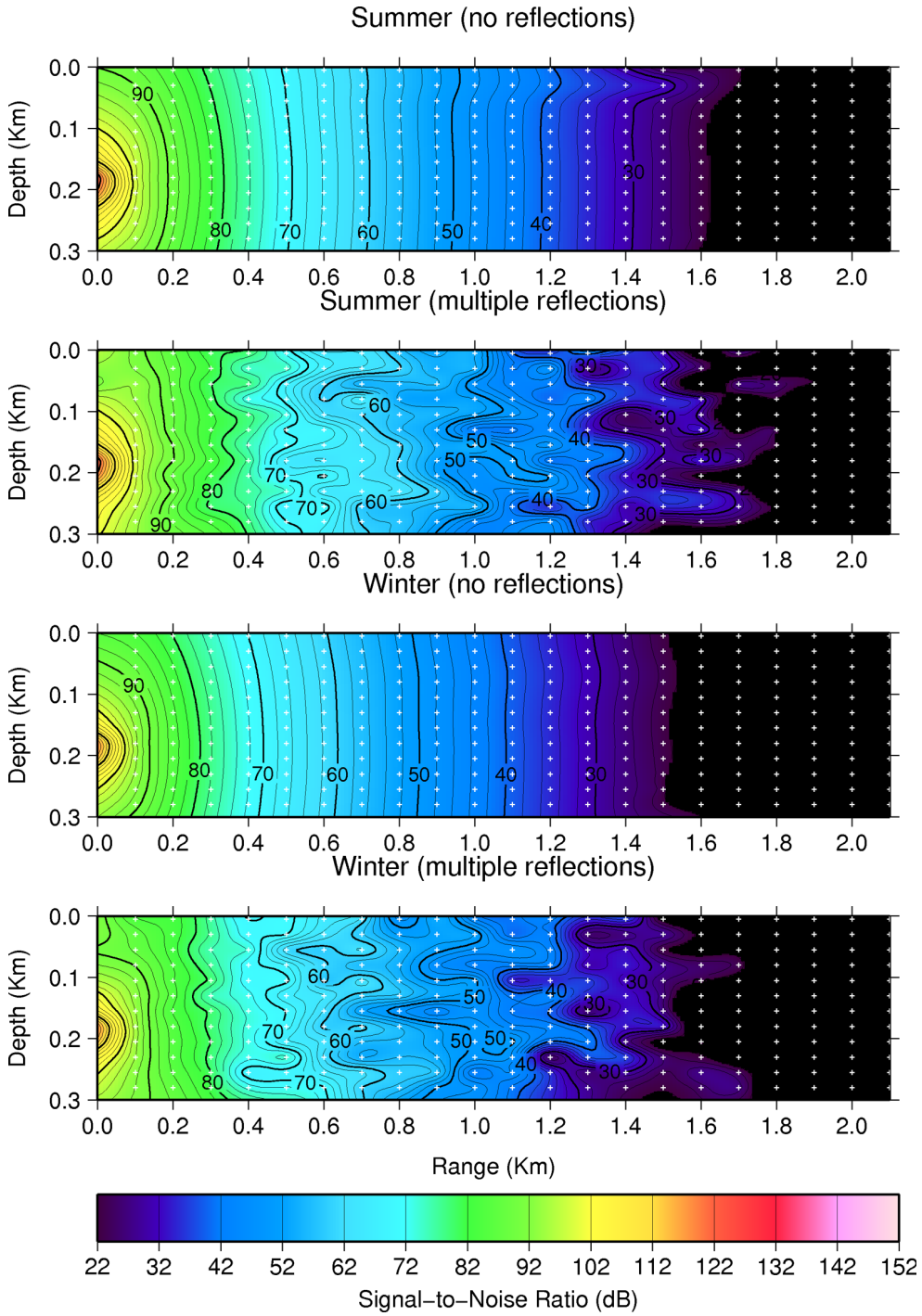

Figure 4.9: *The signal-to-noise ratio for the summer and winter months in the Gulf of Naples with the transmitter positioned at a depth of 190 m. The grid of receivers is plotted with white points. For this source depth the negative velocity gradient of the summer months no longer influences communication; moreover the communication is less disturbed for up to 1.0 to 1.2 km because of the less influence of both the sea and bottom surfaces, since they are far from the source.*

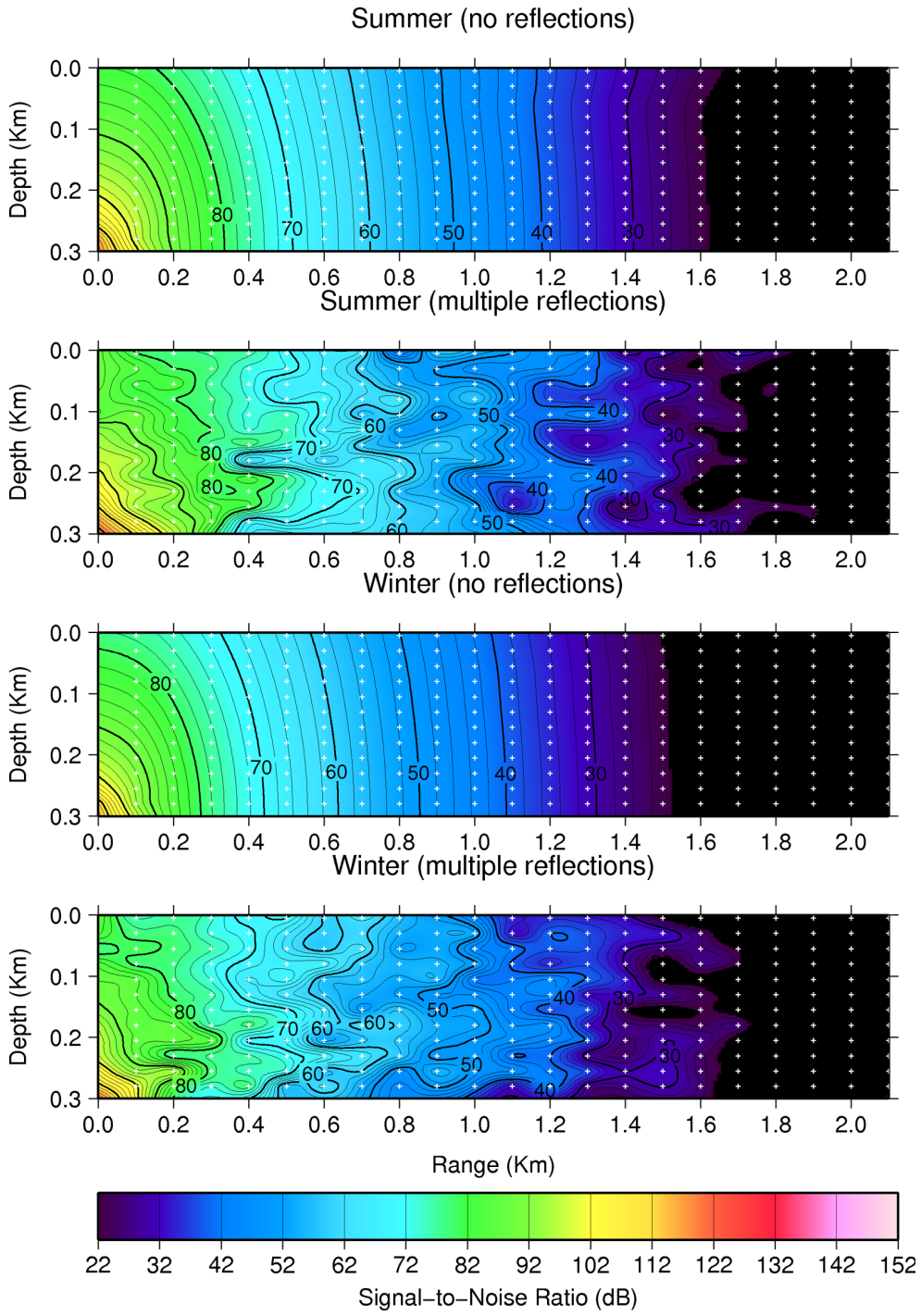

Figure 4.10: *The signal-to-noise ratio for the summer and winter months in the Gulf of Naples with the transmitter positioned at a depth of 299 m. The grid of receivers is plotted with white points. For this source depth the negative velocity gradient of the summer months no longer influences communication, but the influence of the seafloor is magnified.*

Over the reliability of the communication against distance and depth, it is important to bear in mind that the simulated signal at each receiver is perturbed by the multipath effects, arising from the multiple reflections from the surface and the bottom of the sea. Because of this effect, with the transmission of digital data, the coding signals applied to the preceding bit are superimposed on the coding signals of the succeeding bit upon reception, causing an increase in the intersymbol interference (ISI).

Fortunately, acoustic communication has been progressively improving over the course of the years, both in terms of the distances and the data transmission capacity, due to the development of new techniques of signal modulation. In more recent years, the feasibility of the modulation techniques for underwater communication and telemetry has been demonstrated (Catipovic, 1990; Coates, 1993; Stojanovic *et al.*, 1993, 1994, 1995; Stojanovic, 1996, 2005; Hursky *et al.*, 2006), with the minimizing of the ISI with the aim of improving the capacity of the transmission channel.

4.4 Conclusions and discussions

In this Chapter a work carried out by Stabile *et al.* (2007) during this thesis work for the MIUR (Ministry of Education, University and Research) PON-SisMa project is reported.

We have simulated the propagation of sinusoidal acoustic signals sent by an omnidirectional transmitter at the frequency of 100 kHz for the binary sequential digital transmission of information, in a propagation medium with the physical characteristics of the Gulf of Naples. We have used the COMRAD code, described in Chapter 2, to calculate the propagation of the wavefield in the Gulf of Naples. Three different transmitter positions have been considered, at 1 m, 190 m and 299 m (1 m above the bottom) in depth. The reception of the transmitted signal was simulated, for all three cases, by a grid of 21x12 receivers in the sea of 300 m in depth, for a range of 2 km; from the simulation, the SNR maps have been constructed for all of the cases under consideration.

Considering a transmitter with a source level of 165 dB and a velocity of 2.4 kbit/s, for a band pass of 10 kHz, it is seen that the transmission of information is reliable up to distances of 1400-1600 m between source and receiver below 50 m depth and in all seasons of the year, because the mean sound velocity profiles for summer and winter months are similar below this depth. The summer seasonal effects on the sound velocity cannot be overlooked when the transmitter is positioned at the surface or at a low depth. The presence of the sea surface and bottom produce, moreover, important multipath effects that result in errors in the decoding process of the bit sequence of the transmitted information, and particularly if the transmitter is positioned near the surfaces limiting the acoustic channel. Although the sea surface and bottom produce multipath effects, the Vp/Vs ratio of the sedimentary layers does not influence the communication.

If the transmitter is supplied with directionality, the source level can then be increased up to 40 dB, and in this case it is possible to reach a distance of 2000 m while minimizing the multipath effects due to the multiple reflections. Figures 4.8, 4.9, and 4.10 that are relative to the direct phase only give indications as to the SNR that would be present in

the case in which the transmitter is directional; these values must then be increased by the factor of directionality (DI) of the source, which in the case examined here is equal to zero, because it involves a non-directional source.

This study represents a feasibility test of using the acoustic communication to transmit data acquired on the seafloor of the Gulf of Naples. In this region a complex geophysical monitoring system operates for the surveillance of the Neapolitan volcanoes (Mt.Vesuvius and Campi Flegrei caldera). All the instruments are installed in land, while on the seafloor only temporary experiments have been carried out. This study offers a new perspective to the future developments of the monitoring system (such as in Figure 4.11) by the installation of geophysical stations on the seafloor with data transmission by acoustic link to a moored buoy that provides connectivity back to the land by a radio link.

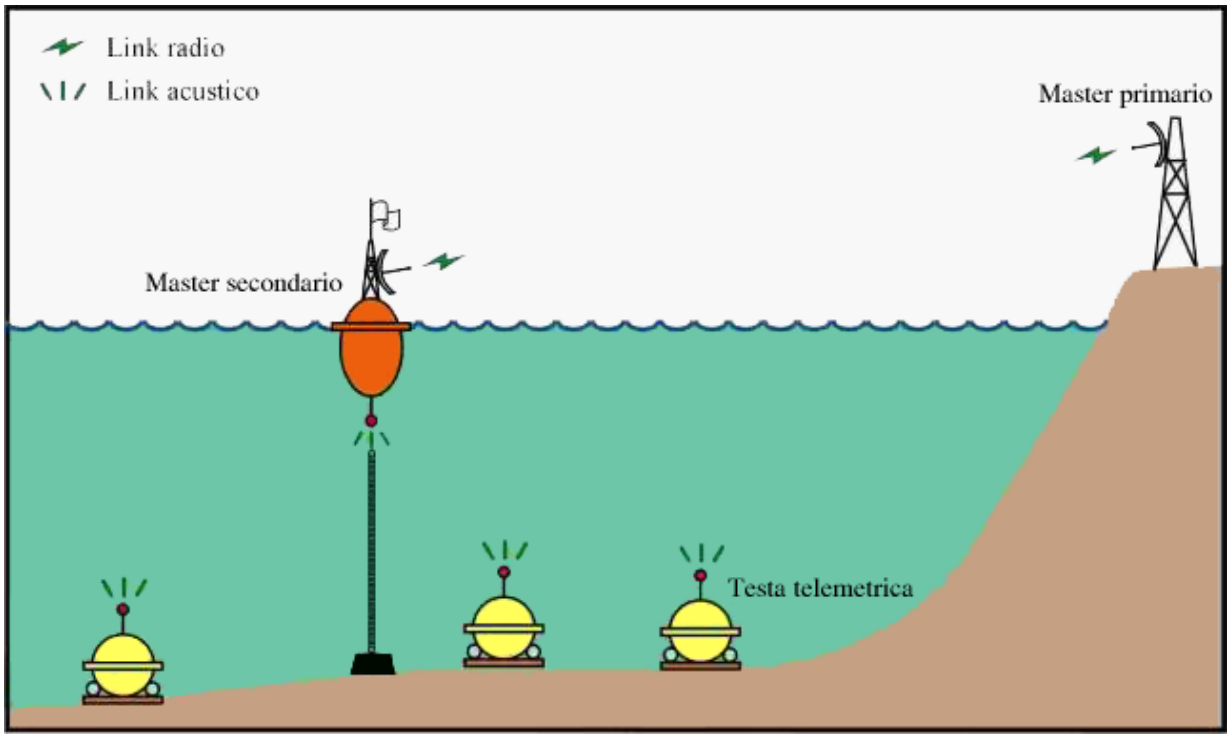

Figure 4.11: *Monitoring system prototype developed during SisMa Project. Geophysical stations installed on the seafloor collect data, which are transmitted to a moored buoy (secondary master) by acoustic link; then a radio communication connects the buoy to the on-land data centre (primary master).*

Chapter 5

Very high frequency Submarine Acoustic Imaging

In the turbid, saline water of the sea, the attenuation of both light and radio waves is orders of magnitude greater than the attenuation of the sound, which is the best form of radiation that travels through the sea. For this reason the acoustic (sound) wave propagation is applied to transmit data through the sea channel or to explore the underwater ambient.

The use of the sound for data transmission in the seawater was discussed in Chapter 4. Here we will apply the underwater acoustic wave propagation to the imaging of submerged objects. This is an on-going work started in the third year of this thesis work and funded on the STSS-500 project that will be described in section 5.1.

Acoustic imaging is nowadays an active and attractive research field, which draws the attention of many companies, organizations, institutes, research groups, and universities in different countries with the aim to study and develop techniques for the processing of signals acquired by acoustic systems in order to reconstruct the image of the insonified medium. The STSS-500 project belongs to this field.

Before describing this work, we want to introduce the concept of passive and active sonar:

- Passive (or listening) sonar systems use sound radiated by the target. Only one-way transmission through the sea is involved, so the system is centred on the hydrophone, which is used to listen to the target sound. These kinds of systems are usually used to the detection and localization of ships, submarines, torpedoes, or everything produces sound in the water.

- Active sonar systems generate the sound by a projector; the sound propagates through the seawater to the target, and comes back as echoes to the hydrophone of the system. These kinds of systems are usually used to reconstruct the image of the target (e.g. submerged objects, sea-bottom topography, ships).

- Hybrid forms of sonar systems use a projector and hydrophone at both ends of the

acoustic communication path. These kinds of systems are employed for communication, telemetry, and control applications.

For each of this type of sonar systems there is an appropriate equation. In Appendix B.1 the different sonar equations will be discussed. A complete treatment on the principles of underwater sound and its applications can be found in Urick (1983).

5.1 The STSS-500 Project

The MIUR (Ministry of Education, University and Research) Pon STSS-500 (from the Italian: "Sonar Tridimensionale Stereoscopico Simultaneo a 500 kHz") project is an ongoing project whose aim is to research and to study the technologies and the processes that can be applied to the sonar imaging field, in order to build a prototype of underwater acoustic camera.

Although underwater optical vision provides images with finer resolution respect to the acoustical one, as we said before its range is limited to a few meters, in particular in turbid water. Using very high frequencies acoustic signals from about one kilohertz to few megahertz the resolution of acoustic imaging systems can become fine too.

Using antennas composed by high-technology electroacoustic transducers, the prototype of acoustic camera can be able to reconstruct the image of submerged objects in the seawater, in particular for turbid water conditions. The implementation of this system can be used to the remote management of several activities in the seawater (e.g., monitoring and surveillance of maritime activities, monitoring industrial pollution along coast and offshore, detection of archaeological objects in the sub-bottom, exploration of the seabed).

The main characteristics of the image produced by the acoustic camera will be:

- complete image of the target
- three-dimensional image
- stereoscopic effect of the image

This is an innovative imaging instrument, since commonly the 3D image is actually produced by moving the system along a specific trajectory, and stereoscopy is not taken into account yet.

The prototype of acoustic camera belongs to the class of active sonar, since the system will be composed by a projector and a receiver apparatus. The projector generates sound in the frequency band between 400 kHz and 600 kHz with a central frequency of 500 kHz, a frequency that can guarantee both a high resolution of the image and a good visibility range. The receiver apparatus is composed by an array of 128 receivers electrically and mechanically insulated (diced[1] array). The maximum planned distance for the detection of the target is about 50 m.

The most important expected results for the research in this field are:

[1]The diced technology consists in a method able to produce transducers by dividing a ceramic block into small separated little blocks insulated each to other.

- to study the materials properties in order to find the most appropriate materials for this kind of array and these high frequencies
- to choose the best technological configuration of the system that gives a 3-D stereoscopic image of the target
- to simulate the behaviour of the chosen configuration both respect to the material response and respect to the physical parameters of the surrounding underwater environment.
- to optimize the transducer parameters (e.g. resolution, performance).

The partners of this project are the WASS[2] industry of Monterusciello (Pozzuoli, Naples), the University of Naples[3] Federico II, and the ENEA[4] research institute.

5.2 Development of an Acoustic Imaging Numerical Simulator

Our role in this project is to study the high frequency propagation of the sound in seawater, from the generation of the sound by the projector to the recording of the echoes from submerged objects in the seawater by the array of receivers, taking into account the influence of the environment parameters on the sound propagation.

Another important aspect we are interested is the processing of the backscattered echoes in order to create an image of the insonified scene.

For these reasons, our work has been implemented in a program which simulates the propagation of the sound in the seawater with modelled objects inside (forward modelling) and reconstructs the image of the target (imaging) from its echoes using beamforming techniques. This simulator is of crucial importance since it can be used for the choice of the best configuration of the acoustic camera system.

Additional tools are included in the numerical simulator in order to improve interactivity with the user. It is possible to create plane and solid objects (as rectangles, circles, spheres, parallelepipeds) that can be used to model simple targets, and import ASCII files describing the shape of both the target and the acquisition system (i.e. the source-receiver geometry) in 3-D. The object can be translated along each direction and can be rotated in the three-dimensional space around each axis using the matrix

$$\begin{pmatrix} 1 & 0 & 0 \\ 0 & \cos\theta & -\sin\theta \\ 0 & \sin\theta & \cos\theta \end{pmatrix} \tag{5.1}$$

[2]Whitehead Alenia Sistemi Subacquei.

[3]Dipartimento di Scienze Fisiche dell'Università degli Studi di Napoli Federico II.

[4]Ente per le Nuove tecnologie, l'Energia e l'Ambiente; offices in Brindisi, Casaccia (Rome), and Frascati (Rome).

with θ the rotation angle (anti-clockwise). The synthetic data provided by the forward modelling part of the simulator can be given in the standard SeismicUnix format (Cohen and Stockwell, 2007). The output of the imaging part of the simulator can be an ASCII file or plots in postscript format along horizontal planes of fixed values of z. Postscript plots of the acquisition geometry should be also provided.

Following we explain in details both the forward modelling and the imaging part of the numerical simulator.

5.2.1 Forward modelling: Rayleigh scattering

The sea contains inhomogeneities of many different kinds both within itself and on its boundaries. These inhomogeneities form discontinuities in the physical properties of the medium reradiate the incident wave into all directions whenever their dimension results comparable or much smaller than the characteristic wavelength of the incident wavefield.

This reradiation of energy is called scattering, and the superposition of the scattering contributions from all scatterers is called reverberation.

In the sea there are three different classes of reverberation:

1. *Volume reverberation*, which occurs when the waves are scattered by matter distributed inside the seawater (e.g. marine life, suspended inanimate materials);

2. *Sea-surface reverberation*, which is produced by scatterers located near or on the sea surface;

3. *Bottom reverberation*, which is produced by scatterers located near or on the sea bottom.

Both the sea-surface and the bottom reverberation may be analytically considered as surface reverberation.

The forward modelling in acoustics has as objective the computation of the scattered pressure field for given incident acoustic waves and the physical properties of the object. Studies of forward scattering problems have been reported in a large number of publications, and both exact analytical solutions[5] and approximate methods have been developed (Liu *et al.*, 2003).

The forward modelling part of the numerical simulator developed in this study is more general, since it considers both the acoustic and the elastic cases. The forward modelling is actually based on single scattering from a spatial distribution of scatterers inside a homogeneous medium. The scatterers are considered as spheres with a diameter $2a$ such that $2ka \ll 1$, with $k = 2\pi/\lambda$ the wavenumber relative to the dominant wavelength λ of the incident wave. The contrast between the material parameters of the scatterers and those of the surrounding medium can be arbitrary. In this situation the Rayleigh approximation,

[5]The exact analytic solutions can be derived only when the technique of separation of variables can be used, such as objects like spheres, spheroids, and cylinders. For objects having more general shape, approximate methods must be used.

explained in section 1.4, can be used in order to compute the amplitude of the scattered waves.

In the case of objects having large dimensions respect to the dominant wavelength λ of the incident wave, they are modelled with a large number of this kind of little spheres. The scattered wavefield is hence a superposition of single scattering produced by each sphere. This allows the modelling of objects with arbitrary shape (thus objects having corners, rough surfaces, thin components).

In summary the following quantities have to be given in input:

1. The physical properties of the background homogeneous medium that contains the scatterers, such as the P-wave velocity Vp_0, the S-wave velocity Vs_0, and the density ρ_0.

2. The position of the i^{th} source $S_i = (x_i, y_i, z_i)$, with $i = 1, \cdots, M$, and M the total number of the sources.

3. The position of the j^{th} receiver $R_j = (x_j, y_j, z_j)$, with $j = 1, \cdots, N$, and N the total number of the receivers.

4. The position of the k^{th} scatterer $P_k = (x_k, y_k, z_k)$ and its physical properties (P-wave velocity Vp_k, S-wave velocity Vs_k, density ρ_k), with $k = 1, \cdots, L$, and L the total number of the scatterers.

5. The waveform and the duration of the signal emitted by the source.

Moreover, it is possible to compute P-P and/or P-S scattering (equations 1.42) and to project (or not) the scattering response onto one of the two horizontal (X or Y) components or onto the vertical (Z) component.

In the case of underwater acoustic propagation only P-P scattering can be computed, since no S-waves propagates inside the water, and the following background parameters can be used

$$Vp_0 = 1500 \text{ m/s}; \qquad Vs_0 \approx 0 \text{ m/s}; \qquad Vp_0 = 1500 \text{ kg/m}^3$$

where $Vs_0 \approx 0$ m/s means a very little[6] value for S waves.

The numerical simulator computes also the geometrical spreading of the wavefield and, in the case of underwater acoustic propagation, the attenuation for absorption α is taken into account by using the empirical equation (B.6) described in Appendix B. The two effects in underwater acoustic can be tied together giving the following expression for the total attenuation A in decibels per kilometre (Stojanovic, 2006):

$$A(\text{dB/km}) = k \cdot 10 \log r + r \cdot \alpha \tag{5.2}$$

[6]It is well known that the S-wave velocity must be equal to zero in fluids, but in the program the S-wave velocity must be set to a little value in order to avoid computational problems due to the division by zero (see section 1.4).

with r the range and k the spreading factor, which describes the geometry of propagation. The commonly used values for the spreading factor are $k = 2$ for spherical spreading, $k = 1$ for cylindrical spreading, and $k = 1.5$ for the so-called practical spreading.

The spherical spreading occurs when the power generated by the source is radiated equally in all directions, so it is equally distributed over the surface of a sphere surrounding the source having radius equal to the range r. The cylindrical spreading occurs when the medium is bounded by two plane-parallel surfaces, so beyond certain distances the power radiated by the source is equally distributed over the surface of a cylinder having radius equal to the range r and height equal to the distance h between the two surfaces. Finally, the practical spreading is used in the case of hybrid (one half spherical and one half cylindrical) spreading.

Figure 5.1 shows curves of the total sound attenuation A in seawater against range and frequency, considering a spherical spreading and the physical parameters of the Gulf of Naples[7]. The range is from 0 km to 1 km, and the plots are for 10 kHz, 100 kHz, 500 kHz, and 1 MHz of frequency, respectively.

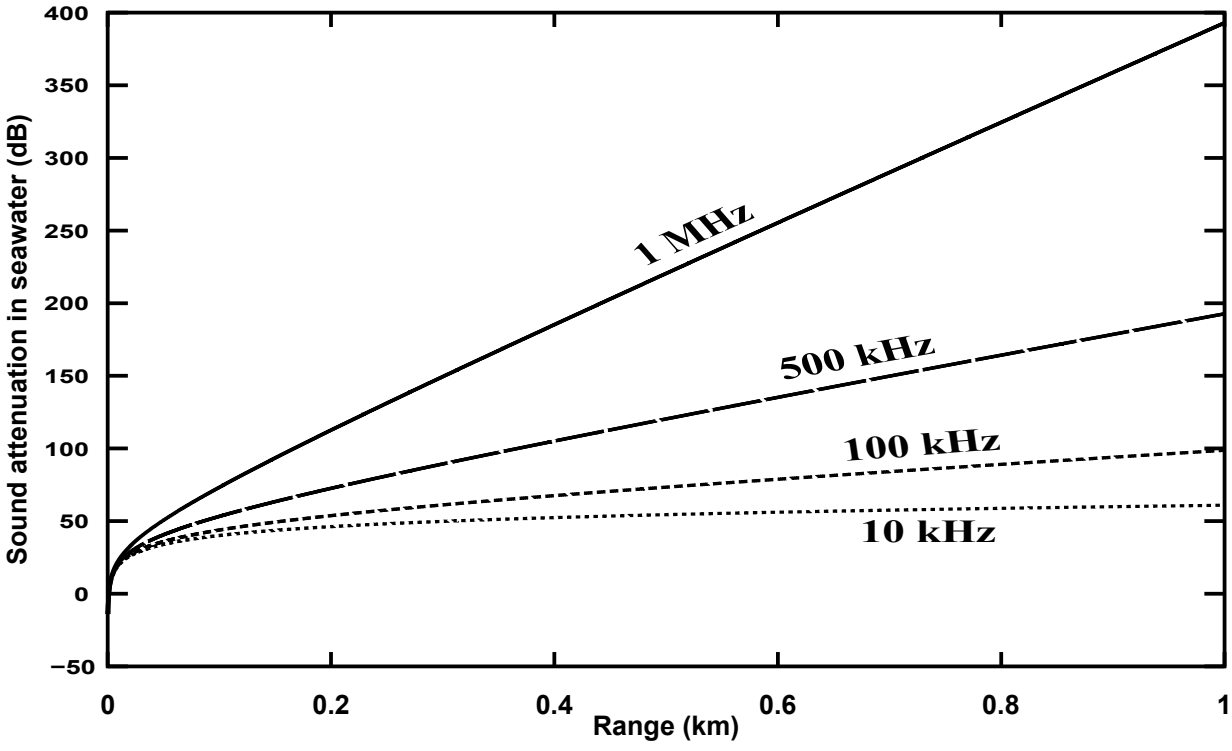

Figure 5.1: *Sound attenuation in seawater against range and frequency, and considering a spherical spreading. Plots relative to frequencies of 10 kHz, 100 kHz, 500 kHz, and 1 MHz are reported, respectively.*

[7]Typical values of physical parameter of the Gulf of Naples are: salinity of 38.5 ppm, pH of 8.1, water temperature of 14.2 °C, depth of 200 metres, and sound velocity of 1512 m/s.

5.2.2 Imaging: Beamforming techniques

When a signal is recorded by a receiver it is possible to see in its waveform many phases that differ each to other both in amplitude and in shape. The main phases of a seismogram or, in general, of a recorded signal are not always of interest. The identification of weak phases such as reflections, convertions, or scattered waves from the discontinuities inside the medium plays an important role. The identification of these weak phases usually requires good-quality registrations and a good coverage of the area under investigation by stations.

Thus having a large number of traces, the weak phases can be detected by their coherent appearance on different traces. A classical method is the stack, where the traces are summed along assumed traveltime curves. If the traveltime curve is correct, the signal is summed coherently while the noise amplitude decreases as a consequence of his incoherency. Various techniques (Yilmaz, 2001) have been developed for extracting information from the observed wave field either in time or in frequency domain in order to detect coherent signals. Moreover, different processing and migration techniques applicable to marine and vertical-seismic-profiling acquisition geometries have been discussed by Müller (2000).

A class of imaging methods is the beamforming, which is a signal processing technique used with arrays of receivers. It involves combining or sum delayed signals from each receiver at slightly different times, so that the signals will be aligned at exactly the same time and produce a strong signal as it would come from a very sensitive receiver. When beamforming is used on both the source and the receiver array side simultaneously, the technique is called the "double-beam method" (Krüger *et al.*, 1996; Scherbaum *et al.*, 1997).

The imaging part of the numerical simulator developed in this study considers the same imaging technique applied by Maercklin *et al.* (2004) to image the Dead Sea Transform with scattered seismic waves. This is a beamforming technique that can be used for both the elastic and the acoustic case.

Figure 5.2 on the next page will help us to explain the method. We consider a medium with an inhomogeneity (a scatterer) in its interior and one source with and array of receivers on the free-surface (Figure 5.2, on the left). The energy excited by the source travels through the medium and is thus recorded by the receivers. The first arrival is the direct P wave, and a second arrival (labelled PxP) is due to scattering from the inhomogeneity.

The first panel of traces in Figure 5.2 shows the result of the forward modelling for this case, with a P arrival around 3.6 s and PxP around 4.3 s.

Direct P traveltimes can be applied to these traces as static shifts to align the first onset. This yields the second panel in Figure 5.2, labelled P. For the second arrival, the PxP wave, we consider in the medium a grid of possible scattering point. For each possible scatterer of the grid and for each receiver we compute the traveltime from the source to the scatterer and from the scatterer to the corresponding receiver. Applying these moveout times as shifts to the initial recordings aligns the the PxP phase as shown in the right panel in figure 5.2.

As we said before, generally real data are contaminated with noise. Thus weak phases

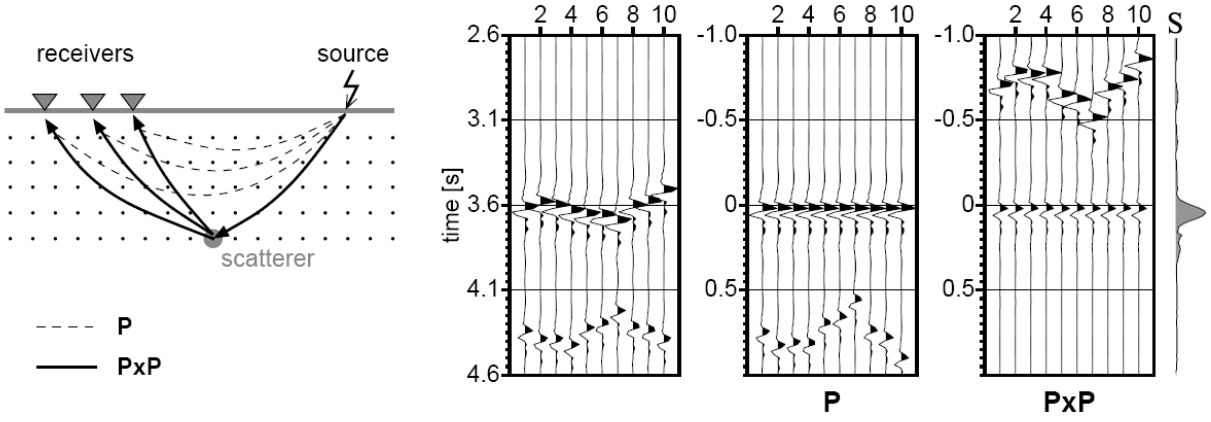

Figure 5.2: *Scheme of the beamforming technique used for the imaging process. The semblance S is maximum in correspondence of coherent phases (P and PxP panels). The figure was modified from Maercklin (2004).*

like PxP have often small amplitudes compared to the P-wave. In these cases the use of coherency measures are preferable to a simple stack of the traces. We have used in this work the semblance S as a coherence measure, but other measures such as the phase-weighted stack (Schimmel and Paulssen, 1997) could be used. The coherency is measured in a time window centred at the predicted arrival time (0 s in Figure 5.2).

The semblance S is defined to be the normalized output/input energy ratio, where the output trace is a simple compositing or sum of the input traces. In mathematical terms it is given by:

$$S = \frac{\sum_{j=k-(N/2)}^{k+(N/2)} \left(\sum_{i=1}^{M} f_{i,j} \right)^2}{M \sum_{j=k-(N/2)}^{k+(N/2)} \sum_{i=1}^{M} f_{i,j}^2} \tag{5.3}$$

in which M aligned traces are analysed in a time window of N samples centred at sample k.

From equation (5.3) we can see that $0 \leq S \leq 1$, where 0 means complete incoherency and 1 perfect agreement between traces, respectively. A high semblance value observed for PxP aligned traces indicates the presence of a scatterer at the corresponding grid point, as shown on the left of Figure 5.2. Thus, we can assign for each value of the semblance a probability meaning: the higher the value is the higher the probability to find in that point the scatterer will be.

Scanning the entire volume, it is possible to reconstruct an image of the medium that localizes scatterers by the use of high values of semblance.

The following quantities have to be given in input to the imaging part of the numerical simulator:

1. The physical properties of the background medium that contains the scatterers, such as the P-wave velocity Vp_0, the S-wave velocity Vs_0, and the density ρ_0. These are

taken automatically from the forward modelling part of the numerical simulator

2. The length of the time window, in which the coherency measure of traces using semblance will be computed.

3. The definition of the image volume. Thus, we have to define the coordinates of the bottom-left point $(x_{min}, y_{min}, z_{min})$ of the grid, the number of points along the X direction (nx), Y direction (ny), and Z direction (nz), and the sampling rates $(dx$, dy, and $dz)$ along these three directions, respectively. One notes that the construction of the grid is more general, since it is possible to sample the medium differently along the three directions.

The output of the imaging process is a 4-column file containing the grid points coordinates (first three columns) and the semblance value (4^{th} column), respectively.

5.3 Three-dimensional imaging of submerged objects

In this section some examples on 3-D imaging using the numerical simulator described in the previous section will be reported.

The first example considers the case of 4 balls in a deep ocean, having a diameter of 1 m and coordinates $B_1 = (3, 4, -1)$ km, $B_2 = (3, 3, -1)$ km, $B_3 = (4, 4, -1)$ km, $B_4 = (4, 3, -1)$ km. We suppose we want to perform a localization of these balls using a system composed by one source and 50 receivers. The system is placed on the sea-surface. Figure 5.3 shows the position of both the system (source+receivers) and the scatterers from two different views (lateral and top). To avoid a strong attenuation we consider a

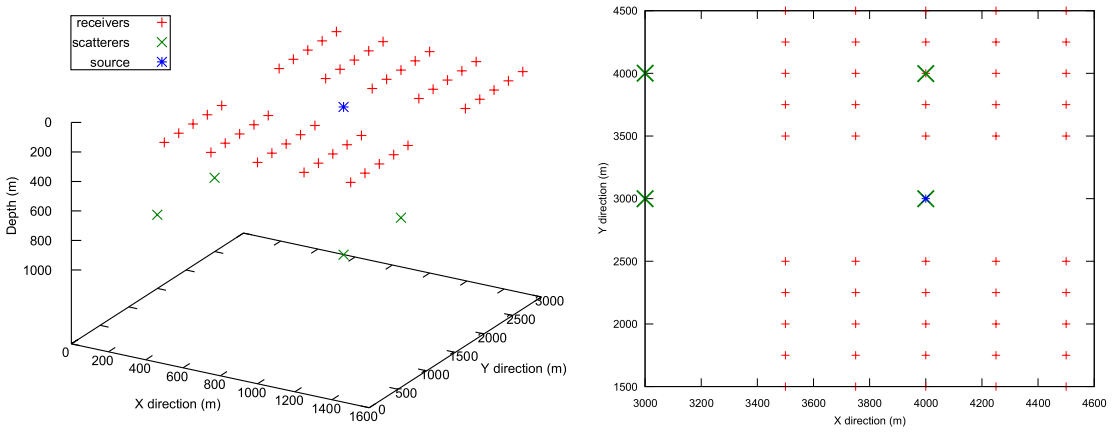

Figure 5.3: *Source-receiver geometry used to perform a localization of the four scatterers. (Left) Positions of the source, the receivers, and the scatterers from a lateral view. (Right) Projection of scatterers onto the source-receivers plane. The source, the receivers and the scatterers are plotted using $*$, $+$, and $\times$ symbols, respectively.*

Gaussian source having a dominant frequency f of 20 Hz. These balls satisfies the Rayleigh condition $ka \ll 1$, so Rayleigh scattering occurs. In fact we have:

$$ka = \frac{2\pi a}{\lambda} = \frac{2\pi a f}{c} = 0.08 \ll 1 \tag{5.4}$$

where $c = 1500$ m/s is the sound velocity in seawater.

The echoes recorded by the receivers are reported in figure 5.4 (left side). The traces are ordered by offset. In the same figure (right side) the image of the scatterers on the plane $z = 1$ km in depth (where the four scatterers are) is reported. Two different sampling rate of 20 m and 200 m are used to define the same image volume. For both the choices the imaging process found the scatterers in their exact position, but the resolution becomes

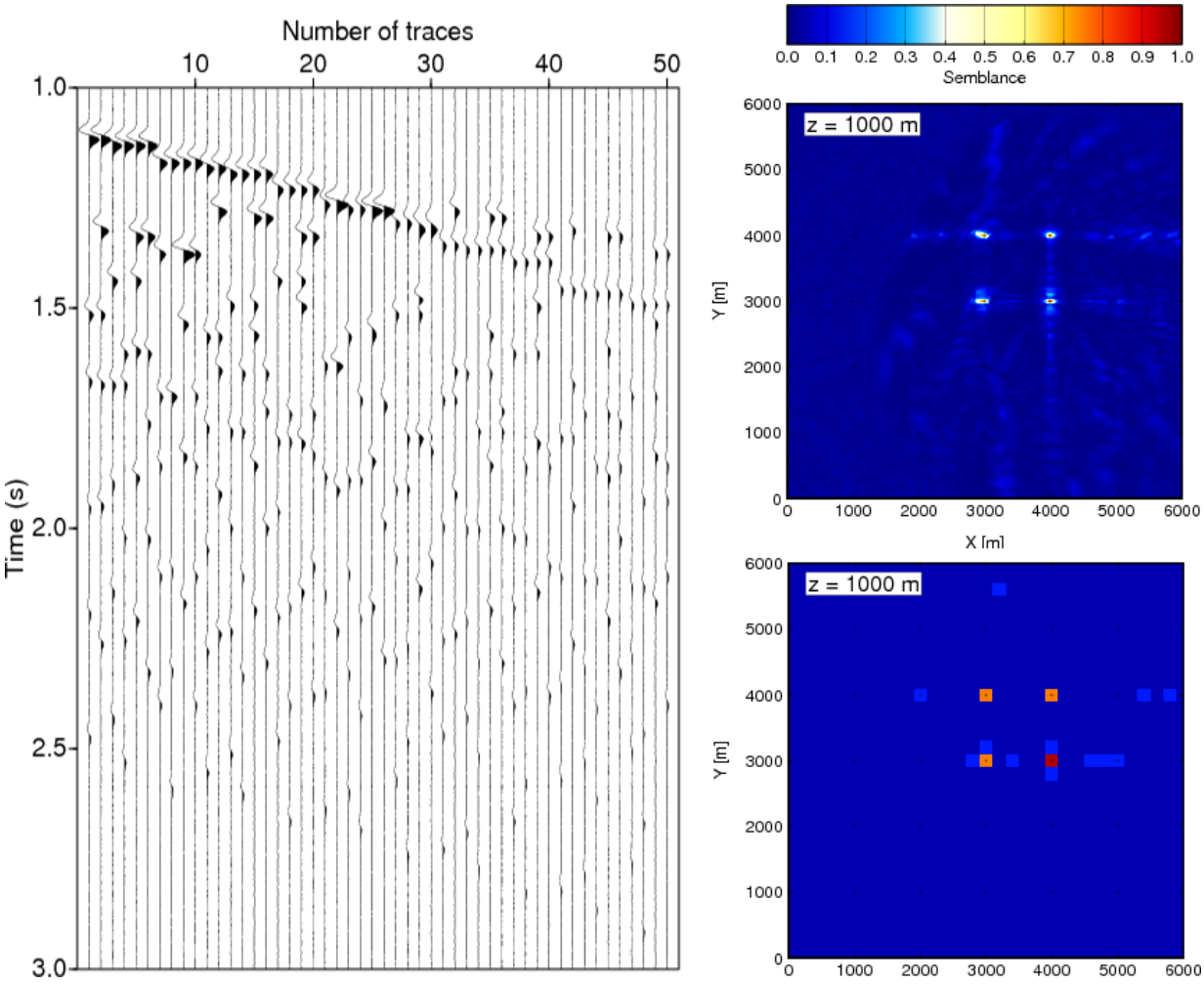

Figure 5.4: *(Left) Synthetic data, ordered by offset, obtained for the model of Figure 5.3. (Top-right) Image of the four scatterers, defining the image volume by a sampling rate of* 20 *m. (Bottom-right) The same image but using a sampling rate of* 200 *m.*

better for smaller sampling rates (top right of Figure 5.4). In particular, the scatterers are localized by the use of semblance values, reported in Figure 5.4 in different colours from blue to red. Blue colour indicates a low semblance value, while red colour indicates a high semblance value that is a high probability to find a scatterer in that point.

The second example considers the case of a granite block submerged in the seawater. The block is a cube having dimension of 50x50x50 cm. Table 5.1 shows the physical properties of the background medium and the cubic block used to compute synthetic data for the case under consideration. One notes that there is a strong contrast between the

Type	Material	Vp (m/s)	Vs (m/s)	Density (kg/m^3)
Background	Water	1500	0.0001	1000
Cubic block	Granite	4500	2600	3000

Table 5.1: *Physical properties of the cubic block and the background medium used for the forward modelling in the second example. The cubic block has dimension of 50x50x50 cm and is made of granite. The background medium is the water.*

cubic block and the surrounding water. The block is considered with water inside and its surfaces (made of granite) are modelled by 15000 spherical scattering points (with a sampling rate of 1 cm) having the physical properties of Table 5.1. We insonify the block by a system having one projector (a non directional point source) above a grid of receivers (acquisition system). The projector emits a Gaussian signal with a dominant frequency of 100 kHz; the signal scattered by the cubic block is recorded by each receiver, thus the image of the target (i.e. the cubic block) is reconstructed using the beamforming technique described in section 5.2.2.

Two different configurations for the acquisition system have been used. The first is a rectangle of 2x1 m in size, composed by 200 receivers having 0.1 m distance each to other. The second configuration is a more complex system of 245 receivers. In Figure 5.5 both the configurations are shown.

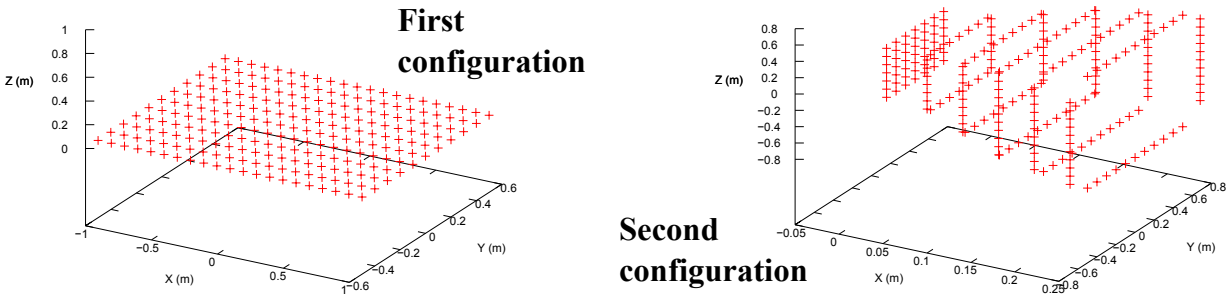

Figure 5.5: *Two different configuration used for the acquisition system. (Left) 200 receivers are arranged on a 1x2 m rectangle. (Right) 245 receivers are arranged in a more complex configuration composed by five not parallel panels.*

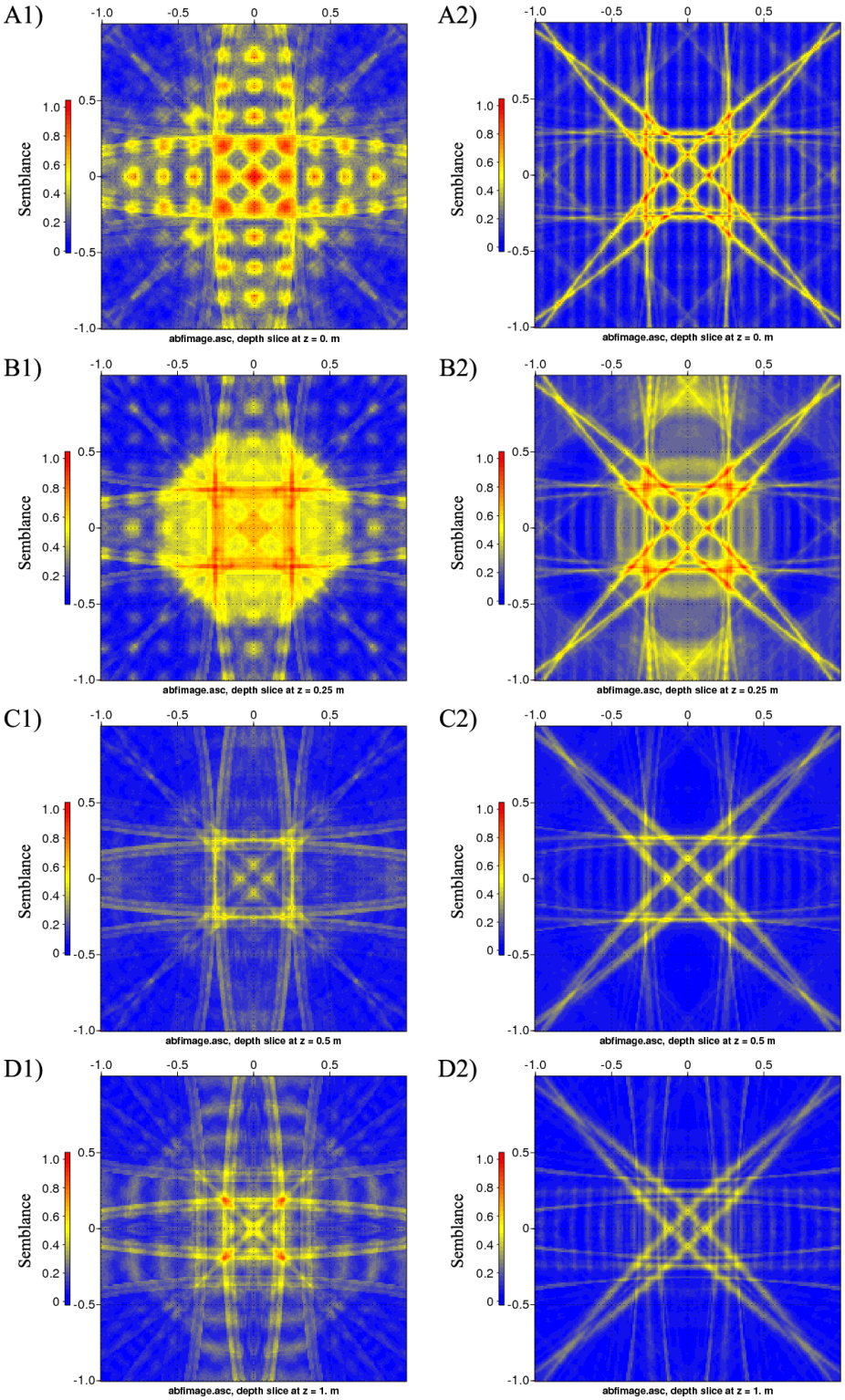

Figure 5.6: *Images of the target in the planes $z = 0$ m, 0.25 m, 0.5 m and 1 m, respectively, obtained using the second configuration of Figure 5.5 (left slices) or the first configuration of Figure 5.5 (right slices).*

We suppose the projector-receivers system to be rigid. This system can rotate around the cubic block at a fixed distance (5 metres) from the centre of the block, which is considered the origin of the axes. Images of the block at different planes $z = const$ as functions of semblance values are reported in Figure 5.6. Here again blue colour indicates a small value of semblance, while red colour indicates a high semblance value. The image volume, that is the grid of points where the semblance is computed, has been built using the following sampling rates along X, Y, and Z direction respectively: $dx = 0.01$ m, $dy = 0.01$ m, and $dz = 0.25$ m.

As shown in Figure 5.6, the second configuration of Figure 5.5 gives high resolution images (slices A1, B1, C1, D1) respect to those obtained by the first simple configuration (slices A2, B2, C2, D2). Moreover, the corners of the block are well evidenced and the correct dimension of the target is obtained from the imaging process. Unfortunately as shown in the slices C1-C2 and D1-D2 on the bottom of Figure 5.6, fuzziness in the image of the object still remains.

Using the second configuration of Figure 5.5, we have also reconstructed a 3-D image of the cubic block by eliminating in the plot all the points P of the image volume that have the corresponding semblance value S less than 0.9, hence the condition imposed is:

$$\text{The point } P \text{ is plotted if} \Rightarrow S(P) \geq 0.9 \tag{5.5}$$

Figure 5.7 shows a comparison between the real image of the cubic block (left side) and the image obtained by the system under consideration (right side).

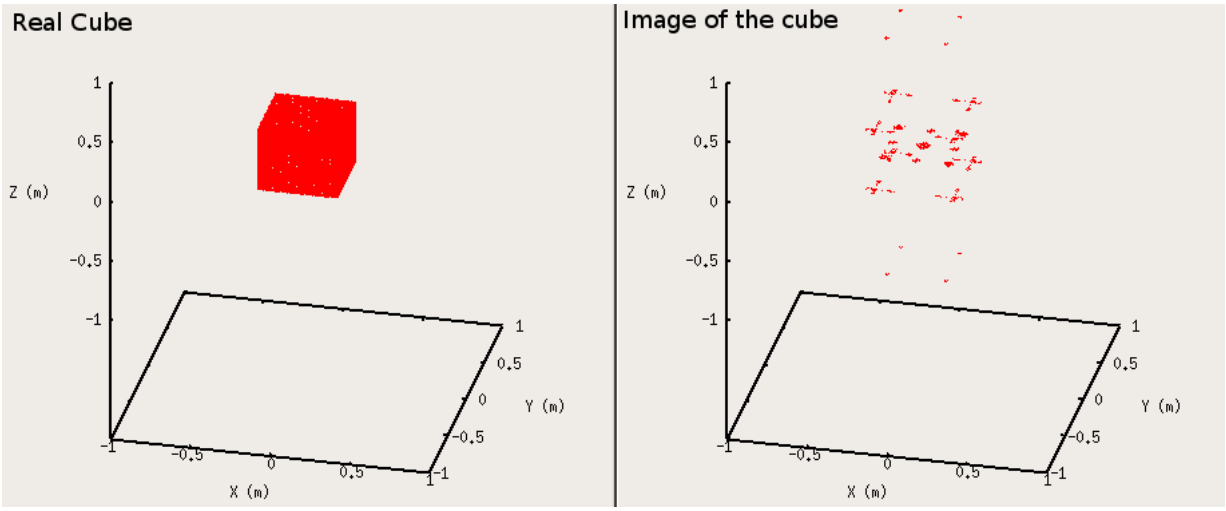

Figure 5.7: *(Left) Real shape of the block and (right) its image obtained using the second configuration of Figure 5.5 and taking into account the condition (5.5).*

5.4 Conclusions and discussions

In this Chapter we have discussed the detection and imaging of objects submerged in the seawater with very high frequency acoustic signals. We have used the scattered theory with the Rayleigh approximation that is valid when the scatterer is much smaller than the dominant frequency of the incident wave. The amplitudes are computed for such a scatterer with spherical shape. Large objects have been modelled as a sum of these little scatterers, each of them contributes to the total scattered field.

We have developed and tested (by the use of synthetic examples) a numerical simulator in order to reproduce the entire process from the generation of the signal to the processing of echoes by the target. Images of the insonified environment have been reproduced.

The numerical simulator will be a useful tool in the development of a 3-D stereoscopic underwater acoustic camera, which is the final product of the STSS-500 project described above. In fact, the simulator can be used both to reproduce synthetic data for the acquisition system and to help the engineers to the development of the system apparatus configuration (shape of projectors and antennas, distances, directivities).

In section 5.3 we have shown some imaging examples until 100 kHz. We have demonstrated that a simple improvement of the receivers' geometry (i.e. the acquisition system) provides a better resolution of the object insonified. Further improvements of the acquisition system will give better images, reducing fuzziness and improving resolution. Moreover, stereoscopy will be taking into account by the use of two of such a system (as we do with two eyes).

Due to problems on the maximum length of traces (65536 samples) in Seismic Unix format (Cohen and Stockwell, 2007), the imaging with 500 kHz signals actually can be carried out only for very short distances because, to avoid aliasing, the sampling rate must be almost 1 mus. We are working both in the direction to extend the trace length and in cutting the portion of the trace that does not contains information.

In the future we will consider also the effect of the medium (especially sedimentary layers) on the image reconstruction as it may improve or disorganize the image coherence. There will be an evaluation of the accuracy on velocity variations in the sedimentary medium for such reconstruction as well as the defocusing effect of a smooth velocity variation in the water column coming from currents modifying the temperature gradient.

Conclusions

In this thesis work we have studied the high-frequency seismic and underwater acoustic wave propagation in complex media. Moreover, imaging techniques are applied in different research field, from the exploration geophysics to the acoustic imaging.

A method for rapid high-frequency seismogram computation has been presented in this thesis. The most important features of this method are summarized as follows:

1. Short computing time that does not depend on the frequency, since the method is based on ray theory.

2. Each phase on the synthetic seismogram is associated at a known body wave, that is both the travel-time, the raypath, and the amplitude of each wave is computed and it is possible to isolate all the phase each to other.

3. Automatic definition of an exhaustive set of reflected/transmitted/converted body waves in a short time (about one second). This is based on the hierarchic generation of strings that describe the ray paths and the phase types to be computed.

4. Constraints on the wavefield propagation can be set in order to reduce (or not) the number of phases. More complex synthetic seismograms requires longer computing time since thousands amplitudes, travel-time and ray-paths have to be computed; simpler synthetic seismograms, including only the direct waves and few reflections, require only few seconds to be computed.

5. Easy implementation with other ray-theory programs, since the criterion used to define the body waves to be computed is almost the same for all of them.

Some work is carried out also to correlate the computing time to the complexity of the synthetics, as function of the values chosen for the constraint parameters. An important series of quantitative tests has been used to validate the method. In particular in this text we have described a quantitative comparison, according to a time-frequency misfit criteria based on the continuous wavelet transform of the signals, between synthetic seismograms computed using our method against those obtained by a discrete wavenumber method, which computes the complete wavefield.

The method proposed cannot be used whenever surface waves, near field terms, or in general low-frequency seismogram computations are required.

On the other hand, lots of applications of the method have been shown in this text, both in seismology and in underwater acoustics. Seismological problems discussed in this thesis are: identification of seismic phases on real data by the comparison with synthetics; the study of multiple reflections on seismogram in order to develop and refine model obtained with other methods; quantitative analyses on seismic phases to estimate the elastic parameter of given models; forward modelling of faulting sources and analyses of their focal mechanisms. Underwater acoustic problems discussed in this text are: analysis of the physical properties of the seawater, in particular for the Gulf of Naples, and their effects on the underwater acoustic propagation; definition of geoacoustic models for underwater environments; high-frequency underwater digital communications, studying their limits and the problems the acoustic channel produces; high frequency imaging of submerged objects; forward modelling of the acoustic wave propagation in the seawater in presence of scattering inhomogeneities.

These works have given the opportunity to study a large variety of problems in geophysics. Moreover, a contribution to different research project, as the SisMa project, the STSS-500 project, and the INGV-DPC V4 project, has been produced during the three years of this thesis work.

For the INGV-DPC V4 project, the method developed for rapid high-frequency seismogram computation, and its implementation in the COMRAD code, results one of the final products of the project.

For the SisMa project this study offers a new perspective to the future developments of the monitoring system considering wireless acoustic two-way communication between geophysical stations on the seafloor and moored buoys on the sea surface that provides connectivity back to the land by a radio link.

Finally, for the on-going STSS-500 project, a numerical simulator has been implemented in order to help the engineers in the development of a 3-D stereoscopic underwater acoustic camera. In particular, the simulator ties together the forward modelling and the imaging process of submerged objects.

Acknowledgements

I would like to thank all members of the Rissc-Lab Group, who have given me their availability during this thesis work and helpful suggestions. Many of them are not only colleagues but also good friends.

Moreover, I thank my tutor, Prof. Aldo Zollo, and Prof. Giovanni Iannaccone, for giving me the opportunity to work in this interesting research topic with an advanced research group.

Thank you, particularly, to Prof. Raffaella de Matteis for her continuous advice in the development of the high frequency method used during this thesis work. The work with her was constructive and successful, and it is opening new research opportunities.

Finally, I thank the engineers of the Whitehead Alenia Sistemi Subacquei of Monterusciello (Naples) for providing the technical specifications of underwater instrumentation and for the useful discussions on the topics of the SisMa and the STSS-500 projects.

Appendix A

The COMRAD Code

In this Appendix the User Guide and the source code of the COMRAD code are reported. The program can be downloaded from the Computer & Geosciences (Elsevier) website. A paper (Stabile *et al.*, 2008) on the method developed during this thesis work is in press under Computer & Geosciences journal.

A.1 User Guide

The propagation of seismic body waves in complex, laterally varying 3-D layered structures is a complicated process. Analytical solutions of the elastodynamic equations for such types of media are not known. The most common approaches to the investigation of seismic wavefields in such complex structures are:

1. methods based on direct numerical solutions of the elastodynamic equation, such as the finite-difference and finite-element methods

2. approximate high-frequency asymptotic methods (such as ray methods)

Both the methods are very useful for solving certain types of seismic problems, have their own advantages and disadvantages, and supplement each other suitability (Červený, 2001).

This program is based on ray-theory, where the solution of the elastodynamic equation is composed of elementary body waves that correspond to the various rays connecting the source to the receiver. Although the computation of ray synthetic seismograms is only approximate and the ray method can fail in certain situations, the high-frequency methods are preferable to direct numerical methods for many applications, both for the shorter computing times and for the full interpretability of the seismograms. The problems arise when we want to use a synthetic seismogram as similar to the real one as possible in the high-frequency approximation, such that the seismogram should be relatively complete, although it is not necessary that it contains every feature of the full elastic wave field. It is becoming necessary to select from all of the rays connecting the source to the receiver only those that produce appreciable amplitude on the seismogram.

A.1.1 What the program does

This program makes use of an algorithm to automatically generate an exhaustive set of seismic phases with appreciable amplitude on the seismogram. The method uses a hierarchical order of rays and seismic phases generation, taking into account some existence constraints for a ray-path and some physical constraints. To compute synthetic seismograms, the COMRAD code (from the Italian: "COdice Multifase per il RAy-tracing Dinamico") uses as its core the dynamic ray-tracing code provided by Farra and Madariaga (1987). Both the programs are written in FORTRAN77 language. For detailed information about the method used to build this program and its validation see Stabile et al, 2007.

A.1.2 Program Manual

This section covers installation and usage of *comrad*, including some shell script examples. The knowledge of the dynamic ray-tracing code provided by Farra and Madariaga (1987) and UNIX shell scripts is assumed here.

Installation

To compile the program you have to go into the source code directory *SRC* and type:

```
$ make
```

in fact the *makefile* in this directory compiles the source file *comrad.f* and moves the executable *comrad* in the *bin* directory created outside the *SRC* directory. Following is shown the structure of the *makefile* script:

```
#  COMRAD makefile
#  Author: Tony Alfredo Stabile
#  Date:   07 September 2007
#

BINDIR = bin

PROGS = comrad

install:       $(PROGS)
               if [ -n ../$(bindir) ]; then \
               mkdir -p ../$(BINDIR); \
               fi
               mv $(PROGS) ../$(BINDIR)

.SUFFIXES: .f

.f:
       f77  $*.f -o $*
```

Input files

The program needs the input parameters and the two *core* input files, one (*creation.inp*) indicating the physical properties of the propagation medium and one (*xxxx.dis*, where *xxxx* indicates a four characters name) setting the source(s)-receiver(s) geometry. An example of *creation.inp*[1] file is the following:

```
test                # name of the xxxx.dis file
0                   # overwrite the existing file: 1=no, 0=yes (CORE)
3                   # number of layers
0.0 5.0 10.0        # top layer depths
0.0 0.0  0.0 0.0  0.0 0.0 # tilt of the layers (CORE)
15.0                # depth of the last layer
0.0 30.0 0.0 30.0   # x0 x1 y0 y1 dimensions of the medium (CORE)
2                   # number of nodes (of splines) 1st layer (CORE)
0                   # velocity gradient: yes=1 no=0 (CORE)
2                   # numbers of sampling points in this layer (CORE)
0.0 5.0             # depths of the sampling points (CORE)
4.5 4.5             # Vp values (at each sampling point)
3                   # number of nodes (of splines) 2nd layer (CORE)
0                   # velocity gradient: yes=1 no=0 (CORE)
3                   # numbers of sampling points in this layer (CORE)
5.0 7.0 10.0        # depths of the sampling points (CORE)
6.0 6.5 6.8         # Vp values (at each sampling point)
2                   # number of nodes (of splines) 3rd (CORE)
1                   # velocity gradient: yes=1 no=0 (CORE)
7.0                 # Vp value (top)
7.2                 # Vp value (bottom)
1.732 1.732 1.732   # Vp/Vs ratios in each layer
2.2 2.2 2.5 2.6 2.7 2.75 # top and bottom densities in each layer
```

the *xxxx.dis* must take the name indicated in the first command line of the *creation.inp* file, so in this example it becomes *test.dis*. An example of the *xxxx.dis* file, i.e. *test.dis*[2] file, is the following :

```
0.0 0.0 6.0       # x,y,z of the source
0                 # iplan (CORE)
0.0 10            # depth z of the stations, number of stations
2 4 6 8 10 20 22 24 26 28  # x stations
0. 0. 0. 0. 0. 0. 0. 0. 0. 0. # y stations
```

[1] If in the comments of the command line there is the word CORE this means that the line is important only for the *core* and not for *comrad*

[2] If in the comments of the command line there is the word CORE this means that the line is important only for the *core* and not for *comrad*

```
 0.25             # dtau (CORE)
 0.0 180.0 1800   # TETAmin, TETAmax, nTETA (CORE)
 0.0 0.0 1        # PHImin, PHImax, nPHI (CORE)
 0.3 0.15         # distm, distm2 (CORE)
 0.1 0.2 100      # DIST accepted, DIST tolerated,ITMAX (CORE)
----------------  BELOW WILL BE REPLACED BY THE COMRAD OUTPUT
 3                # number of phases
 1 1              # ray-string length, idir (1=direct wave, 0=other waves)
 1                # id layer that contains the component of the ray-string
 1                # direct P-wave: wave polarization (1=P, 2=S)
 4 0              # ray-string length, idir (1=direct wave, 0=other waves)
 1 2 2 1          # id layer that contains the 1st,2nd,3rd,4rt component
 1 1 2 2          # P\S/ bottom of the second layer: wave pol. (1=P, 2=S)
 4 0              # ray-string length, idir (1=direct wave, 0=other waves)
 1 2 2 1          # id layer that contains the 1st,2nd,3rd,4rt component
 1 1 1 1          # P\P/ bottom of the second layer: wave pol. (1=P, 2=S)
```

it is clear from the second part of this file that the user must indicate the number of phases the *core* must calculate, writing also for each phase the ray-path and the polarization. This becomes a tedious work if we want to calculate synthetic seismograms as complete as possible, i.e. thousands of phases in the input file. The *comrad* program is developed to do this automatically and quickly (about a second).

How to run the program

You can run the program simply typing:

```
$ comrad < comrad.inp
```

where the input file *comrad.inp* has the following command lines:

```
2      # 1 P and S waves from the source; 2 only P waves from the source
1      # 1 select manually the max length of the ray-strings; 2 automatic
12     # maximum length of the ray-string
         (Cancel this line if you choose automatic selection)
1      # 1 type manually the value of the phase parameter; 2 automatic
1e-4   # value of the phase parameter - % of direct P-wave amplitude
         (Cancel this line if you set the automatic value)
1      # 1 set manually the multiple reflection parameter; 2 automatic
8      # value of the multiple reflection parameter
         (Cancel this line if you set the automatic value)
2      # 0 travel-times; 1 ray-paths; 2 seismograms
0      # 0 no free-surfaces effects; 1 free-surfaces effects
```

You can also run the program typing:

```
$ comrad
```

but in this case you have to insert manually the parameters. However, the *comrad* program will read automatically the information contained in the *creation.inp* and the *xxxx.dis* input files.

Output files

As explained in the section A.1.2, the second part of the *xxxx.dis* file will be replaced by the *comrad* output. Here the output files will not be shown because of their length (you can imagine a file like the second part of the *xxxx.dis* but with thousands of command lines). After the *comrad* program is run, it creates six output files:

1. 1nfasi.tmp (total number of phases for rays which start direction is up, i.e. first command line of the second part of the *xxxx.dis* file))
2. 1raggi.tmp (codification of ray-strings and phase strings, i.e. second part of the *xxxx.dis* file)
3. 1core.inp (input file for the *core* program)
4. 2nfasi.tmp (total number of phases for rays which start direction is down, i.e. first command line of the second part of the *xxxx.dis* file))
5. 2raggi.tmp (codification of ray-strings and phase strings, i.e. second part of the *xxxx.dis* file)
6. 2core.inp (input file for the *core* program)

the calculation of travel-times, ray-paths or synthetic seismograms is then divided in two steps. A first run of the *core* program is done using (1), (2) and (3) files, and then a second run of the *core* program is done using (4), (5) and (6) files. Below is shown the procedure step by step for the first run:

- cut the second part of the *xxxx.dis* file (here *test.dis*) and indicate in the 7th command line the initial and final starting angle for a ray[3]

```
$ sed -n 1,6p test.dis > cuttest.dis
$ echo 90.0 180.0 1800 >> cuttest.dis
$ sed -n 8,10p test.dis >> cuttest.dis
```

- concatenate *cuttest.dis*, *1nfasi.tmp* and *1raggi.tmp* files:

```
$ cat cuttest.dis 1nfasi.tmp 1raggi.tmp > test.dis
```

[3]Put 90°-180° if starting direction is up and 0°-90° if starting direction is down.

- run the *core* programs[4] (*creation* and *rayintpl2pt*) with the *core.inp* and *creation.inp* input file to overcome the program questions (*test.dis* input file will be read automatically)

```
$ creation < creation.inp
$ rayintpl2pt < core.inp
```

the *core* output should be a *xxxx.dat* ASCII file, if we choose to calculate the travel-times, a *xxxx.rai* binary file, if we choose to calculate the ray-paths, and a *xxxx.sis* ASCII file, if we choose to calculate the synthetic seismograms.

In particular the *xxxx.sis* ASCII file gives the Green functions and so it is necessary to use a convolution program to have the synthetic seismograms. There are available several freeware convolution programs (i.e. *sismos* developed by Véronique Farra).

Script example

This script does automatically all the instructions to create synthetic seismograms. It runs the *comrad* program, its *core* and uses *sismos* program for the convolution.

```
#! /bin/bash

#  Bash script "multiphase.sh"
#  Author: Tony Alfredo Stabile
#

comrad < comrad.inp

creation < creation.inp

nome=‘sed -n 1p creation.inp|awk ’{print $1}’‘
a1=90

for i in 1 2
do
  a2=$(echo "scale=3; $a1 + 90" | bc)
  nome1=‘sed -n 1p ${i}raypt.inp|awk ’{print $1}’‘
  nome2=${nome1}.tmp
  nome3=${i}nfasi.tmp
  nome4=${i}raggi.tmp
  nome5=${nome1}.dis
  if [ $i -eq 1 ]
```

[4]The *creation* program generates another input file (*xxxx.mil*) for the dynamic ray-tracing code *rayintpl2pt*. Contact Véronique Farra to have the core programs.

```
     then
         green1=$nome1
     else
         green2=$nome1
  fi
  cp ${nome}.mil ${nome1}.mil
  sed -n 1,6p ${nome}.dis > $nome2
  iteraz=‘sed -n 7,7p ${nome}.dis | awk ’{print $3/2}’‘
  echo $a1 $a2 $iteraz >> $nome2
  sed -n 8,10p ${nome}.dis >> $nome2
  cat $nome2 $nome3 $nome4 > $nome5

  rayintpl2pt < ${i}raypt.inp

  a1=0
done

for k in 1 3
do
  (
  echo "sismos.inp"
  echo "0"
  echo "1"
  echo "${green1}.sis"
  echo "1"
  echo "${green2}.sis"
  echo "0"
  echo "${k}"
  echo "2"
  echo "0.03"
  echo "0"
  ) > macro.tmp

  sismos < macro.tmp

  rm *.tmp
done

rm 1tes.mil 2tes.mil
exit
```

A.2 The source code

Following is shown the file `dimensioni.inc`, in which are defined the values of the parameters and the dimensions of variables, arrays, and matrices used in the `comrad` code.

```
c file "dimensioni.inc"     Multiphase code COMRAD
c AUTHOR: Tony Alfredo Stabile
c ************************************************************
c *                                                          *
c *                  Dimensions                              *
c *                                                          *
c *    dst: maximum number of elements                       *
c *    dnr: maximum number of rays                           *
c *    dl: maximum length of ray and phase strings           *
c *    dl2: maximum length of ray string + counter + multiple  *
c *         reflections + direction (up/down)                *
c *    df: maximum number of phases of each ray              *
c *                                                          *
c ************************************************************

      integer dst,dnr,dl,dl2,df
      parameter (dst=100,dnr=500000,dl=25,dl2=dl+2,df=4100)
```

Here is shown the source code of the COMRAD program. It is written in Fortran77.

```
c*************************************************************************
c*****
c***** COMRAD PROGRAM (COdice Multifase per il RAy-tracing Dinamico)
c***** AUTHOR:  Tony Alfredo Stabile
c***** EMAIL:   stabile@na.infn.it
c***** VERSION: 1.3
c*****
c***** THIS PROGRAM NEEDS THE INPUT FILES creation.inp AND ----.dis
c*****
c***** THE OUTPUT IS SAVED ON THE FOLLOWING FILES:
c***** 1nfasi.tmp, 1raggi.tmp, 2nfasi.tmp, 2raggi.tmp
c*****
c***** THE PROGRAM MAKE USE OF THE FOLLOWING SUBROUTINES:
c***** legginpdis, genray
c*****
c***** THE PROGRAM WRITE ALSO THE FILES 1raypt.inp AND 2raypt.inp
c***** WHICH GIVE THE INPUT PARAMETERS FOR THE rayintpl2pt PROGRAM
c***** (rayintpl2pt IS THE CORE PROGRAM DEVELOPED BY V. FARRA)
c*****
```

```
c***** READ THE USER GUIDE FOR ADDITIONAL INFORMATION
c**********************************************************************
      program comrad
      implicit none
      integer lmin,lmax,p,nf,ud,att,maxrefl
      integer j,l,m,r,s,opz,suplib
      character*4 nomefile
      character*10 rag,fas,inp
      real rif,frac
      common /perc/ frac
      common /rmul/ maxrefl
      att=0
      rif=0.
      call legginpdis(nomefile,m,r,s)
      write(*,*)'Only P waves from the source (YES=2)?'
      read(*,*)p
      lmin=abs(s-r)+1
      write(*,*)'Choose one of the two following options:'
      write(*,*)'1. Insert the maximum length of the ray strings'
      write(*,*)'2. Choose the default length (=Lmin+2m)'
      read(*,*)opz
      if (opz.eq.1) then
         write(*,*)'Insert the length (almost',lmin,')'
         read(*,*)lmax
      else
         lmax=lmin+2*m
      endif
      write (*,*)'Plan the phase selection:'
      write (*,*)'1. Manual plan'
      write (*,*)'2. Default plan (0.0001% of the direct P wave)'
      read (*,*)opz
      if (opz.eq.1) then
         write(*,*)'Insert the value'
         read(*,*)frac
      else
         frac=1e-4
      endif
      write (*,*)'Set the multiple reflection parameter:'
      write (*,*)'1. Manually'
      write (*,*)'2. Default value (RIFM = 8)'
      read (*,*)opz
      if (opz.eq.1) then
         write(*,*)'Insert the value'
```

```
         read(*,*)maxrefl
      else
         maxrefl=8
      endif
      if (lmax.gt.25) lmax=25
      write(*,*)'Choose one of the three following options:'
      write(*,*)'0. Calculate travel times'
      write(*,*)'1. Calculate ray-paths'
      write(*,*)'2. Calculate seismograms'
      read(*,*)opz
      write(*,*)'Do you want to take into account'
      write(*,*)'of free surface effects (YES=1, NO=0)?'
      read(*,*)suplib
      do ud=1,2
         write(inp,100),ud
100      format(i1,'raypt.inp')
         write(rag,200),ud
200      format(i1,'raggi.tmp')
         write(fas,300),ud
300      format(i1,'nfasi.tmp')
         OPEN(70,FILE=rag,FORM="FORMATTED")
         OPEN(71,FILE=inp,FORM="FORMATTED")
         write(71,400)ud,nomefile
400      format(i1,a3)
         write(71,*)opz
         write(71,*)suplib
         call genray(lmax,lmin,p,nf,ud,m,r,s,rif,att)
         CLOSE(70)
         CLOSE(71)
         OPEN(70,FILE=fas,FORM="FORMATTED")
         write(70,*)nf
         CLOSE(70)
      enddo
      end
c
c=============================================================
c*************************************************************
c***** THE legginpdis SUBROUTINE READS THE INFORMATION
c***** CONTAINED IN THE "creation.inp" AND "----.dis" FILES.
c*****
c***** THE TWO FILES MUST BE IN THE FOLDER WHERE THE PROGRAM
c***** WILL RUN
c*****
```

```
c***** THIS SUBROUTINE HAS TO BE SUBSTITUTED IF ANOTHER CORE
c***** IS USED INSTEAD OF rayintpl2pt
c*********************************************************
      SUBROUTINE legginpdis(nomefile,m,r,s)
      include 'dimensioni.inc'
      integer m,r,s
      integer i,j,h,tre(3),nstaz,diff(2)
      character*4 nomefile
      character*8 nomeintero
      real zs(3),zr(3)
      real spess(dst),dens(dst,2),vp(dst,2),vs(dst,2)
      real vpvs(dst),appo,appovet(205),prf(2)
      common /info1/ spess,dens,vp,vs
      common /info2/ zr,zs
      OPEN(8,FILE='creation.inp',STATUS='OLD',FORM="FORMATTED")
      read(8,*)nomefile,appo,m
      read(8,*) (appovet(i), i=1,m)
      do i=2,m
         spess(i-1)=appovet(i)-appovet(i-1)
      enddo
      appo=2*m+5
      read(8,*) (appovet(i), i=1,appo)
      do j=1,m
         read(8,*)tre(1),tre(2),tre(3)
         do h=1,2
            read(8,*) (appovet(i), i=1,tre(3))
         enddo
         vp(j,1)=appovet(1)
         vp(j,2)=appovet(tre(3))
      enddo
      read(8,*) (vpvs(i), i=1,m)
      do i=1,m
         vs(i,1)=vp(i,1)/vpvs(i)
         vs(i,2)=vp(i,2)/vpvs(i)
      enddo
      read(8,*) (dens(i,1),dens(i,2), i=1,m)
      CLOSE(8)
      write(nomeintero,500),nomefile
500   format(a4,'.dis')
      OPEN(9,FILE=nomeintero,FORM="FORMATTED")
      read(9,*) (zs(i), i=1,3)
      read(9,*) (appovet(i), i=1,3)
      zr(3)=appovet(2)
```

```
c...TO BE MODIFIED IF THE Y COORDINATE OF THE RECEIVERS ARE NOT EQUAL TO 0
      zr(2)=0.
c...END MODIFICATION
      nstaz=int(appovet(3))
      read(9,*) (appovet(i), i=1,nstaz)
      diff(1)=abs(appovet(1)-zs(1))
      diff(2)=abs(appovet(nstaz)-zs(1))
      if (diff(1).gt.diff(2)) then
         zr(1)=diff(1)
      else
         zr(1)=diff(2)
      endif
      CLOSE(9)
      prf(1)=0.
      do i=1,m
         prf(2)=prf(1)+spess(i)
         if ((zs(3).ge.prf(1)).and.(zs(3).lt.prf(2))) s=i
         if ((zr(3).ge.prf(1)).and.(zr(3).lt.prf(2))) r=i
         prf(1)=prf(2)
      enddo
      m=m-1
      return
      end
c
c=============================================================
c*************************************************************
c***** THE genray SUBROUTINE GENERATES RAY-STRINGS AND WRITES
c***** THE INFORMATION TO BE ADDED IN THE "----.dis" FILE
c*****
c***** THIS SUBROUTINE MAKE USE OF THE FOLLOWING SUBROUTINES:
c***** controlla, fase
c*************************************************************
      SUBROUTINE genray(lmax,lmin,p,nf,ud,m,r,s,rif,att)
      include 'dimensioni.inc'
      integer lmax,lmin,p,nf,ud,m,r,s,a(dl2,dnr,2),av(dl2),f(dl2,df)
      integer sw1,sw2,n,appo,cont,c,dec(4),att
      integer l,j,i,k,h,tot
      real zs(3),zr(3),rif
      common /info2/ zr,zs
      nf=0
      sw1=1
      sw2=2
      n=1
```

```
      a(1,1,sw1)=s
      a(3,1,sw1)=0
      a(4,1,sw1)=ud
      if ((zs(3).le.0.000001).and.(ud.eq.1)) return
      if ((s.eq.r).and.((zs(3).ne.0).or.(zr(3).ne.0))) then
         if ((zs(3).ge.zr(3)).and.(ud.eq.2)) goto 600
         if ((zs(3).le.zr(3)).and.(ud.eq.1)) goto 600
         write(70,*) '1 1'
         write(70,*) s
         write(70,*) '1'
         nf=nf+1
         if (p.ne.2) then
            write(70,*) '1 1'
            write(70,*) s
            write(70,*) '2'
            write(71,*) '1'
            nf=nf+1
         endif
600   endif
      do l=2,lmax
         cont=0
         do j=1,n
            do i=-1,1
               a(l,j,sw1)=a(l-1,j,sw1)+i
               do k=1,4
                  dec(k)=a(l-2+k,j,sw1)
               enddo
               call controlla(m,dec,c)
       if (c.eq.1) then
          cont=cont+1
  do k=1,l
     a(k,cont,sw2)=a(k,j,sw1)
  enddo
          do k=3,4
             a(l-1+k,cont,sw2)=dec(k)
  enddo
c*********************************************************
c****** START OUTPUT FOR THE RAYCODE **********************
c*********************************************************
          if ((a(l,cont,sw2).eq.r).and.((zr(3).ne.0).or.((zr(3)
     &.eq.0).and.(a(l+3,cont,sw2).eq.1)))) then
                   write(*,*) (a(k,j,sw1), k=1,l)
                   tot=0
```

```
     h=l+2
     do k=1,h
        av(k)=a(k,j,sw1)
     enddo
     call fase(m,tot,l,av,p,f,nf,ud,rif,att)
     if (tot.ne.0) then
                        do h=1,tot
                         if (l.eq.lmin) then
                              write(70,*) l,' 1'
                           else
                              write(70,*) l,' 0'
                           endif
           write(70,*) (a(k,j,sw1), k=1,l)
           write(70,*) (f(k,h), k=1,l)
c ... START COMMAND TO INDICATE A SV WAVE
                           if (f(1,h).eq.2) write(71,*) '1'
c ... END COMMAND TO INDICATE A SV WAVE
                           nf=nf+1
                        enddo
                     endif
          endif
c*************************************************************
c****** END OUTPUT FOR THE RAYCODE  ***********************
c*************************************************************
       endif
    enddo
 enddo
 n=cont
 appo=sw1
 sw1=sw2
 sw2=appo
      enddo
      return
      end
c
c============================================================
c*************************************************************
c***** THE SUBROUTINE controlla VERIFIES IF THE RAYS
c***** SATISFY THE SELECTED CONSTRAINTS ON RAYS. IF A RAY
c***** DOES NOT SATISFY THE CONSTRAINTS, THE c VARIABLE
c***** WILL BE 0, ELSE IT WILL BE 1
c*************************************************************
      SUBROUTINE controlla(m,dec,c)
```

```
      include 'dimensioni.inc'
      integer m,dec(4),c,updw,rifmult,maxrefl
      real spess(dst),dens(dst,2),vp(dst,2),vs(dst,2)
      common /info1/ spess,dens,vp,vs
      common /rmul/ maxrefl
      c=1
      if ((dec(2).gt.m).or.(dec(2).lt.1)) then
         c=0
         return
      endif
      if ((dec(4).eq.2).and.(dec(2).lt.dec(1))) then
         c=0
         return
      endif
      if ((dec(4).eq.1).and.(dec(2).gt.dec(1))) then
         c=0
         return
      endif
      if (dec(2).eq.dec(1)) then
         dec(3)=dec(3)+1
         if (dec(4).eq.1) then
            if (vp(dec(2),1).eq.vp(dec(2)-1,2)) then
       c=0
       return
    endif
    updw=1
 else
            if (vp(dec(2),2).eq.vp(dec(2)+1,1)) then
       c=0
       return
    endif
    updw=-1
         endif
      else
         dec(3)=0
         updw=0
      endif
      rifmult=dec(3)*dec(2)
      if (rifmult.gt.maxrefl) c=0
      dec(4)=dec(4)+updw
      return
      end
c
```

```
c============================================================
c************************************************************
c***** THE fase SUBROUTINE GENERATES 2^L PHASES FOR EACH RAY
c***** CREATED BY THE decray SUBROUTINE. THIS SUBROUTINE
c***** VERIFIES IF EACH PHASE SATISFIES THE SELECTED
c***** CONSTRAINTS ON PHASES. IF A PHASE DOES NOT SATISFY
c***** THE CONSTRAINTS, THE okko VARIABLE WILL BE 0,
c***** ELSE IT WILL BE 1
c************************************************************
      SUBROUTINE fase(m,tot,l,av,p,f,nf,ud,rif,att)
      include 'dimensioni.inc'
      integer m,tot,l,av(dl2),p,fa(dl2,df),f(dl2,df),nf,ud,att
      integer i,k,sw1,elevmax,okko,tb(dl2),tb2,inc,pol,w,rt
      real novs,rif,cf(4,5,2),imp1,imp2,cnt,frac
      real spess(dst),dens(dst,2),vp(dst,2),vs(dst,2)
      parameter (novs=0.001)
      data (cf(1,j,1),j=1,5)/0.17,0.45,0.73,1.00,0.71/,
     &(cf(2,j,1),j=1,5)/0.21,0.24,0.21,0.25,0.27/,
     &(cf(3,j,1),j=1,5)/0.01,0.02,0.02,0.02,0.17/,
     &(cf(4,j,1),j=1,5)/0.50,0.92,0.98,1.00,0.96/,
     &(cf(1,j,2),j=1,5)/0.70,0.69,0.37,0.24,0.35/,
     &(cf(2,j,2),j=1,5)/0.51,0.35,0.19,0.12,0.21/,
     &(cf(3,j,2),j=1,5)/0.17,0.07,0.03,0.03,0.05/,
     &(cf(4,j,2),j=1,5)/0.90,0.66,0.19,0.10,0.16/
      common /info1/ spess,dens,vp,vs
      common /perc/ frac
      tb(1)=ud
      do i=2,l
         tb(i)=abs(abs(av(i)-av(i-1))-1)+tb(i-1)
         if (tb(i).eq.3) tb(i)=1
      enddo
      write(*,*)'...the phase strings will be generated'
      elevmax=2**l
      do k=1,elevmax
c*********  START CREATION OF ALL THE PHASES  **********
         if (k.eq.1) then
            do i=1,l
               fa(i,k)=1
            enddo
         else
            sw1=0
            do i=1,l
               if (sw1.eq.1) fa(i,k)=fa(i,k-1)
```

```
               if (sw1.eq.2) then
                  if (fa(i,k-1).eq.1) then
                     sw1=1
                     fa(i,k)=2
                  else
                     fa(i,k)=1
                  endif
               endif
               if ((sw1.eq.0).and.(fa(i,k-1).eq.1)) then
                  fa(i,k)=2
                  sw1=1
               endif
               if ((sw1.eq.0).and.(fa(i,k-1).eq.2)) then
                  fa(i,k)=1
                  sw1=2
               endif
            enddo
         endif
c********  END CREATION OF ALL THE PHASES  ********
c********  START SELECTION OF PHASES  ********
         if (((p.eq.2).and.(fa(1,k).eq.1)).or.(p.eq.1)) then
            okko=0
            prod=1
            do i=1,l-1
               if ((vs(av(i),1).lt.novs).and.(fa(i,k).eq.2)) then
                  okko=1
                  goto 700
               endif
               rt=abs(tb(i)-tb(i+1))+1
               pol=2*fa(i,k)+fa(i+1,k)-2
               if (tb(i).eq.1) then
                  tb2=2
                  inc=-1
               else
                  tb2=1
                  inc=1
               endif
               if (pol.le.2) then
                  imp1=vp(av(i),tb(i))*dens(av(i),tb(i))
                  imp2=vp(av(i)+inc,tb2)*dens(av(i)+inc,tb2)
               else
                  imp1=vs(av(i),tb(i))*dens(av(i),tb(i))
                  imp2=vs(av(i)+inc,tb2)*dens(av(i)+inc,tb2)
```

```
               endif
               cnt=imp1/imp2
               if (cnt.le.0.5) w=1
               if ((cnt.gt.0.5).and.(cnt.le.0.8)) w=2
               if ((cnt.gt.0.8).and.(cnt.le.0.95)) w=3
               if ((cnt.gt.0.95).and.(cnt.le.1.2)) w=4
               if (cnt.gt.1.2) w=5
               prod=prod*cf(pol,w,rt)
               if (prod.lt.rif) okko=1
            enddo
            if (att.eq.0) then
               att=1
               rif=prod*frac/100
            endif
            if ((vs(av(l),1).lt.novs).and.(fa(l,k).eq.2)) okko=1
700         if (okko.eq.0) then
               tot=tot+1
               do i=1,l
                  f(i,tot)=fa(i,k)
               enddo
            endif
         endif
c********   END SELECTION OF PHASES   ********
      enddo
      return
      end
```

Appendix B

Fundamentals of underwater acoustics

In this Appendix some concepts and equations used commonly in underwater acoustics will be introduced. Here we illustrate briefly the concept of micropascal reference unit and the Decibel.

The level of an acoustic wave is defined as the number of decibels by which its intensity I differs from the intensity of a reference sound wave I_0:

$$I(\text{dB}) = 10 \log \left(\frac{I}{I_0} \right) \tag{B.1}$$

Since $I = p^2/\rho c$, where p is the pressure, ρ is the density, and c is the sound velocity, if ρc can be considered as constant (as usual), the above equation can be written as follows:

$$I(\text{dB}) = 20 \log \left(\frac{p}{p_0} \right) \tag{B.2}$$

The unit of intensity in underwater acoustics is the intensity of a plane wave having a pressure of 1 μPa, or equivalently 10^5 dyne per square centimetre (dyn/cm^2). Thus, a wave having intensity 1000 times that of a plane wave of pressure 1 μPa, using equation (B.1), it would be said to have a level of 30 dB re 1 μPa.

Following the sonar equations, the sound attenuation in seawater, and the calculation of the transmission reliability will be discussed in separated sections.

B.1 The sonar equations

The many phenomena and effects that are related to the sound propagation in the seawater can be grouped together quantitatively in a small number of sonar parameters, which are related to the sonar equations. These equations tie together the medium, the target and the equipment effects and are used to set one of the sonar parameters if the others are known.

The sonar equations are founded on a basic equality between the desired and the undesired portions of the received signal. In fact, the portion of the total acoustic field at the receiver which is desired is called the signal while the portion undesired is called the background. In sonar equations the background is either noise (undesired waves in the seawater) or reverberation (return of own acoustic wave due to scatterers in the seawater). The objective of the sonar equations is to find means for increasing the response of the sonar system and decreasing the response of the system to the background.

The sonar parameters are levels in unit decibels relative to the standard reference pressure of a 1-μPa plane wave. Table B.1 shows the sonar parameters determined by the equipment, the medium, and the target, respectively. The sonar parameters that represent

Equipment	**Medium**	**Target**
Projector Source Level: SL	Transmission Loss: TL	Target Source Level: SL
Self Noise Level: NL	Ambient-Noise Level: NL	Target Strength: TS
Directivity Index: DI	Reverberation Level: RL	
Detection Threshold: DT		

Table B.1: *Sonar parameters determined by the equipment, the medium, and the target, respectively.*

the desired portion of the acoustic wavefield at the receiver are SL, TS, and DI, while the undesired portion of the acoustic wavefield at the receiver is represented by TL, NL, and RL. The difference between the first group of parameters and the second is the signal-to-background ratio, commonly called simply signal-to-noise ratio SNR. Finally, the Detection Threshold DT parameter gives an indication of the presence or the absence of the target. In other words, when the input signal-to-noise ratio SNR is above a certain DT fulfilling certain probability criteria, the target is considered present, else the target is absent. Now we will obtain the sonar equations for active and passive sonar.

In the case of active sonars a sound source acting also as receiver produces by some means a source level of SL decibels at unit distance (1 m). When the sound reaches the target it is reduced by the transmission loss TL. On reflection or scattering by the target, the reflected or backscattered level has a gain at a unit distance from the target equal to the target strength TS. When the sound propagates back toward the source it is again reduced by TL. Moreover, in the seawater there is a noise level (neglecting the reverberation) which is reduced by the directivity index DI of the transducer acting as a receiver. Taking into account these quantities, the equation for active sonar becomes:

$$SNR = SL - 2TL + TS - (NL - DI) = SL - 2TL + TS - NL + DI \tag{B.3}$$

A modification is required when the background is reverberation instead of noise. In this case the terms $NL - DI$ of equation (B.3) is replaced by an equivalent plane-wave reverberation level RL:

$$SNR = SL - 2TL + TS - RL \tag{B.4}$$

where DT has a different value than DT for noise.

In the case of passive sonar, the target itself produces the signal with a source level of SL decibels at 1 meter distance. Moreover, the target strength TS is not considered yet and one-way transmission loss is involved. So for passive sonar the equation (B.3) becomes:

$$SNR = SL - TL - NL + DI \tag{B.5}$$

which is the equation (4.6) used in section 4.2.2 without the directivity index since in that simulation omnidirectional sources and receivers have been considered.

The SNR value can be finally compared with the detection threshold DT in order to make a decision on the presence ($SNR \geq DT$) or absence ($SNR < DT$) of the target.

B.2 Sound attenuation in seawater up to a frequency of 1 MHz

The geometrical spreading is not the unique cause of the sound attenuation in seawater: the underwater acoustic wave propagation is subjected also to scattering and absorption effects, which produce additional attenuation of the sound energy. The absorption of sound in seawater is considered to be that of pure water plus an excess absorption due to small amounts of various salts in the sea. In particular, the sound absorption is due by the combination of the two following different processes:

1. viscous dissipation of energy (pure water absorption)
2. chemical relaxation of magnesium sulphate ($MgSO_4$) and boric acid (H_3BO_3)

Each process dominates compressional wave attenuation in seawater in a particular range of frequencies. From 50 Hz to 10 kHz the boric acid contribution becomes the most important, although this is only 0.055% of the total molality of seawater. Also magnesium sulphate is present in little quantities equal to 0.84% of the total molality of seawater, but its relaxation process dominates the wave attenuation in the band of frequencies between 10 kHz and 200 kHz. At frequencies above 200 kHz, pure water absorption (due to shear and bulk viscosity of freshwater) is the largest contributor (Jackson and Richardson, 2007; Jensen *et al.*, 2000).

Several studies carried out between the 1950's and the 1980's demonstrated that the sound attenuation in the water increases according to the square of the frequency and it depends from the processes described above. The equation for the absorption coefficient α at frequency f in seawater is usually written, following the notation of (Fisher and Simmons, 1977), as

$$\alpha(\text{dB/km}) = \frac{A_1 P_1 f_1 f^2}{f_1^2 + f_2} + \frac{A_2 P_2 f_2 f^2}{f_2^2 + f_2} + A_3 P_3 f^2 \tag{B.6}$$

where indexes 1, 2, and 3 indicate the dependence from the chemical relaxation of boric acid, the chemical relaxation of magnesium sulphate, and the water viscosity, respectively.

The dependencies from the pressure in the three processes are indicated with P_1, P_2, and P_3, respectively. Finally, the two relaxation frequencies (expressed in KHz) are indicated with f_1 and f_2. A_1, A_2, and A_3 terms were originally considered as constants, but it was experimentally demonstrated (Francois and Garrison, 1982ba,b) that they vary with the water properties. A_1 and A_2 terms are both expressed in dB/(km $\cdot$ kHz), while A_3 term is expressed in $[\mathrm{dB}/(\mathrm{km} \cdot \mathrm{kHz})]^2$.

A simplified expression of equation (B.6) was formulated by Thorp (1967) and optimized later by Fisher and Simmons (1977). The Thorp's formula is still commonly used for the calculation of the sound attenuation α in seawater up to a frequency of 100 kHz. Its expression is the equation (4.3) used in the section 4.2.1, which is reported here again for completeness:

$$\alpha(\mathrm{dB/km}) = 3.3 \cdot 10^{-3} + \frac{0.11 f^2}{1+f^2} + \frac{44 f^2}{4100+f^2} + 3.0 \cdot 10^{-4} f^2 \tag{B.7}$$

with the frequency f in kHz. Francois and Garrison (1982aa, 1982bb) obtained in the 1982 a more complete expression for the seawater sound attenuation α (in dB/km) with depends not only from the frequency f (as for the Thorp's formula), but considering the terms A_1, A_2, and A_3 as functions of the seawater parameters like the temperature, the depth (or pressure), the salinity, and the pH. Following, the values obtained by Francois and Garrison for the terms of the equation (B.6) are reported:

$$\underline{\text{Boric acid contribution}} \begin{cases} A_1 &= \dfrac{8.86}{c} \cdot 10^{(0.78\mathrm{pH}-5)} \\ P_1 &= 1 \\ f_1 &= 2.8(S/35)^{0.5} \cdot 10^{(4-1245/\theta)} \end{cases}$$

$$\underline{\text{Magnesium sulphate contribution}} \begin{cases} A_2 &= 21.44 \dfrac{S}{c}(1+0.025T) \\ P_2 &= 1 - 1.37 \cdot 10^{-4} D + 6.2 \cdot 10^{-9} D^2 \\ f_2 &= \dfrac{8.17 \cdot^{(8-1990/\theta)}}{1+0.0018(S-35)} \end{cases}$$

$$\underline{\text{Water viscosity contribution}} \begin{cases} P_3 &= 1 - 3.83 \cdot 10^{-5} D + 4.9 \cdot 10^{-10} D^2 \\ \text{For T} &\leq 20^\circ\mathrm{C} \\ A_3 &= 4.937 \cdot 10^{-4} - 2.59 \cdot 10^{-5} T \\ &\quad +9.11 \cdot 10^{-7} T^2 - 1.50 \cdot 10^{-8} T^3 \\ \text{For T} &> 20^\circ\mathrm{C} \\ A_3 &= 4.937 \cdot 10^{-4} - 2.59 \cdot 10^{-5} T \\ &\quad +9.11 \cdot 10^{-7} T^2 - 1.50 \cdot 10^{-8} T^3 \end{cases}$$

where c is the sound velocity (m/s) which can be calculated by the use of one of the various expressions in literature (e.g., the equation of Del Grosso (1974)), T is the temperature (°C), $\theta = 273 + T$, S is the salinity (ppm), D is the depth (m), and f is the frequency (kHz).

The empirical equation of Francois and Garrison is valid for frequencies between 200 Hz and 1 MHz, for seawater temperature from -2 °C to 30 °C, for typical values of the seawater[1] pH (from 7.6 to 8.3), for salinity between 30 ppm and 40 ppm, and for depth also bigger than 3000 m.

B.3 Calculation of the transmission reliability

The velocity of a binary sequential source which emits K bits in a time T, is defined by the ratio

$$R_s \equiv \frac{K}{T} \tag{B.8}$$

and it is expressed in bit/s, or in kbit/s. The capacity of the communication channel is related to the bandwidth w of the transmission medium and to the signal-to-noise ratio by the following expression:

$$C \equiv w \log_2 \left(1 + \frac{S}{N}\right) \tag{B.9}$$

The Shannon's capacity theorem (Shannon, 1948) states that error-free transmission in a digital communication system is possible as long as the transmitter velocity R_s is less then the channel's capacity C, hence

$$R_s \leq C \tag{B.10}$$

If we want to know the value of the signal-to-noise ratio in decibels (dB), below which the digital communication is no longer reliable, taking into account that

$$\frac{S}{N}(dB) = 10 \log_{10} \left(\frac{S}{N}\right) \tag{B.11}$$

and using the equations (B.9) and (B.10), we have the following result:

$$\frac{S}{N}(dB) = 10 \left(2^{\frac{R_s}{w}} + 1\right) \tag{B.12}$$

As an example, if the bandwidth of the transmission channel is equal to 10 kHz and the transmitter velocity is equal to 2.4 kbit/s, the signal-to-noise ratio must be

$$\frac{S}{N} \geq 21.8 \text{ dB}$$

for a reliable (error-free) transmission in a digital communication system with these characteristics.

[1] In particular in the Gulf of Naples the seawater pH is about 8.1-8.2.

Bibliography

Adams, A., Hinton, O., Sharif, B., Salles, G., Orr, N., and Tsiminedes, C. (2000). An experiment in sub-sea networks – the lotus sea trials. In *ECUA'00, Lyon, France*.

Aki, K. and Richards, P. G. (2002). *Quantitative Seismology*. University Science Books, Sausalito, California, second edition.

Akyildiz, I. F., Pompili, D., and Melodia, T. (2005). Underwater acoustic sensor networks: Research challenges. *Elsevier's Ad Hoc Networks*, **3**, 257–279.

Atkin, R. J. and Fox, N. (1980). *An introduction to the theory of Elasticity*. Longman London and New York.

Badia, L., Mastrogiovanni, M., and Zorzi, M. (2006). An optimization framework for joint sensor deployment, link scheduling and routing in underwater sensor networks. *in Proc. First ACM International Workshop on Underwater Networks WUWNet'06 Los Angeles, California, USA*, **September 25**, 56–63.

Ben-Menahem, A. and Singh, S. J. (1981). *Seismic Waves and Sources*. Springer-Verlag New York Heidelberg Berlin.

Benson, B., Chang, G., Manov, D., Graham, B., and Kastner, R. (2006). Design of a low-cost acoustic modem for moored oceanographic applications. *in Proc. First ACM International Workshop on Underwater Networks WUWNet'06 Los Angeles, California, USA*, **September 25**, pp. 71–78.

Bernard, P. and Zollo, A. (1989). The irpinia (italy) 1980 earthquake: detailed analysis of a complex normal faulting. *Journal of Geophysical Research*, **94**(B2), 1631–1647.

Beydoun, W. B. and Keho, T. H. (1987). The paraxial ray method. *Geophysics*, **52**, 1639–1653.

Bohlen, T. (2004). *Analysis of seismic waves in the presence of small-scale strong material discontinuities*. Habilitation thesis, Christian-Albrechts-Universität Kiel, Germany.

Bouchon, M. (1981). A simple method to calculate green's functions for elastic layered media. *Bulletin of the Seismological Society of America*, **71**(4), 959–971.

Bouchon, M. and Aki, K. (1977). Discrete wave-number representation of seismic-source wave fields. *Bulletin of the Seismological Society of America*, **67**(2), 250–277.

Brokešová, J. (2006). *Asymptotic ray method in seismology: A tutorial.* Matfyzpress, Praha.

Brune (1970). Tectonic stress and the spectra of seismic shear waves from earthquakes. *Journal of Geophysical Research*, **75**(26), 4997–5009.

Catipovic, J. A. (1990). Performance limitations in underwater acoustic telemetry. *IEEE J. Ocean. Eng.*, **15**, 205–216.

Cazzolato, B. S., Nelson, P., Joseph, P., and Brind, R. J. (2001). Numerical simulation of optimal deconvolution in a shallow-water environment. *Journal of the Acoustical Society of America*, **110**(1), pp. 170–185.

Chen, C. T. and Millero, F. J. (1977). Speed of sound in seawater at high pressure. *Journal of the Acoustical Society of America*, **62**, 1129–1135.

Clarke, T. J. (1993a). The complete ordered ray expansion – i. calculation of synthetic seismograms. *Geophysical Journal International*, **115**, 421–434.

Clarke, T. J. (1993b). The complete ordered ray expansion – ii. multiphase body wave tomography. *Geophysical Journal International*, **115**, 435–444.

Coates, R. F. W. (1990). *Underwater acoustic systems.* John Wiley and Sons.

Coates, R. F. W. (1993). Underwater acoustic communications. *in Proc. OCEANS '93, Victoria, Canada*, **III**, 420–425.

Cohen, J. K. and Stockwell, J. W. (2007). *CWP/SU: Seismic Unix Release 40: an open source software package for seismic research and processing.* Center for Wave Phenomena, Colorado School of Mines, Golden, Colorado. http://www.cwp.mines.edu/cwpcodes/index.html.

Coppens, A. B. (1981). Simple equations for the speed of sound in neptunian waters. *Journal of the Acoustical Society of America*, **69**(3), pp. 862–863.

Coutant, O. (1989). Program of numerical simulation axitra. In *Res. Report LGIT, Grenoble, in French.*

Dahl, P. (2004). The sea surface bounce channel. bubble-medianted energy loss and time/angle spreading. In *in High Frequency Ocean Acoustics*, pages 194–203. Eds. M. Porter, M. Siderius, and W. Kuperman, American Institute of Physics.

De Dominicis Rotondi, A. (1990). *Principi di elettroacustica subacquea Vol.I.* Ed. ELSAG, Genova.

De Dominicis Rotondi, A. (1995). *Principi di elettroacustica subacquea Vol.II: Le caratterizzazioni dell'ambiente operativo marino*. Edizioni Scriba.

De Dominicis Rotondi, A. (1996). *Principi di elettroacustica subacquea Vol.III: Il canale acustico marino*. Edizioni Scriba.

Del Grosso, V. A. (1974). New equation for the speed of sound in natural waters (with comparisons to other equations). *Journal of the Acoustical Society of America*, **56**(4), pp. 1084–1091.

Farra, V. and Madariaga, R. (1987). Seismic waveform modeling in heterogeneous media by ray perturbation theory. *Journal of Geophysical Research*, **92**(B3), 2697–2712.

Festa, G. and Vilotte, J. P. (2005). The newmark scheme as a velocity-stress time-staggering: an efficient perfectly matched layers implementation for spectral element simulations of elastodynamics. *Geophysical Journal International*, **161**(3), 789–812.

Fisher, F. H. and Simmons, V. P. (1977). Sound absorption in sea water. *Journal of the Acoustical Society of America*, **62**(3), pp. 558–564.

Francois, R. E. and Garrison, G. R. (1982a). Sound absorption based on ocean measurements: Part i: Pure water and magnesium sulfate contributions. *Journal of the Acoustical Society of America*, **72**(3), 896–907.

Francois, R. E. and Garrison, G. R. (1982b). Sound absorption based on ocean measurements: Part ii: Boric acid contribution and equation for total absorption. *Journal of the Acoustical Society of America*, **72**(6), 1879–1890.

Giberti, G., Yven, B., Zamora, M., and Vanorio, T. (2006). Database on laboratory measured data on physical properties of rocks of campi flegrei volcanic area (italy). In A. Zollo, P. Capuano, and M. Corciulo, editors, *Geophysical Exploration of the Campi Flegrei (Southern Italy) Caldera' Interiors: Data, Methods and Results*, chapter 4, pages 179–192. Doppiavoce.

Gritto, R., Korneev, V. A., and Johnson, L. R. (1995). Low-frequency elastic-wave scattering by an inclusion: limits of applications. *Geophysical Journal International*, **120**(3), 677–692.

Gubernatis, J. E., Domany, E., Krumhansl, J. A., and Thompson, R. M. (1977). The born approximation in the theory of the scattering of elastic waves by flaws. *Journal of Applied Physics*, **48**(7), 2812–2819.

Hamilton, E. L. (1979a). Sound velocity gradients in marine sediments. *Journal of the Acoustical Society of America*, **65**(4), 909–922.

Hamilton, E. L. (1979b). Vp/vs and poisson's ratios in marine sediments and rocks. *Journal of the Acoustical Society of America*, **66**(4), 1093–1101.

Hamilton, E. L. (1980). Geoacoustic modeling of the sea floor. *Journal of the Acoustical Society of America*, **68**(5), 1313–1340.

Hron, F. (1971). Criteria for selection of phases in synthetic seismograms for layered media. *Bulletin of the Seismological Society of America*, **61**(3), 765–779.

Hron, F. (1972). Numerical methods of ray generation in multilayered media. In *Methods in Computational Physics*, volume 12, pages 1–34. Academic Press, New York.

Hron, F., May, B. T., Covey, J. D., and Daley, P. F. (1986). Synthetic seismic section for acoustic, elastic, anisotropic inhomogeneous layered media. *Geophysics*, **51**, 710–735.

Hursky, P., Porter, M. B., Siderius, M., and McDonald, V. K. (2006). Point-to-point underwater acoustic communications using spread-spectrum passive phase conjugation. *Journal of the Acoustical Society of America*, **120**(1), 247–257.

Jackson, D. R. and Richardson, M. D. (2007). *High-Frequency Seafloor Acoustics*. Springer New York, USA.

Jaffe, J. and Schurgers, C. (2006). Sensor networks of freely drifting autonomous underwater explorers. *in Proc. First ACM International Workshop on Underwater Networks WUWNet'06 Los Angeles, California, USA*, **September 25**, pp. 93–96.

Jensen, F. B., Kuperman, W. A., Porter, M. B., and Schmidt, H. (2000). *Computational ocean acoustics*. Springer-Verlag.

Kaser, M. and Dumbser, M. (2006). An arbitrary high order discontinuous galerkin method for elastic waves on unstructured meshes i: the two-dimensional isotropic case with external source terms. *Geophysical Journal International*, **166**(2), 855–877.

Kinsler, L. E., Frey, A. R., Coppens, A. B., and Sanders, J. V. (2000). *Fundamentals of Acoustics*. John Wiley & Sons, fourth edition.

Knudsen, V. O., Alford, R. S., and Emling, J. W. (1948). Underwater ambient noise. *Journal of Marine Research*, **22**, 410–429.

Komatitsch, D. and Vilotte, J. P. (1998). The spectral element method: an efficient tool to simulate the seismic response of 2d and 3d geological structures. *Bulletin of the Seismological Society of America*, **88**(2), 368–392.

Kristeková, M., Kristek, J., Moczo, P., and Day, S. M. (2006). Misfit criteria for quantitative comparison of seismograms. *Bulletin of the Seismological Society of America*, **96**(5), 1836–1850.

Krüger, F., Scherbaum, F., Weber, M., and Schlittenhardt, J. (1996). Analysis of asymmetric multipathing with a generalization of the double-beam method. *Bulletin of the Seismological Society of America*, **86**(3), pp. 737–749.

Lay, T. and Wallace, T. C. (1995). *Modern Global Seismology*. Academic Press.

Lee, W. H. K. and Lahr, J. C. (1975). Hypo71 (revised): A computer program for determining hypocenter, magnitude and first motion pattern of local earthquakes. Open-File Report 75-311, US Department of Interior Geological Survey, National Center for Earthquake Research, Menlo Park, CA. pp.114.

Liu, G. R., Li, W., Zhang, X. M., and Varadan, V. K. (2003). Shape identification of underwater objects using backscattered frequency signals. *Journal of the Acoustical Society of America*, **113**(6), 3146–3154.

Ludwig, W. J. J., Nafe, E., and Drake, C. L. (1970). Seismic refraction. In *in The Sea*, pages 53–84. edited by A. E. Maxwell, Wiley Intersc. Hoboken N. J.

Mackenzie, K. V. (1981). Nine-term equation for sound speed in the oceans. *Journal of the Acoustical Society of America*, **70**(3), pp. 807–812.

Madariaga, R. (1976). Dynamics of an expanding circular fault. *Bulletin of the Seismological Society of America*, **66**, 639–666.

Maercklin, N. (2004). *Seismic structure of the Arava Fault, Dead Sea Transform*. Dissertation, Universität Potsdam, Germany. urn:nbn:de:kobv:517-0001469.

Maercklin, N. and Zollo, A. (2008). Analysis of ps-to-pp amplitude ratios for seismic reflector characterisation: method and application. In *Conception, verification, and application of innovative techniques to study active volcanoes, INGV-DPC V4*, pages 265–275. Sottovoce (in press).

Maercklin, N., Haberland, C., Ryberg, T., Weber, M., Bartov, Y., and DESERT Group (2004). Imaging the dead sea transform with scattered seismic waves. *Geophysical Journal International*, **158**(8), 179–186.

Marfurt, K. J. (1984). Accuracy of finite-difference and finite-element modeling of the scalar and elastic wave equations. *Geophysics*, **49**, 553–549.

Müller, C. (2000). *On the Nature of Scattering from Isolated Perturbations in Elastic Media and the Consequences for Processing of Seismic Data*. Dissertation, Christian-Albrechts-Universität, Kiel, Germany.

Nelder, J. A. and Mead, R. (1965). A simplex method for function minimization. *Computer Journal*, **7**, 308–313.

Pengcheng, L. and Archuleta, R. J. (2004). A new nonlinear finite fault inversion with three-dimensional green's functions: application to the 1989 loma prieta, california, earthquake. *Journal of Geophysical Research*, **109**(B02318), 1–15.

Pompili, D., Melodia, T., and Akyildiz, I. F. (2006). Deployment analysis in underwater acoustic wireless sensor networks. *in Proc. First ACM International Workshop on Underwater Networks WUWNet'06 Los Angeles, California, USA*, **September 25**, pp. 48–55.

Preisig, J. (2006). Acoustic propagation considerations for underwater acoustic communications network development. *in Proc. First ACM International Workshop on Underwater Networks WUWNet'06 Los Angeles, California, USA*, **September 25**, pp. 1–5.

Press, W. H., Teukolsky, S. A., Vetterling, W. T., and Flannery, B. P. (2003). *Numerical Recipes in Fortran 77: The Art of Scientific Computing*. Cambridge University Press, second edition.

Reasenberg, P. A. and Oppenheimer, D. (1985). Fpfit, fpplot, and fppage: Fortran computer programs for calculating and displaying earthquake fault-plane solutions. Open-File Report 85-739, U.S. Geological Survey.

Rosenbaum, J. H. (1960). The long-time response of a layered elastic medium to explosive sound. *Journal of Geophysical Research*, **65**, 1577–1613.

Rosi, M. and Sbrana, A. (1987). *Phlegraean Fields*, volume 114. CNR, Quaderni de "La Ricerca Scientifica".

Scherbaum, F., Krüger, F., and Weber, M. (1997). Double beam imaging: Mapping lower mantle heterogeneities using combinations of source and receiver arrays. *Journal of Geophysical Research*, **102**(B1), pp. 507–522.

Schimmel, M. and Paulssen, H. (1997). Noise reduction and detection of weak, coherent signals through phase-weighted stacks. *Geophysical Journal International*, **130**(2), pp. 497–505.

Shannon, C. E. (1948). A mathematical theory of communication. *Bell System Technical Journal*, **27**, 379–423, 623–656.

Smith, K. B., Abrantes, A. A. M., and Larraza, A. (2003). Examination of time-reversal acoustics in shallow water and applications to noncoherent underwater communications. *Journal of the Acoustical Society of America*, **113**(6), pp. 3095–3110.

Snieder, R. and Spencer, C. (1993). A unified approach to ray bending, ray perturbation, paraxial ray theories. *Geophysical Journal International*, **115**, 456–470.

Sozer, E. M., Stojanovic, M., and Proakis, J. G. (2000). Underwater acoustic networks. *IEEE Journal of Oceanic Engineering*, **25**, 72–83.

Stabile, T. A., Zollo, A., Vassallo, M., and Iannaccone, G. (2007). Underwater acoustic channel properties in the gulf of naples and their effects on digital data transmission. *Annals of Geophysics*, **50**(3), 313–328.

Stabile, T. A., de Matteis, R., and Zollo, A. (2008). Method for rapid high-frequency seismogram calculation. *Computer & Geosciences*. (in press).

Stojanovic, M. (1996). Recent advances in high-speed underwater acoustic communications. *IEEE J. Ocean. Eng.*, **21**, 125–136.

Stojanovic, M. (2005). Retrofocusing techniques for high rate acoustic communications. *Journal of the Acoustical Society of America*, **117**(3), 1173–1185.

Stojanovic, M. (2006). On the relationship between capacity and distance in an underwater acoustic communication channel. *in Proc. First ACM International Workshop on Underwater Networks WUWNet'06 Los Angeles, California, USA*, **September 25**, 41–47.

Stojanovic, M., Catipovic, J. A., and Proakis, J. G. (1993). Adaptive multichannel combining and equalization for underwater acoustic communications. *Journal of the Acoustical Society of America*, **94**, 961–672.

Stojanovic, M., Catipovic, J. A., and Proakis, J. G. (1994). Phase coherent digital communications for underwater acoustic channels. *IEEE J. Ocean. Eng.*, **19**, 100–111.

Stojanovic, M., Catipovic, J. A., and Proakis, J. G. (1995). Reduced complexity spatial and temporal processing of underwater acoustic communication signals. *Journal of the Acoustical Society of America*, **98**, 961–672.

Telford, W. M., Geldart, L. P., and Sheriff, R. E. (1990). *Applied Geophysics (second edition)*. Cambridge University Press.

Thorp, W. H. (1967). Analytic description of the low-frequency attenuation coefficient. *Journal of the Acoustical Society of America*, **42**(1), 270.

Urick, R. J. (1983). *Principles of underwater sound (third edition)*. Peninsula Publishing.

Urick, R. J. (1986). *Ambient noise in the sea*. Peninsula Publishing.

Červený, V. (2001). *Seismic Ray Theory*. Cambridge University Press, first edition.

Červený, V. and Hron, F. (1980). The ray series method and dynamic ray tracing system for three-dimensional inhomogeneous media. *Bulletin of the Seismological Society of America*, **70**(1), 47–77.

Virieux, J. (1986). P-sv wave propagation in heterogeneous media: Velocity-stress finite-difference method. *Geophysics*, **51**, 889–901.

Virieux, J. (1991). Fast and accurate ray tracing by hamiltonian perturbation. *Journal of Geophysical Research*, **96**, 579–594.

Weber, E., Convertito, V., Iannaccone, G., Zollo, A., Bobbio, A., Cantore, L., Corciulo, M., Crosta, M. D., Elia, L., Martino, C., Romeo, A., and Satriano, C. (2007). An advanced seismic network in the southern apennines (italy) for seismicity investigations and experimentation with earthquake early warning. *Seismological Research Letters*, **78**(6), 622–634.

Wenz, G. M. (1962). Acoustic ambient noise in the ocean: Spectra and sources. *Journal of the Acoustical Society of America*, **34**(12), 1936–1956.

Wong, G. S. K. and Zhu, S. (1995). Speed of sound in seawater as a function of salinity, temperature, and pressure. *Journal of the Acoustical Society of America*, **97**(3), 1732–1736.

Yilmaz, O. (2001). *Seismic Data Analysis - Investigations in Geophysics*, volume 10. Society of Exploration Geophysicists, Tulsa.

Zollo, A., Judenherc, S., Auger, E., D'Auria, L., Virieux, J., Capuano, P., de Franco, C. C. R., Makris, J., Nichelini, A., and Musacchio, G. (2003). Evidence for the buried rim of campi flegrei caldera from 3-d active seismic imaging. *Geophysical Research Letter*, **30**(19), 10/1–10/4.